



Aalborg Universitet

AALBORG UNIVERSITY  
DENMARK

## Mission Profile based System-Level Lifetime Prediction of Modular Multilevel Converters

Zhang, Yi

*Publication date:*  
2019

*Document Version*  
Publisher's PDF, also known as Version of record

[Link to publication from Aalborg University](#)

*Citation for published version (APA):*  
Zhang, Y. (2019). *Mission Profile based System-Level Lifetime Prediction of Modular Multilevel Converters*. Aalborg Universitetsforlag. Ph.d.-serien for Det Ingeniør- og Naturvidenskabelige Fakultet, Aalborg Universitet

### General rights

Copyright and moral rights for the publications made accessible in the public portal are retained by the authors and/or other copyright owners and it is a condition of accessing publications that users recognise and abide by the legal requirements associated with these rights.

- ? Users may download and print one copy of any publication from the public portal for the purpose of private study or research.
- ? You may not further distribute the material or use it for any profit-making activity or commercial gain
- ? You may freely distribute the URL identifying the publication in the public portal ?

### Take down policy

If you believe that this document breaches copyright please contact us at [vbn@aub.aau.dk](mailto:vbn@aub.aau.dk) providing details, and we will remove access to the work immediately and investigate your claim.



**MISSION PROFILE BASED SYSTEM-LEVEL  
LIFETIME PREDICTION OF MODULAR  
MULTILEVEL CONVERTERS**

**BY  
YI ZHANG**

DISSERTATION SUBMITTED 2019



**AALBORG UNIVERSITY**  
DENMARK





---

---

# **Mission Profile based System-Level Lifetime Prediction of Modular Multilevel Converters**

---

---

Ph.D. Dissertation  
Yi Zhang

Dissertation submitted November, 2019

Dissertation submitted: November, 2019

PhD supervisor: Prof. Frede Blaabjerg  
Aalborg University, Denmark

Assistant PhD supervisor: Prof. Huai Wang  
Aalborg University, Denmark

PhD committee: Associate Professor Amjad Anvari-Moghaddam (chair.)  
Aalborg University  
Professor Bhim Singh  
Indian Institute of Technology Delhi  
Professor Axel Mertens  
Leibniz Universität Hannover

PhD Series: Faculty of Engineering and Science, Aalborg University

Department: Department of Energy Technology

ISSN (online): 2446-1636  
ISBN (online): 978-87-7210-538-3

Published by:  
Aalborg University Press  
Langagervej 2  
DK – 9220 Aalborg Ø  
Phone: +45 99407140  
aauf@forlag.aau.dk  
forlag.aau.dk

© Copyright: Yi Zhang

Printed in Denmark by Rosendahls, 2020

# Abstract

With the increasing utilization of Modular Multilevel Converters (MMCs) in many applications, such as High-Voltage Direct Current (HVDC) transmissions, medium-voltage machine drives, electric ship, etc., the reliability performance of MMCs has attracted attention. In recent years, researchers have done much work to improve the reliability of MMCs. However, how to size the major devices/components of the MMC with compromised costs and design margins, while at the same time to fulfill a specific reliability target is still an open question. To cope with the challenge, a systematic reliability evaluation is a prerequisite. Accordingly, this Ph.D. project firstly studies the system-level power loss model for all major components in MMCs. Then, the electro-thermal modeling of the MMC is investigated. Based on these two models, a mission profile-based lifetime prediction method is proposed for the MMC system. The outcomes serve as a first step for developing realistic reliability analysis and model-based design methods for full-scale MMCs in practical applications.

For a quantitative reliability evaluation of an MMC, a systematic power loss model is studied at first. All major components, including IGBT modules, capacitors, inductors, and bleeding resistors, are covered in the model. The proposed analytical model is computationally efficient, relies on a limited amount of information (i.e., active and reactive power information), and considers the impact of transformer leakage inductance. Moreover, device parameters are measured experimentally. The parameter tolerances are also considered in the process.

Moreover, the electro-thermal modeling of the MMC is investigated. The thermal profiles of the MMC are classified into periodic and non-periodic profiles. Based on a frequency-domain analysis, different thermal modeling requirements are clarified in terms of the two different thermal profiles. Following, an equivalent thermal profile is firstly proposed to estimate the periodic thermal profiles of the MMC. The proposed method can model the inherent thermal unbalance of the MMC which does not require the aid of time-domain simulations. A quantitative error model is proposed to further simplify the equivalent thermal profile. A computational-efficient thermal

estimation can be achieved within a maximum allowable error. Furthermore, when it comes to the non-periodic thermal profiles, a system-level thermal model is proposed, which has two aspects: the junction/hotspot-to-local ambient thermal model, and local ambient-to-global ambient thermal model. The first aspect considers the Thermal Cross-Coupling (TCC) effects among the components. The second aspect models the TCC effects among different subsystems. The layout, cooling systems, cabinet materials are all comprehensively considered in the process. In addition, the thermal model of Thermal Interface Materials (TIMs) are also investigated comprehensively.

Finally, a mission profile-based lifetime prediction is performed from components to the MMC system. The justification of different mission profile resolution is investigated firstly. In addition, different lifetime model selections are also studied comparatively. Furthermore, a systematic methodology to perform reliability analysis from system-level modeling to component-level modeling, and then back to the system-level is demonstrated at last. It includes long-term mission profiles, lifetime modeling, Monte Carlo analysis, and redundancy analysis. The outcomes serve as a step for developing realistic reliability analysis and model-based design methods for full-scale MMCs in practical applications.

All the research developments have been verified by simulations and experiments. The contributions have been presented in 5 journal and several conference papers.

# Resumé

Med den stigende udnyttelse af modulære multi level omformere (Mmc'er) i mange applikationer, såsom højspændings jævnstrøm (HVDC) transmissioner, medium-spænding maskine drev, elektrisk skib, etc., pålidelighed ydeevne af MMCs har tiltrukket Opmærksomhed. I de seneste år har forskerne gjort meget arbejde for at forbedre pålideligheden af MMCs. Men hvordan man størrelse de store enheder/komponenter i MMC med kompromitterede omkostninger og design margener, mens på samme tid til at opfylde et specifikt pålideligheds målet er stadig et åbent spørgsmål. For at klare udfordringen er en systematisk vurdering af pålidelighed en forudsætning. Derfor, denne Ph.D. projekt for det første undersøgelser system-niveau strøm tab model for alle større komponenter i MMCs. Derefter undersøges den elektrotermiske modellering af MMC. Baseret på disse to modeller, en mission profil-baseret levetid forudsigelse metode er foreslået for hele MMC-systemet. Resultaterne tjener som et første skridt til at udvikle realistiske pålideligheds analyser og modelbaserede design metoder til fuld skala-Mmc'er i praktiske anvendelser.

For en kvantitativ pålidelighed evaluering af en MMC, en systematisk strøm tab model er undersøgt i første. Alle større komponenter, herunder IGBT-moduler, kondensatorer, Induktionsspoler og blødnings modstande, er dækket af modellen. Den foreslåede analytiske model er beregningsmæssigt effektiv, afhængig af en lille mængde information (dvs. aktiv og reaktiv effekt information), og betragter virkningen af transformator lækage induktion. Desuden måles enhedens parametre eksperimentelt. De ujævne parametre tages også i betragtning i processen.

Desuden er den elektro-termiske modellering af MMC undersøgt. De termiske profiler af MMC er klassificeret i periodiske og ikke-periodiske profiler. Baseret på en frekvens-domæne analyse, er forskellige termiske modellering krav præciseret for de to forskellige termiske profiler. Efterfølgende foreslås en tilsvarende termisk profil for at estimere de periodiske termiske profiler af MMC. Den foreslåede metode kan modellere den iboende termiske ubalance i MMC, som ikke kræver hjælp af tids-domæne simuleringer. Desuden foreslås en kvantitativ fejl model for yderligere at forenkle den tilsvarende

termiske profil. En beregnings effektiv termisk vurdering kan opnås inden for en maksimal tilladt fejl. Når det kommer til den ikke-periodiske termiske profiler, en system-niveau termisk model er foreslået, som har to aspekter: Junction/hotspot-til-lokale omgivende termisk model, og lokale omgivende-til-globale omgivende termisk model. Det første aspekt betragter de termiske Cross-kobling (TCC) effekter blandt komponenterne. Det andet aspekt modellerer TCC-effekterne blandt forskellige delsystemer. Layoutet, kølesystemer, kabinet materialer er alle grundigt overvejet i processen. Desuden er den termiske model af termisk interface materialer (TIMs) også undersøgt.

Endelig udføres en mission Profile-baseret livstids forudsigtelse fra komponenter til MMC-systemet. Begrundelsen for forskellige missions profil modeller undersøges først, hvilket tjener til at kvantificere dens indvirkning på livstids forudsigtelse. Desuden er forskellige livstids modelvalg også undersøgt forholdsvis. Endvidere, en systematisk metode til at udføre pålideligheds analyse fra system-niveau modellering til komponent-niveau Modeling, og derefter tilbage til systemet-niveau er demonstreret omsider. Det omfatter langsigtede missions profiler, Lifetime modellering, Monte Carlo analyse og redundans analyse. Resultaterne tjener som et skridt til at udvikle realistiske pålideligheds analyser og modelbaserede design metoder til fuld skala-Mmc'er i praktiske anvendelser.

Alle forsknings udviklinger er blevet verificeret af simuleringer og eksperimenter. Bidragene er blevet præsenteret i 5 tidsskrifter og flere conferenceoplæg.

# Preface

This Ph.D. thesis is a summary of the Ph.D. project "Mission Profile Based System-Level Lifetime Prediction of Modular Multilevel Converters".

First of all, I would like to express my gratefulness to my supervisors, Professor Frede Blaabjerg and Professor Huai Wang. They have provided me professional and patient guidance during the last three years. Their support and encouragement are a great help for me to complete my Ph.D. study. It has been a great experience to work under their supervision.

I am also grateful to Associate Professor Maryam Saeedifard for helping me in the visiting of Georgia Tech, USA. I benefit a lot from her valuable guidance and kindness during the period.

I would also like to thank Associate Professor Yongheng Yang for his valuable suggestions and helps. Special thanks go to Mr. Zhongxu Wang for his help in many discussions and experiments.

Many thanks to Dr. Haoran Wang, Dr. Yanfeng Shen, Dr. Ionuț Vernica, Dr. Qian Wang for their help in research and daily life. I would also like to thank Dr. Rui Li, Dr. Yaoqiang Duan, Mr. Hao Niu, Dr. Guanguan Zhang, Mr. Zhijian Yin, Mr. Zhan Shen, Mr. Hong Gong, Ms. Zhongting Tang, etc. Moreover, many thanks to all the colleagues at the Department of Energy Technology, Aalborg University for their kind help.

Last but not least, I would like to express my gratitude to my family for their support and encouragement.

Yi Zhang  
Aalborg University, November 8, 2019





# Contents

<b>Abstract</b>	<b>iii</b>
<b>Resumé</b>	<b>v</b>
<b>Preface</b>	<b>vii</b>
<b>Report</b>	<b>1</b>
<b>1 Introduction</b>	<b>3</b>
1.1 Background . . . . .	3
1.2 Power Losses of Critical Components in MMCs . . . . .	6
1.3 Electro-Thermal Modeling of the MMC . . . . .	7
1.3.1 Electro-thermal Modeling of the Periodic Profiles . . . . .	8
1.3.2 Electro-thermal Modeling of the Non-periodic Profiles . . . . .	9
1.3.3 Thermal Interface Materials of IGBT Modules . . . . .	10
1.4 Lifetime Prediction for Components and Systems . . . . .	12
1.4.1 Impacts of Mission Profiles and Lifetime Models on Component-level Reliability . . . . .	12
1.4.2 System-level Reliability Prediction . . . . .	13
1.5 Research Questions and Objectives . . . . .	14
1.6 Thesis Outline . . . . .	15
1.7 List of Publications . . . . .	15
<b>2 System Configuration and Power Loss Evaluation for MMCs</b>	<b>19</b>
2.1 Abstract . . . . .	19
2.2 Analytical Modeling of an MMC . . . . .	19
2.3 Description of a Down-scale MMC Prototype . . . . .	23
2.4 Modeling of the Power Losses of the Critical Components . . . . .	24
2.4.1 Power Losses of the IGBT Modules . . . . .	25
2.4.2 Power Losses of Capacitors . . . . .	28
2.4.3 Power Losses of the Arm Inductors . . . . .	30

2.4.4	Power Losses of the Bleeding Resistors . . . . .	30
2.5	Experimental Verifications . . . . .	32
2.6	Summary . . . . .	33
<b>3</b>	<b>Comprehensive Electro-thermal Model of the MMC</b>	<b>35</b>
3.1	Abstract . . . . .	35
3.2	Classification of Typical Thermal Profiles . . . . .	35
3.2.1	Time-domain Thermal Profile Analysis . . . . .	36
3.2.2	Frequency-domain Thermal Profile Analysis . . . . .	40
3.3	Periodic Power Loss Profiles of MMCs . . . . .	40
3.3.1	Equivalent Power Loss Profile . . . . .	41
3.3.2	Parameter Sensitivity Analysis . . . . .	43
3.3.3	Simplification with Quantitative Errors . . . . .	46
3.3.4	Experimental Validation . . . . .	48
3.4	Non-periodic Power Loss Profiles of MMCs . . . . .	51
3.4.1	Junction/Hotspot-to-Local Ambient Thermal Modeling	53
3.4.2	Local Ambient-to-Global Ambient Thermal Modeling .	54
3.5	Thermal Interface Materials in SMS . . . . .	57
3.5.1	Impact of TIM Thicknesses on Predicted Lifetime . . . .	57
3.5.2	An Empirical Characterization Model for TIMs under Realistic Conditions . . . . .	60
3.6	Summary . . . . .	63
<b>4</b>	<b>Mission Profile-based Lifetime Prediction for MMCs</b>	<b>65</b>
4.1	Abstract . . . . .	65
4.2	The Impact of Mission Profiles . . . . .	65
4.2.1	Different Mission Profile Resolutions based on a Wind Power Application . . . . .	66
4.2.2	Impact of Mission Profile Resolutions on Predicted Life- time . . . . .	68
4.3	Impact of Lifetime Model Selection . . . . .	69
4.3.1	Typical Lifetime Models . . . . .	69
4.3.2	Impact of Lifetime Model Selections on Predicted Lifetime	70
4.4	System-level Reliability Assessment . . . . .	73
4.4.1	Thermal Profiles and Static Annual Damage of Compo- nents . . . . .	73
4.4.2	Monte Carlo Simulations and System-Level Failure Prob- ability Calculation . . . . .	77
4.4.3	Discussion . . . . .	80
4.5	Summary . . . . .	81

<b>5</b>	<b>Conclusions</b>	<b>83</b>
5.1	Summary . . . . .	83
5.2	Main Contributions . . . . .	84
5.3	Research Perspectives . . . . .	85
	<b>Bibliography</b>	<b>87</b>
	References . . . . .	87



# Report



# Chapter 1

## Introduction

### 1.1 Background

Modular Multilevel Converters (MMCs) were proposed in 2003 [1] and first used commercially in the Trans Bay Cable project in San Francisco [2]. This topology has been becoming one of the most common types of Voltage-Source-Converter High Voltage Direct Current (VSC-HVDC) transmission systems. Compared to the conventional two- and three-level VSCs, the MMC offers many advantages, such as modularity, scalability, negligible ripple content in outputs, largely reduced switching frequency, improved efficiency, etc [2–5]. Due to these merits, the power ratings of MMCs have been up to 2 GW and with voltage ratings of up to 400 kV as listed in Table 1.1, and even higher ratings are technically feasible. Additionally, many medium-voltage applications also adopt the topology, such as machine drives [6, 7], DC electric ship [8], etc.

The MMC has merits of modularity and redundancy, which enhance its reliability and fault-tolerant capability. However, the applications of MMCs still face severe reliability challenges. First, the MMC is a large-scale and complex system. As shown in Fig. 1.1, hundreds or thousands of individual components, including Insulated-Gate Bipolar Transistors (IGBTs), capacitors, and inductors, must operate properly. For instance, the first commercial MMC-HVDC project—Trans Bay Cable project adopts more than 2,000 IGBT modules and over 1,000 capacitor banks [10]. However, both IGBTs and capacitors are reliability-critical components, which contribute to over 50% failures in power electronic systems [11, 12]. Any unexpected failures in the single device might lead to the shut-down of the whole system and lower the availability. Besides, the application/environmental conditions of the MMC are much more severe than the conventional power electronic applications. For example, in the case of an offshore wind energy collection system based

**Table 1.1:** Selected MMC-based Projects around the World [9]

Project	Capacity (MW)	DC-link Voltage (kV)	Supplier
Offshore wind-power plant (OWPP) connection project			
Borwin Beta	800	$\pm 300$	SIEMENS
Borwin Gamma	900	$\pm 320$	SIEMENS
Dolwin Alpha	800	$\pm 320$	ABB
Dolwin Alpha	916	$\pm 320$	ABB
Dolwin Gamma	900	$\pm 320$	GE
Helwin Alpha	576	$\pm 250$	SIEMENS
Helwin Beta	690	$\pm 320$	SIEMENS
Sylwin Alpha	864	$\pm 320$	SIEMENS
Power grid Interconnection			
Trans Bay Cable	400	$\pm 200$	SIEMENS
INELFE	2000	$\pm 320$	SIEMENS
NordBalt	700	$\pm 300$	ABB
Skaggerrak 4	700	500	ABB
SydVastlanken	$2 \times 600$	$\pm 300$	GE
COBRAcable	700	$\pm 320$	SIEMENS
Nemo Link	1000	$\pm 400$	SIEMENS

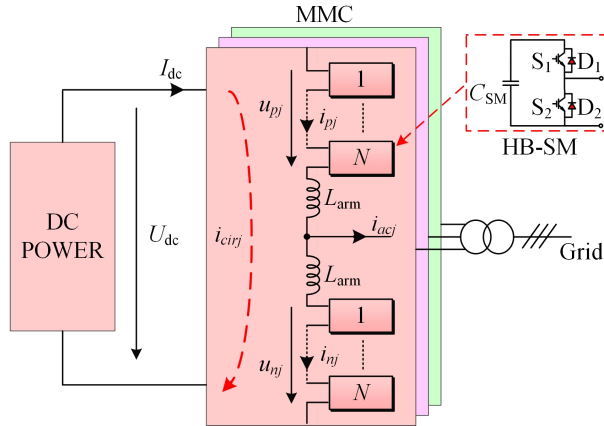


**Fig. 1.1:** Circuit Configuration of a typical modular multilevel converter [J1].

on the MMC [13, 14], temperature variations, humidity, and salinity accelerate the degradation of the devices and the entire system. Any failures in the offshore MMC platform usually lead to enormous economic costs, and further maintenance is also time-consuming and costly. From this perspective, reliability is of great importance to the design and operation of the MMC.

In the previous studies, many solutions have been proposed to improve the reliable performance of the MMC, such as redundancy [15], fault-tolerant control [16], and sizing components with excessive design margins (e.g., size components with larger Safe Operating Areas (SOA), selecting more massive



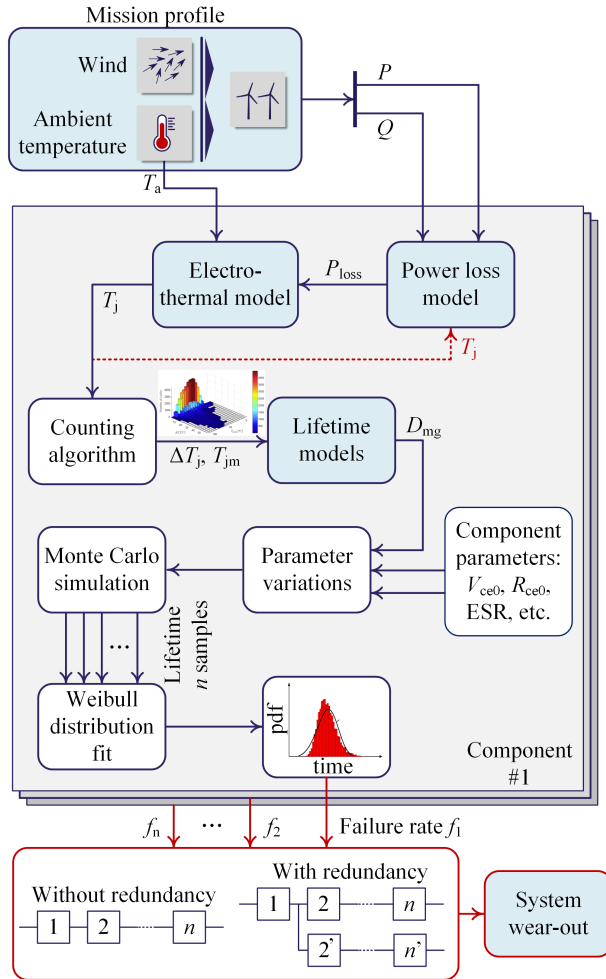


**Fig. 1.2:** Flowchart of the mission profile based lifetime prediction method for an MMC in a wind power generation application (This Ph.D. project discusses mainly the mission profile, power loss model, thermal model, and system wear-out reliability as indicated with blue color in the figure).

heatsinks, etc.). However, the design constraints in cost and efficiency impose significant challenges on the excessive utilization of redundancies and design margins. As a result, the industry increasingly demands a methodology to design an MMC with compromised costs and design margins, while fulfilling a specific reliability target [J1]. To achieve the target, a systematic understanding of the failure mechanisms of the MMC is a prerequisite, which involves the understanding of operational environments, loading conditions, key design variables, component sizing, system layout, etc.

Lifetime prediction is one of the important tools to evaluate the reliability performance of MMCs, which in return has attracted wide attention [17–19]. However, most of these reliability evaluations are based on the component-level reliability information provided in the Military-Handbook-217F [20]. The reliability data in the handbook is collected from the large-population of failed products based on the component level. Although the accelerated factors under different stresses (e.g., temperatures, voltages, etc.) are considered in [19], the failure rate data still do not differentiate the loading conditions, technologies, and manufacturers. Moreover, the wear-out of devices is not considered. From the design perspective, the wear-out failures of components need to be avoided or limited to a certain level. Otherwise, exponential failure issues might occur during the warranty period due to component degradation. Thus, a constant failure rate method is limited to provide evidence to uncover the root cause of failures or to provide design insights for reliability improvement.

Mission profile based lifetime prediction is an application-dependent approach to predict the reliability of power electronic components and/or systems [21], as shown in Fig. 1.2. In this method, mission profiles (i.e., the operating conditions and environments) of a system are converted into loss profiles, thermal profiles, and finally being able to obtain the quantified reliability metrics [J1]. The corresponding estimated reliability performance is closely correlated with its loading conditions and applied environments, making it possible to locate the failure roots more accurately and to achieve a specific reliability specification in the design stage. Although the method has been presented to consider the component-level reliability of MMCs in [22] and [23]. However, considering the numerous components, Sub-Modules (SMs), and complicated redundancies, it is still challenging to apply the same method to do the system-level reliability of a complete MMC system.

## 1.2 Power Losses of Critical Components in MMCs

Power loss models are one of the essential parts of the mission profile-based lifetime prediction. As shown in Fig. 1.2, power losses significantly determine the component junction temperatures or hotspot temperatures. These temperatures are regarded as critical stresses to component reliability in power electronics [11]. As a result, the accuracy of the power loss estimation is significantly correlated to the predicted lifetime. For the MMC with many SMs, the power loss model is challenging to consider a large number of components, the complicated structure, various modulation and control strategies, etc. Thus, a widely accepted method for power loss evaluation of the MMC is numerical simulation [24]. Some simplified simulation methods are also proposed to improve the computational efficiency with a com-

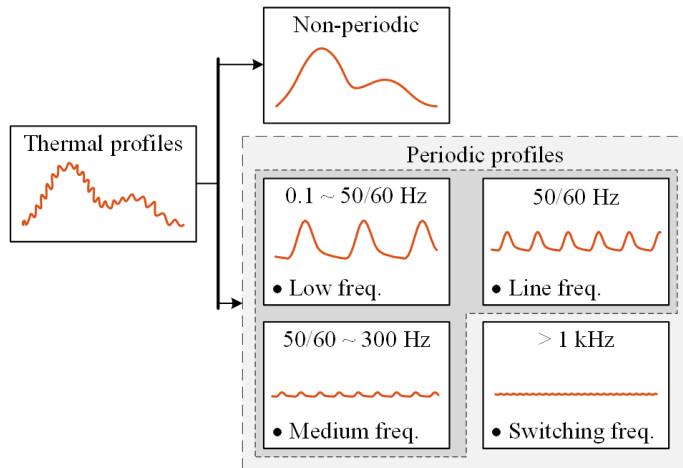


Fig. 1.3: Typical thermal profiles with multiple frequencies in power electronic converters [C5].

promised accuracy [25]. Simulation-based solutions have the merits of considering sophisticated degrees of freedom in terms of control strategies and modulation algorithms in the MMC. However, the reliability evaluation usually requires to compare the performance of different design schemes, such as various device selection, different number of SMs, switching frequencies, etc. Different cases require to modify the corresponding simulation parameters, which results in that the simulation-based solution is not preferable for reliability evaluation.

Analytical power loss models have advantages of being computationally efficient and easy to change parameters [26–32]. Based on a specific modulation scheme, reference [26] establishes the power loss model for the power semiconductor devices. Afterwards, many analytical models consider more variables, such as inserted probabilities of SMs [27], different circuit topologies [28], variable switching frequencies based the Nearest-Level Modulation (NLM) [29], junction temperatures [30], grid integration [31], the use of SiC devices [32], etc. However, all the above-mentioned studies focus on the power semiconductor devices only. The power losses of capacitors, inductors, and bleeding resistors (in parallel of capacitors) are rarely discussed, and this is important for complete system analysis.

### 1.3 Electro-Thermal Modeling of the MMC

Temperatures are one of the most significant stressors for many power electronic devices [11, 12]. Electro-thermal analysis, thus, is critical to perform reliability analysis. As shown in Fig. 1.3, thermal profiles for power

semiconductor devices have two classifications:

- Periodic profiles: temperature fluctuations are induced by periodic power loss profiles (i.e., power losses related to fundamental-frequency currents), which cover four different frequency ranges: 1) low frequencies are from 0.1 Hz to 50/60 Hz, typically as low-speed variable frequency drives [33]; 2) line frequencies (e.g., utilities); 3) medium frequencies range from 50/60 Hz to around 300 Hz, typically as high-speed machine drives and 4) switching frequencies are mostly larger than 1 kHz [J2].
- Non-periodic profiles: thermal swings are caused by long-term environmental variations, e.g., ambient temperatures, wind speed profiles [34], solar irradiation [35], working loads [36], etc. The time scale is typically varied from seconds to minutes [J2];

In the-state-of-the-art, thermal estimation of IGBT modules in MMCs has been reported in [22, 37–40]. However, the systematic thermal behaviors of the MMC from the above two classifications still have not attracted sufficient discussions and need more analysis.

### 1.3.1 Electro-thermal Modeling of the Periodic Profiles

The periodic thermal profiles are mainly related to fundamental-frequency currents. Although the thermal amplitudes at the periodic profiles are usually small compared to the non-periodic profiles, the number of the periodic thermal cycles are extremely large [41]. According to [34] and [41], the enormous thermal cycles with minor amplitudes accumulate non-neglected fatigues in the devices. Meanwhile, reference [42] also experimentally verifies that a large amount of small thermal cycles accelerate the device aging. However, the impacts of periodic thermal stresses are commonly neglected in previous reliability evaluations of the MMC [22]. Also, a proper estimation of the periodic thermal fluctuations is of importance for the cooling system designs. Especially for the variable-frequency applications [43], the peak junction temperature in these applications might exceed up to 3 or more times than the temperatures under 50/60-Hz conditions. It further highlights the importance of electro-thermal modeling from the perspective of the periodic profiles.

One of the challenges to estimate periodic thermal profiles of the MMC is the inherent thermal unbalance existing within an SM of the MMC. Due to the device currents of the MMC contain an inherent DC-bias component [44], the IGBTs and the diodes are conducting over or fewer of 50% in a fundamental-current cycle. For instance, reference [22] reveals that the downside IGBT chip is always hotter than the upside IGBT in a half-bridge SM. Moreover,

the inherently unbalanced thermal behaviors are not constant, which are varied with the operational conditions. These characteristics lead to a more complicated electro-thermal modeling for the periodic profiles.

Secondly, the computational burden of thermal estimation is also a challenge in electro-thermal modeling of the periodic profiles. The lifetime prediction process of the MMC is usually based on long-term mission profiles, in which a large amount of periodic power loss profiles are necessary to be converted into thermal profiles. The multi-physics simulation tools, such as the Finite Element Method (FEM) and electro-thermal simulations (e.g., PLECS), provide comprehensive thermal results. However, these advanced methods require complicated geometrical structures, material information, and control/modulation strategies. Massive computations are thus involved. Apart from the simulation methods, analytical modeling methods are more promising from the perspective of long-term reliability evaluation. A straightforward analytical method is to apply the convolution calculation of thermal models and instantaneous power loss profiles [45]. Nonetheless, neither the convolution algorithm nor the instantaneous power losses are easy to be computed. Following, some computationally efficient thermal estimation methods are also developed for two-level converters, such as the square wave profile [46], the fixed half-sine profile [47], and the two-level profile [34]. However, all the above methods are discussed based on the conventional two-level converters. The feasibility of these methods for MMCs has not been fully revealed yet.

On the other hand, when the prior-art simplified thermal models are proposed to improve the computational efficiency, another challenge that comes with is the error level. For example, the square-wave profile [46] has advantages of simplicity to a large extent but degrades its accuracy. In order to improve the accuracy of the estimated temperature, the fixed half-sine profile is recommended by [47]. The fixed half-sine loss profile is divided into a series of power dissipation pulses at first. More accurate power loss profiles can be developed, which in return provides a good approximation of the junction temperature. However, this method costs more computational burden. Under certain conditions, a two-level profile is a good trade-off approximation of the half-sine profile [34]. However, all methods above have not quantified the error level under different conditions or different device selections. Therefore, a more generic simplification method is necessary for the electro-thermal modeling of the periodic profiles.

### **1.3.2 Electro-thermal Modeling of the Non-periodic Profiles**

Unlike the periodic profile with the time scale of around micro-seconds, non-periodic profiles typically have larger time scales (i.e., several seconds to minutes). Moreover, the corresponding thermal amplitudes of the non-

periodic profiles are remarkably larger than that of the periodic profiles. As a result, thermal estimations regarding non-periodic profiles are of importance for the cooling system design/management and reliability analysis of the MMC. Due to the difference in thermal behaviors under different time scales, the non-periodic profiles suffer from distinct challenges as follows.

Firstly, as the time scale increases, Thermal Cross-Coupling (TCC) effects significantly affect the thermal behaviors of devices. References [22, 37–40] have studied the thermal behaviors of IGBT modules in MMC systems, but they typically use One-Dimensional (1-D) RC lumped thermal networks (e.g., Foster and Cauer networks [46, 48]). Manufacturers normally provide the 1-D thermal networks in the datasheet. However, the 1-D networks neglect the TCC effects among devices. TCC effects occur when multiple chips/devices exist with the same package and even if different power modules are mounted on the same heatsink. Moreover, considering the increasing demands in higher power density and smaller parasitics, more compact packaging with multi-chips is used commonly in power electronic systems. This means that the TCC effects between devices are more significant. The TCC effects have attracted increasing discussions in many power electronic applications, such as motor drives, PV inverters [35, 49], etc. The MMC application has rarely been discussed regarding the TCC effects among devices.

Secondly, the thermal behaviors of devices are not only affected by the power dissipations, but also the environmental temperatures. In the conventional power electronic applications (volume  $\leq 1 \text{ m}^3$ ), such as motor drives, PV inverters [35, 49], etc., all the devices assume to have the same environmental thermal stresses. The further simplifications ignore the impacts of cabinets and cooling systems [22], assuming the environmental thermal stresses of devices straightforwardly equal to the ambient temperature outside of the cabinet. These assumptions might be reasonable for certain types of systems. However, the complexity-level and the overall size of the MMC are far more beyond the scope of those converters that have been studied. Different SMs exposing under homogeneous environmental stress are questionable. These challenges require a further study of the electro-thermal modeling of the non-periodic profiles in MMCs.

### 1.3.3 Thermal Interface Materials of IGBT Modules

With increasing requirements of power density and extended lifetime expectation in many power electronics applications, the power semiconductor manufacturers consistently endeavor to increase the current-carrying capability of power devices with smaller packaging. Power semiconductor devices are expected to resist more power dissipations, higher temperature limitations, etc. Simultaneously, system integration designers pursue to reduce the volume of power converters. The commonly applied solutions include reduc-

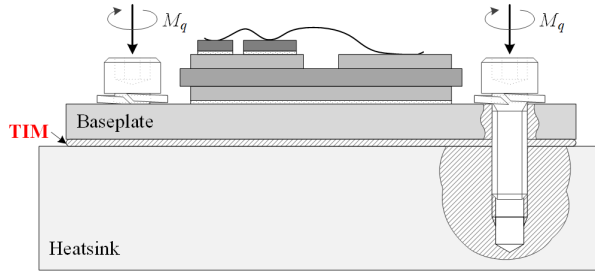


**Fig. 1.4:** Schematic represent on a real joint surface of the Thermal Interface Materials (TIMs) [J5].

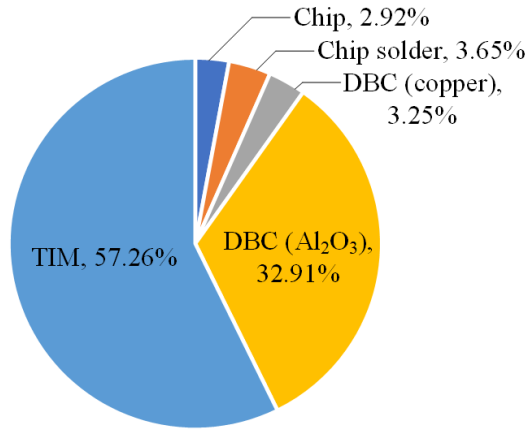


**Fig. 1.5:** An overview of thermal resistance share in a specific IGBT module, data from [46] (TIM: thermal interface material, DBC: direct bonded copper, which consists of a ceramic layer and two copper layers) [C3].

ing the margin of cooling systems and using a more compact heatsink. This conflict trend results in increasingly higher demands on the Thermal Interface Materials (TIMs), which is usually applied between the power semiconductor devices and heatsinks.

As shown in Fig. 1.4, a typical power electronic system contains a power module, TIMs, and a cooling system. According to [46], the thermal-resistance contribution of the TIM can be up to 50% from the junction to the heatsink. An inappropriate TIM design usually accelerates the degradation of the power semiconductor device itself. However, the thermal model of the TIM has not attracted much attention in power electronics. Reference [22] has discussed the thermal model of IGBT modules in an MMC system. The thermal resistance of the TIM has been not clarified. Beyond the MMC applications, other study cases often commonly assume the thermal resistance of TIM as a

constant value by a recommendation in the datasheet [34, 36, 50]. Since TIM has a significant contribution to the overall thermal resistance, the prior-art simplified thermal modeling of the TIM might lead to misleading the thermal stresses. The corresponding lifetime prediction results in return are lack of confidence. Therefore, from the perspective of reliability, the impact of TIM still needs further investigation.

Apart from the impact of TIMs on the lifetime of power devices, the thermal-model characterization of the TIM has also attracted increasing attention. The standard ASTM D5470 [51] provides dedicated guidelines for thermal resistance characterization of the TIM. However, the testing conditions of the standard is developed from microelectronic applications, where idealized flat and minimum-roughness measuring surface ( $< 0.4 \mu\text{m}$ ) are required. When it comes to power electronic applications, the baseplates of power module packaging are usually pre-bended, in order to handle a larger thermal expansion under high power dissipations. Moreover, the commonly applied milled heatsinks (roughness is around  $10\text{-}15 \mu\text{m}$ ) are also different from microelectronic applications. These differences raise a question if the standard established from microelectronics can be extended to power electronics simply. Based on the measurements of device junction temperatures in power electronic applications, reference [52] has uncovered that the correlation between the actual thermal resistance and TIM datasheet value measured by the standard is limited. In order to further understand the difference from the physical mechanism, several physical models are proposed in [53, 54] to model the different surface conditions for TIMs. However, physical models are difficult to be applied in engineering design, since these models are complicated and require many inputs of mechanical, thermal, material parameters, etc. Therefore, how to develop a simple characterization model for TIMs while considering the realistic conditions of power electronic applications is significant.

## **1.4 Lifetime Prediction for Components and Systems**

### **1.4.1 Impacts of Mission Profiles and Lifetime Models on Component-level Reliability**

As shown in Fig. 1.2, the lifetime prediction of a component relies on mission profiles and lifetime model selections. Thus, the justification of a specific mission profile or lifetime model should be discussed at first.

The mission profile is the starting point for the lifetime prediction. The consideration of the mission profile is not only an essential part of the product development process but also forms the basis for the specification of prod-



uct requirements. However, many industrial fields are still lack of a widely accepted requirement for mission profiles. In reference [22], IGBT modules of the MMC system are analyzed by the mission profile based lifetime prediction method, but the justification of mission profiles with a resolution of 1 hour/data is not fully discussed. Beyond the MMC applications, the impact of the mission profile on the predicted lifetime has not been received much attention as well, such as Wind Turbine Systems (WTS) [34], Photo-Voltaic (PV) inverters [35]. In light of the above, a comprehensive investigation of the mission profile is significant.

In the second aspect, the selection of lifetime models also affects the predicted results. For power semiconductor devices, lifetime models are typically expressed as a specific number of temperature cycles. The lifetime of power semiconductor devices involves multi-physical domains. To some extent, the predicted lifetime is usually affected by different lifetime model selections. In the existing lifetime models of the power semiconductor devices, Coffin Manson model is widely accepted [55], which considers the amplitudes of temperature swings only. Based on the Coffin Manson model, more comprehensive parameters are involved, such as elastic strains of devices materials  $\Delta T_0$  [56], average or mean temperatures  $T_m$  [46], minimum or maximum temperatures  $T_{\min}$  or  $T_{\max}$  [57], power-on time  $t_{\text{on}}$  [58], etc. Considering the limitations and effective boundary for different lifetime models, it is inevitable to raise a question on which lifetime model should be used in a specific application. In the lifetime prediction of the MMC system, the adoption of the specific lifetime model is rarely discussed either. Therefore, the impact of lifetime model selection still remains unclear.

#### 1.4.2 System-level Reliability Prediction

The system-level reliability prediction is significant to achieve a specific reliability target while limiting the cost. Simultaneously, this methodology is valuable for economic analysis. The previous studies [17–19] have many discussions on the system-level reliability of the MMC. However, many of these methods are based on constant-failure-rate models provided in the Military-Handbook-217F [20]. The constant failure rates consider the large-population statistics of random failures. For the MMC with a small amount of commissioned projects, the statistical random failures are obviously limited. Moreover, the wear-out failures are not considered. Physics-of-Failure (PoF) methods consider the failure mechanism of components, which has been applied to the component-level reliability of MMCs in [22] and [23]. Since the MMC has numerous components, SMs, and complicated redundant schemes, the PoF method is still challenging to achieve the system-level reliability prediction of the MMC.

Some studies have investigated the system-level reliability via PoF meth-

ods for other kinds of converters, such as a DC/DC converter [36] and a PV micro-inverter [35]. When it comes to the MMC, both the electric ratings and footprint are far beyond the scope of the conventional power electronic systems. Moreover, the redundancies of the MMC are also out of the scope of previous studies. As a result, it is limited to directly extend those previous studies to the MMC application.

## 1.5 Research Questions and Objectives

With the above motivations, the main research question is "how to establish a mission profile based system-level reliability prediction methodology for MMCs?" It includes the multi-disciplinary understanding of the MMC, e.g., electric, thermal, materials, layouts, etc., which cover the following research sub-questions:

- How to evaluate the power losses of all major components of the MMC for reliability evaluation?
- How to estimate the thermal behaviors across multi-time scales in reliability prediction?
- How to predict the lifetime of the MMC with numerous SMs and complicated redundancies?

Motivated by the above issues, this Ph.D. project investigates a methodology to evaluate the system-level reliability of the MMC. The objectives can be summarized as follows:

- **To establish a system-level power loss model for the MMC:** it requires to consider all major components, including power semiconductor devices, capacitors, inductors, and bleeding resistors. In order to achieve a long-term reliability prediction, the established power loss model also requires being computationally efficient, friendly to change parameters, and considering the leakage inductance of the transmission transformer.
- **To establish comprehensive electro-thermal modelings to consider a multi-time scale thermal behaviors in the MMC system:** based on different frequency responses of thermal profiles, the comprehensive electro-thermal modelings are required to be computationally efficient, having a quantitative error, considering the TCC effects among different components, subsystems, etc. Moreover, the impact of TIM is necessary to be discussed in the modeling.

**Table 1.2:** The related publications for each chapter.

Chapter No.	Contents	Relevant Publications
2	Power loss model	C6, J1
	Thermal model of periodic profiles	C4, J1, J2, J3
3	Thermal model of non-periodic profiles	C5, J4
	Thermal interface materials	C3, J5
4	Mission profiles and lifetime models	C1, C2
	System-level reliability assessment	J4

- **To conduct system-level lifetime prediction of the MMC:** as mentioned above, the lifetime prediction of the MMC involves cross-disciplinary knowledge. The justification of a specific mission profile modeling and a lifetime model is necessary to be investigated at first. Moreover, considering the numerous components, SMs, and redundancies, the Ph.D. project is also aimed to conduct a mission profile-based lifetime prediction method from components to the whole system.

## 1.6 Thesis Outline

The outcome of this project is documented by a Ph.D. thesis, which includes two parts: a report and related publications.

Chapter 1 introduces the backgrounds and challenges of the study. A system-level power loss model of the MMC is depicted in Chapter 2. Electro-thermal modeling of the MMC is introduced in Chapter 3, including periodic profiles, non-periodic profiles, and TIMs. The comparative investigations of mission profiles and lifetime models are discussed in Chapter 4. A methodology of system-level lifetime prediction is also discussed at the same time. The summary and outlook are remarked at last. All discussions are carried out with simulations on a full-scale 30-MW MMC system. Additionally, experimental tests on a 15-kVA MMC prototype are also provided.

To depict the contributions for each chapter, the relationship between the chapters of the Ph.D. thesis and the publications are shown in Table. 1.2.

## 1.7 List of Publications

The research outcomes through the Ph.D. study are listed below, including journal papers and conference publications.

### *Journal Papers*

- J1. **Y. Zhang**, H. Wang, Z. Wang, Y. Yang, and F. Blaabjerg, "Simplified thermal modeling for IGBT modules with periodic power loss profiles in modular mul-

tilevel converters," *IEEE Trans. Ind. Electron.*, vol. 66, no. 3, pp. 2323–2332, 2019.

- J2. **Y. Zhang**, H. Wang, Z. Wang, Y. Yang, and F. Blaabjerg, "A Simplification Method for Power Device Thermal Modeling with Quantitative Error Analysis," *IEEE J. Emerg. Sel. Top. Power Electron.*, vol. 7, no. 3, pp. 1649–1658, 2019.
- J3. **Y. Zhang**, H. Wang, Z. Wang, and F. Blaabjerg, "Computational-Efficient Thermal Estimation for IGBT Modules under Periodic Power Loss Profiles in Modular Multilevel Converters," *IEEE Trans. Ind. Appl.*, vol. 55, no. 5, pp. 4984–4992, 2019.
- J4. **Y. Zhang**, H. Wang, Z. Wang, F. Blaabjerg, and M. Saeedifard, "Mission Profile based System-level Lifetime Prediction for Modular Multilevel Converters," *IEEE Trans. Power Electron.*, Under Review, 2019.
- J5. **Y. Zhang**, H. Wang, Z. Wang, and F. Blaabjerg, "An empirical model for thermal interface materials based on experimental characterizations under realistic conditions," *Microelectron. Reliab.*, vol. 88–90, no. May, pp. 806–811, 2018.
  - Z. Wang, H. Wang, **Y. Zhang**, and F. Blaabjerg, "A Viable Mission Profile Emulator for Power Modules in Modular Multilevel Converters," *IEEE Trans. Power Electron.*, Early access, 2019.
  - H. Wang, H. Wang, Z. Wang, **Y. Zhang**, X. Pei, and Y. Kang, "Condition Monitoring for Submodule Capacitors in Modular Multilevel Converters," *IEEE Trans. Power Electron.*, Early Access, 2019.

#### Conference Papers

- C1. **Y. Zhang**, H. Wang, Z. Wang, Y. Yang and F. Blaabjerg, "The impact of mission profile models on the predicted lifetime of IGBT modules in the modular multilevel converter," in *Proc. 43rd Annual Conference of the IEEE Industrial Electronics Society (IECON)*, Beijing, 2017, pp. 7980–7985.
- C2. **Y. Zhang**, H. Wang, Z. Wang, Y. Yang and F. Blaabjerg, "Impact of lifetime model selections on the reliability prediction of IGBT modules in modular multilevel converters," in *Proc. IEEE Energy Conversion Congress and Exposition (ECCE)*, Cincinnati, OH, 2017, pp. 4202–4207.
- C3. **Y. Zhang**, H. Wang, Z. Wang, Y. Yang and F. Blaabjerg, "Impact of the Thermal-Interface-Material Thickness on IGBT Module Reliability in the Modular Multilevel Converter," in *Proc. International Power Electronics Conference (IPEC-Niigata ECCE Asia)*, Niigata, 2018, pp. 2743–2749.
- C4. **Y. Zhang**, H. Wang, Z. Wang and F. Blaabjerg, "Simplified Estimation of the Junction Temperature Fluctuation at the Output Frequency for IGBT Modules in Modular Multilevel Converters," in *Proc. IEEE Energy Conversion Congress and Exposition (ECCE)*, Portland, OR, 2018, pp. 1–5.
- C5. **Y. Zhang**, H. Wang, Z. Wang and F. Blaabjerg, "Simplified Multi-time Scale Thermal Model Considering Thermal Coupling in IGBT Modules," in *Proc. IEEE Applied Power Electronics Conference and Exposition (APEC)*, Anaheim, CA, USA, 2019, pp. 319–324.

- C6. **Y. Zhang**, H. Wang, Z. Wang, F. Blaabjerg and M. Saeedifard, "System-level Power Loss Evaluation of Modular Multilevel Converters," in *Proc. IEEE Energy Conversion Congress and Exposition (ECCE)*, Baltimore, USA, 2019.



## Chapter 2

# System Configuration and Power Loss Evaluation for MMCs

### 2.1 Abstract

A system-level power loss evaluation is a prerequisite for the reliability assessment of the MMC system. The prior-art studies have many discussions on the power losses of the MMC, such as numerical simulations [24, 25], analytical power loss models [26–32]. However, most of them focus on the power semiconductor devices only. Capacitors, inductors, and bleeding resistors (in parallel of capacitors), which contribute to non-negligible power losses, do not have been paid much attention. In this chapter, the analytical modeling of an MMC is introduced. Moreover, from the perspective of system-level reliability analysis, a power loss model is established. This model involves the critical components in the MMC, which is computationally efficient and requires system-level specifications only. A 15 kVA experimental prototype validates the effectiveness of the proposed model.

### 2.2 Analytical Modeling of an MMC

Fig. 2.1 shows an MMC interfacing to the grid through a transformer.  $L_T$  is the leakage inductance of the transformer, and  $L_0$  is the arm inductor. The leakage inductance of a transmission transformer is typical 0.14 p.u. [59, 60] given the manufacturing cost. The exclusive of the reactive power consumption from the leakage inductance may lead to underestimated device stresses. Therefore, all the discussions should be based on active/reactive power at the Point of Common Coupling (PCC), where the impact of leakage inductance is considered.

The grid voltage at the PCC is used as the reference. Then, the grid voltage and

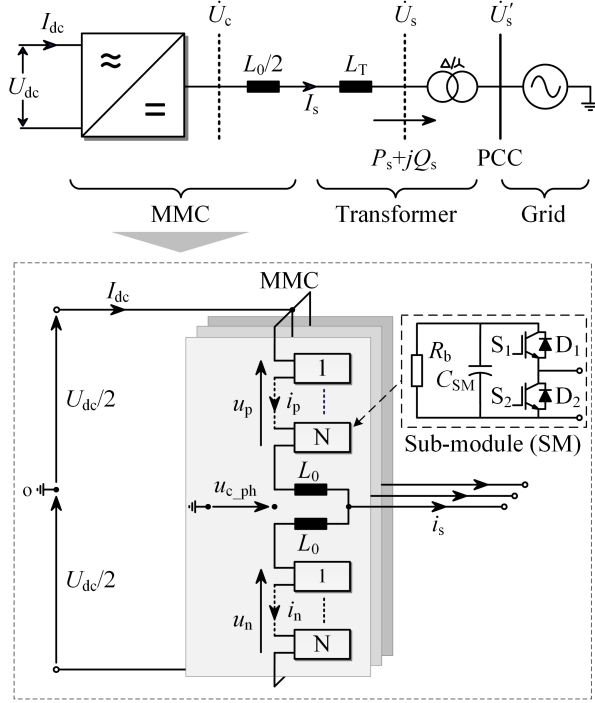


Fig. 2.1: The circuit diagram of an MMC interfaced to an AC system through a transformer [C6].

the line-to-line AC voltage of the converter can be expressed as

$$\hat{U}_s = \hat{U}_s \angle 0^\circ, \hat{U}_c = \hat{U}_c \angle \delta \quad (2.1)$$

where  $\hat{U}_s$  and  $\hat{U}_c$  are amplitudes of the grid and the converter voltages, and  $\delta$  is the power angle, defining the angle between  $U_c$  and  $U_s$ .

The phase inductance is a combination of the transformer leakage and the arm inductors, which is

$$L_{eq} = L_T + L_0/2 \quad (2.2)$$

The modulation index is defined as

$$m = \frac{\hat{U}_{c\_ph}}{U_{dc}/2} \quad (2.3)$$

where  $\hat{U}_{c\_ph}$  is the amplitude of the converter phase voltage,  $U_{dc}$  is the DC bus voltage. The Root-Mean-Square (RMS) line-to-line voltage of the converter is expressed as

$$U_c = \frac{\sqrt{3}}{\sqrt{2}} \hat{U}_{c\_ph} \quad (2.4)$$



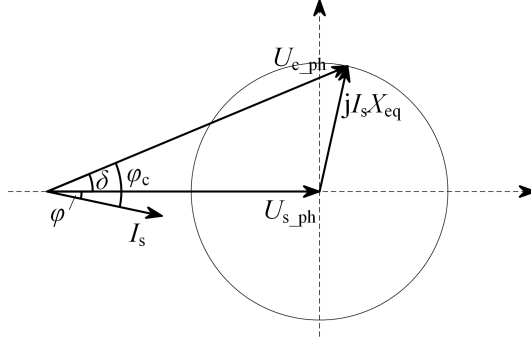


Fig. 2.2: The operation vector diagram of the MMC system shown in Fig. 2.1.

According to [59], the active and reactive power at the PCC is given by

$$\begin{cases} P_s = \frac{U_s U_c \sin \delta}{X_{eq}} \\ Q_s = \frac{U_s (U_c \cos \delta - U_s)}{X_{eq}} \end{cases} \quad (2.5)$$

where  $X_{eq}$  is the impedance of the phase reactance  $L_{eq}$ . Once an AC voltage gain is defined as

$$\lambda = \frac{U_c}{U_s} \quad (2.6)$$

Then, (2.5) can be rewritten as

$$\begin{cases} P_s = \frac{U_s^2 \lambda \sin \delta}{X_{eq}} \\ Q_s = \frac{U_s^2 (\lambda \cos \delta - 1)}{X_{eq}} \end{cases} \quad (2.7)$$

Solving (2.7), the power angle  $\delta$  and the AC voltage gain  $\lambda$  are expressed as

$$\begin{cases} \delta = \arctan \left( \frac{P_s X_{eq}}{U_s^2 + Q_s X_{eq}} \right) \\ \lambda = \frac{Q_s X_{eq} + U_s^2}{U_s^2 \cos \delta} \end{cases} \quad (2.8)$$

Correspondingly, the modulation index is rewritten as

$$m = \frac{2\sqrt{2} \lambda U_s}{\sqrt{3} U_{dc}} = \frac{2\sqrt{2} (Q_s X_{eq} + U_s^2)}{\sqrt{3} U_{dc} U_s \cos \delta} \quad (2.9)$$

in which the modulation index is not changed freely. Conversely, the grid parameters (e.g., reactive power, grid voltage, etc.) determine the range of the modulation index.

Similarly, the power factor, RMS value of the AC and DC currents are expressed as

$$\text{PF} = \cos \varphi = \frac{P_s}{\sqrt{P_s^2 + Q_s^2}} \quad (2.10)$$

$$I_s = \frac{\sqrt{P_s^2 + Q_s^2}}{\sqrt{3}U_s} \quad (2.11)$$

$$I_{\text{dc}} = \frac{P_s}{U_{\text{dc}}} \quad (2.12)$$

Therefore, the phase voltage of the converter and AC current are expressed according to Fig. 2.2, which are

$$u_{\text{c,ph}}(t) = m \frac{U_{\text{dc}}}{2} \sin(\omega t) \quad (2.13)$$

$$i_s(t) = \sqrt{2}I_s \sin(\omega t - \varphi_c) \quad (2.14)$$

where  $\varphi_c$  is the phase angle given by the converter AC voltage, which has  $\varphi_c = \delta + \varphi$ .

In the steady-state, the arm current consists of a fundamental-frequency component and a DC-bias, which are expressed as

$$\begin{cases} i_p(t) = \frac{I_{\text{dc}}}{3} + \frac{\hat{I}_s}{2} \sin(\omega t - \varphi_c) = \frac{\hat{I}_s}{2} [k + \sin(\omega t - \varphi_c)] \\ i_n(t) = \frac{I_{\text{dc}}}{3} - \frac{\hat{I}_s}{2} \sin(\omega t - \varphi_c) = \frac{\hat{I}_s}{2} [k - \sin(\omega t - \varphi_c)] \end{cases} \quad (2.15)$$

where  $k$  is the current ratio in the arm current, which is defined as

$$k = \frac{I_{\text{dc}}}{3} \bigg/ \frac{\hat{I}_s}{2} \quad (2.16)$$

By neglecting the power losses in the MMC,  $k$  is also obtained as

$$U_{\text{dc}} I_{\text{dc}} = \frac{3}{2} \hat{U}_{\text{c,ph}} \hat{I}_s \cos \varphi_c \Rightarrow k = \frac{1}{2} m \cos \varphi_c \quad (2.17)$$

According to Kirchhoff's voltage law, the upper arm and lower arm voltages are given by

$$\begin{cases} u_p = \frac{U_{\text{dc}}}{2} - u_{\text{c,ph}} \\ u_n = \frac{U_{\text{dc}}}{2} + u_{\text{c,ph}} \end{cases} \quad (2.18)$$

Substituting (2.13) into (2.18), the arm voltages are solved as

$$\begin{cases} u_p = \frac{1}{2} [1 - m \sin(\omega t)] U_{\text{dc}} \\ u_n = \frac{1}{2} [1 + m \sin(\omega t)] U_{\text{dc}} \end{cases} \quad (2.19)$$

**Table 2.1:** Specifications and Parameters of a Down-scale MMC Prototype

Parameters and symbols	Values and units
Nominal apparent power $S_N$	15 kVA
Nominal active power $P_N$	13.5 kW
DC bus voltage $U_{dc}$	900 V
Switching frequency $f_{sw}$	1.5 kHz
Leakage reactance of the transformer $L_T$	4 mH (0.12 p.u.)
Arm reactance $L_0$	4 mH (0.12 p.u.)
SM capacitance $C_{SM} = C_1 + C_2$	400 V/820 $\mu$ F $\times 2$
Grid line voltage at PCC $U_s$	380 V
Number of SMs per arm $N$	4
Bleeding resistor of each SM $R_b$	12 k $\Omega$
IGBT module	1.2 kV/50 A (F4-50R12KS4)

In the ideal MMC model, it has the constraint of  $U_{dc} = NU_{SM}$ , where  $N$  is the number of SMs per arm and  $U_{SM}$  is the SM capacitor voltage. The insertion probability of the upper arm and lower arm are denoted by  $N_p$  and  $N_n$ , that is

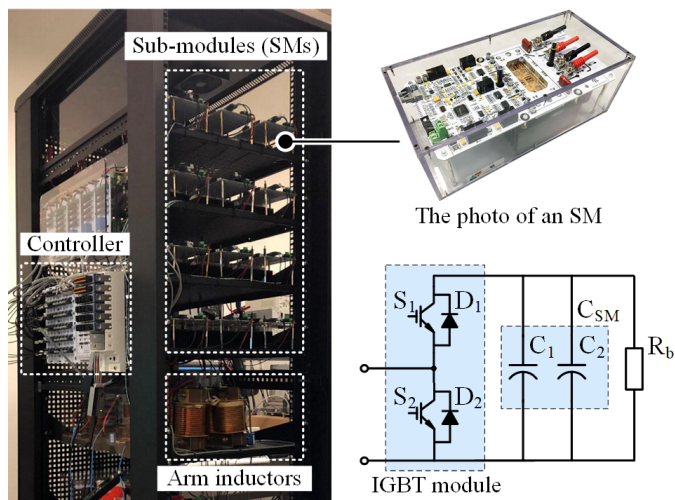
$$\begin{cases} N_p = \frac{u_p}{NU_{SM}} = \frac{1}{2} [1 - m \sin(\omega t)] \\ N_n = \frac{u_n}{NU_{SM}} = \frac{1}{2} [1 + m \sin(\omega t)] \end{cases} \quad (2.20)$$

So far, all the variables inside the MMC converter (e.g., modulation index, arm voltages/currents) has been established the analytical relationship according to the active/reactive power at the PCC.

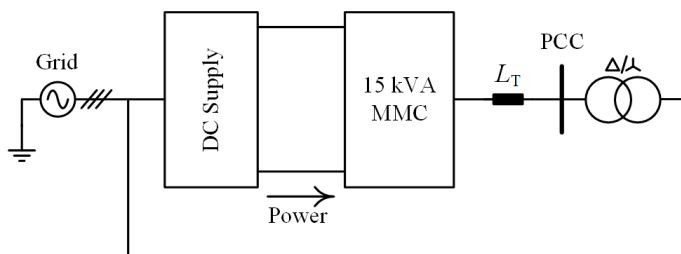
## 2.3 Description of a Down-scale MMC Prototype

In this thesis, a 15 kVA down-scale MMC prototype has been built for experimental verification, as shown in Fig. 2.3. The detailed specifications are listed in Table 2.1. In particular, although the MMC-based HVDC systems commonly employ high-power film capacitors and air-core inductors, the down-scale prototype utilizes the commercial Aluminum Electrolytic Capacitors (Al-Caps) and iron-core inductors due to the volume and power density limitations. It is worth noticing that the Al-Caps and iron-core inductors also offer advantages for medium-power MMC applications [61].

As shown in Fig. 2.4, the  $P/Q$  capability circle shows that selected operational  $P/Q$  ranges are located within a certain limits. In addition, the steady-state waveforms in Fig. 2.5 verify a proper operation of the converter under the nominal condition ( $P = 13.5$  kW and  $Q = 6.5$  kVar).



(a)



(b)

**Fig. 2.3:** A 15 kVA down-scale MMC prototype: (a) a photo of the platform along with the Sub-Module (SM) circuit and (b) the circuit configuration of the setup.

## 2.4 Modeling of the Power Losses of the Critical Components

In the initial design of an MMC, the power losses of many component candidates need to be evaluated quickly. This section provides analytical power loss models for the critical components (i.e., IGBTs, capacitors, inductors, and bleeding resistors). The analytical models utilize only grid-level information (e.g., grid voltages,  $P/Q$  set points at PCC, etc.), which are usually accessible in the initial design stage. Moreover, the selected components are measured to reveal the uneven parameters in practice, which will be taken into account by subsequent reliability evaluation. Finally, the theoretical power loss formulas and experimental results are also compared.

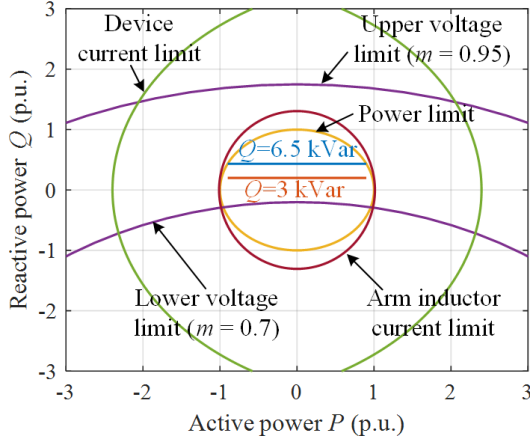


Fig. 2.4:  $P/Q$  capability graph of the down-scale MMC in Fig. 2.3, where the power limit is determined by the maximum apparent power, arm inductor limit is determined by the current rating of the inductor, and the device current limit means the maximum IGBT current, respectively.

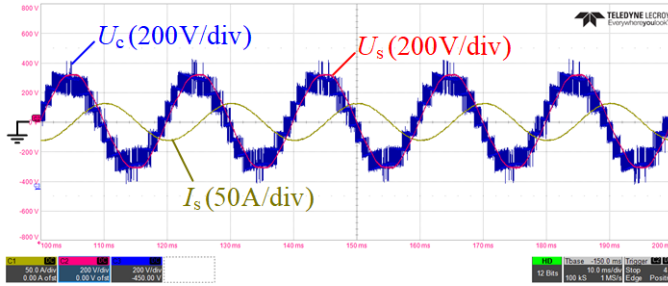


Fig. 2.5: Steady-state MMC waveforms when  $P = 13.5$  kW and  $Q = 6.5$  kVar (the grid voltage, the converter AC voltage, and the current).

## 2.4.1 Power Losses of the IGBT Modules

In the down-scale prototype, a 1200 V/50 A IGBT module is used as the basic component, which has conduction and switching losses. According to [62], the conduction losses of the IGBT/diode can be calculated by

$$P_{\text{cond}} = |I_{\text{avg}}| \left[ U_{\text{cond0@}T_{\text{ref}}} + K_{T1} (T_j - T_{\text{ref}}) \right] + I_{\text{RMS}}^2 \left[ r_{\text{cond0@}T_{\text{ref}}} + K_{T2} (T_j - T_{\text{ref}}) \right], \quad (2.21)$$

with  $U_{\text{cond0@}T_{\text{ref}}}$ ,  $r_{\text{cond0@}T_{\text{ref}}}$ ,  $K_{T1}$  and  $K_{T2}$  being the coefficients obtained experimentally as shown in Fig. 2.6 and listed in Table 2.2, respectively. The reference temperature is  $T_{\text{ref}} = 25^\circ\text{C}$  and  $T_j$  is the junction temperature. In addition,  $I_{\text{avg}}$  and  $I_{\text{RMS}}$  are the average and the RMS currents flowing through the devices, respectively. The switching energy dissipations  $E_{\text{sw}} = E_{\text{on}} + E_{\text{off}}$  for the IGBT, and the reverse recovery

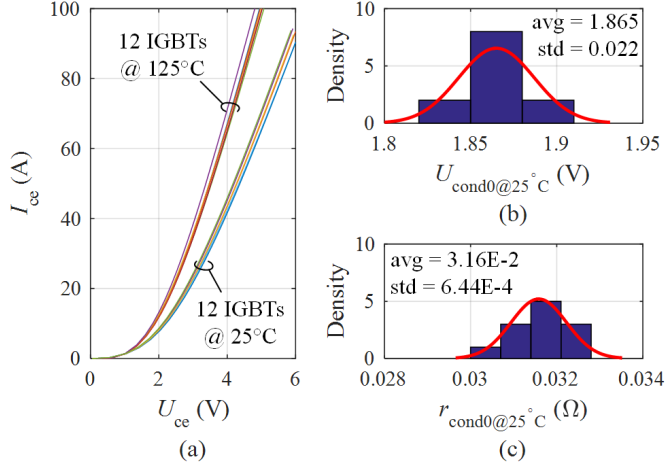


**Fig. 2.6:** Measured conduction losses of 12 IGBT modules (1200 V/50 A): (a) output characteristic of the IGBT, (b) the obtained  $U_{\text{cond0@25}^\circ\text{C}}$  and its distributions and (c) the obtained  $r_{\text{cond0@25}^\circ\text{C}}$  and its distributions.

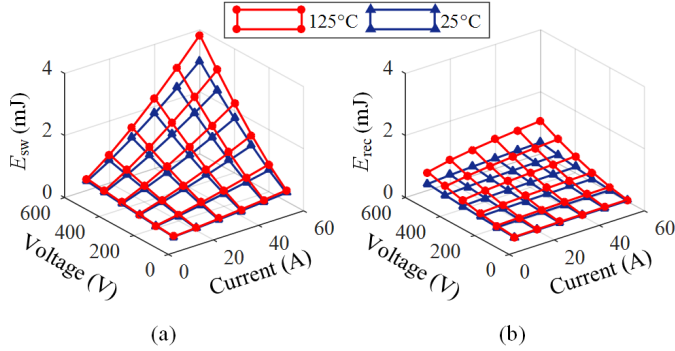


**Fig. 2.7:** Measured switching energy dissipations in the IGBT module (1200 V/50 A): (a) IGBTs and (b) diodes.

energy per pulse  $E_{\text{sw}} = E_{\text{rec}}$  for the freewheeling diode for the current  $I$  are given by

$$E_{\text{sw}} = E_{\text{swref}} \left( \frac{I}{I_{\text{ref}}} \right)^{K_i} \left( \frac{U_{\text{SM}}}{U_{\text{ccref}}} \right)^{K_u} [1 + K_{\text{sw}} (T_j - T_{\text{ref}})], \quad (2.22)$$

with  $I_{\text{ref}}$ ,  $U_{\text{ccref}}$  and  $E_{\text{swref}}$  being the nominal test conditions.  $K_i$ ,  $K_u$  and  $K_{\text{sw}}$  are the coefficients obtained from the measurements as shown in Fig. 2.7 and also listed Table 2.2, respectively.  $U_{\text{SM}}$  is the SM capacitor voltage.

Subsequently, the average switching losses are

$$P_{\text{sw}_S/D} = \frac{1}{T} \sum_{t_0}^{t_0+T} E_{\text{sw}}(i_{\text{CE}/f}), \quad (2.23)$$

**Table 2.2:** Measured Power Loss Coefficients for the Selected IGBT Modules (avg: average values, std: standard deviations)

		IGBT		Diode	
		avg	std	avg	std
$U_{\text{cond}0@T_{\text{ref}}}$	[V]	1.87	2.2E-2	1.31	2.5E-2
$r_{\text{cond}0@T_{\text{ref}}}$	[ $\Omega$ ]	3.16E-2	6.4E-4	1.46E-2	5.2E-4
$K_{T1}$	[V/ $^{\circ}\text{C}$ ]	2.70E-3	1.7E-4	-3.3E-3	4.2E-4
$K_{T2}$	[ $\Omega$ / $^{\circ}\text{C}$ ]	9.73E-5	1.1E-5	1.82E-5	2.9E-6
$K_i$	[1]	1.30	2.2E-2	3.32E-1	5.5E-3
$K_u$	[1]	1.33	2.2E-2	1.72	2.9E-2
$K_{\text{sw}}$	[1/ $^{\circ}\text{C}$ ]	2.76E-3	4.6E-5	1.84E-2	3.1E-4

\*for IGBT,  $E_{\text{swref}}=0.72$  mJ,  $I_{\text{ref}}=20$  A,  $U_{\text{ccref}}=300$  V;

\*for Diode,  $E_{\text{swref}}=0.26$  mJ,  $I_{\text{ref}}=20$  A,  $U_{\text{ccref}}=300$  V.

**Table 2.3:** The Average and RMS Currents of the Power Devices in an SM of the MMC

Device	Average current (A)
$S_1$	$\frac{\hat{I}_s}{4\pi} (k^2 - 1) \cos \alpha$
$D_1$	$\frac{\hat{I}_s}{4\pi} (1 - k^2) \cos \alpha$
$S_2$	$\frac{\hat{I}_s}{4\pi} [(\pi + 2\alpha)k + (1 + k^2) \cos \alpha]$
$D_2$	$\frac{\hat{I}_s}{4\pi} [(\pi - 2\alpha)k - (1 + k^2) \cos \alpha]$
Device	The power of RMS current ( $\text{A}^2$ )
$S_1$	$\frac{\hat{I}_s^2}{16\pi} \left[ \left( \frac{1}{2} - k^2 \right) (\pi - 2\alpha) - \frac{k}{3} \cos(3\alpha) \right]$
$D_1$	$\frac{\hat{I}_s^2}{16\pi} \left[ \left( \frac{1}{2} - k^2 \right) (\pi + 2\alpha) + \frac{k}{3} \cos(3\alpha) \right]$
$S_2$	$\frac{\hat{I}_s^2}{16\pi} \left[ \left( \frac{1}{2} + 3k^2 \right) (\pi + 2\alpha) + 6k \cos \alpha - \frac{k}{3} \cos(3\alpha) \right]$
$D_2$	$\frac{\hat{I}_s^2}{16\pi} \left[ \left( \frac{1}{2} + 3k^2 \right) (\pi - 2\alpha) - 6k \cos \alpha + \frac{k}{3} \cos(3\alpha) \right]$

where  $P_{\text{sw}_S/D}$  and  $i_{\text{CE}/f}$  are the average switching losses and the instantaneous device currents for IGBTs or diodes, respectively.

Based on (2.21), the key task to calculate the power losses of the IGBT module is to find the instantaneous, the average and the RMS currents of the power device. Solving (2.15), the zero crossing points of the arm current are at

$$\begin{cases} \omega t_1 = -\alpha + \varphi_c \\ \omega t_2 = \pi + \alpha + \varphi_c \end{cases} \quad \text{where } \alpha = \arcsin(k), \quad (2.24)$$

when the arm current is positive (i.e.,  $\omega t_1 \leq \omega t < \omega t_2$ ), it flows through the devices  $D_1$  and  $S_2$ . On the contrary, the arm current passes through the devices  $S_1$  and  $D_2$  when the current is negative. The instantaneous current  $i_{\text{CE}_S1}$ , the average current  $I_{S1\_avg}$  and the RMS current  $I_{S1\_RMS}$  of the device  $S_1$  are calculated as

$$i_{\text{CE}_S1} = \begin{cases} 0, & 2\pi + \omega t_1 \leq \omega t < \omega t_2 \\ N_p i_p, & \omega t_2 \leq \omega t < 2\pi + \omega t_1, \end{cases} \quad (2.25)$$

$$I_{S1\_avg} = \frac{1}{2\pi} \int_{\omega t_2}^{2\pi + \omega t_1} N_p i_p d\omega t = \frac{\hat{I}_s}{4\pi} (k^2 - 1) \cos \alpha, \quad (2.26)$$

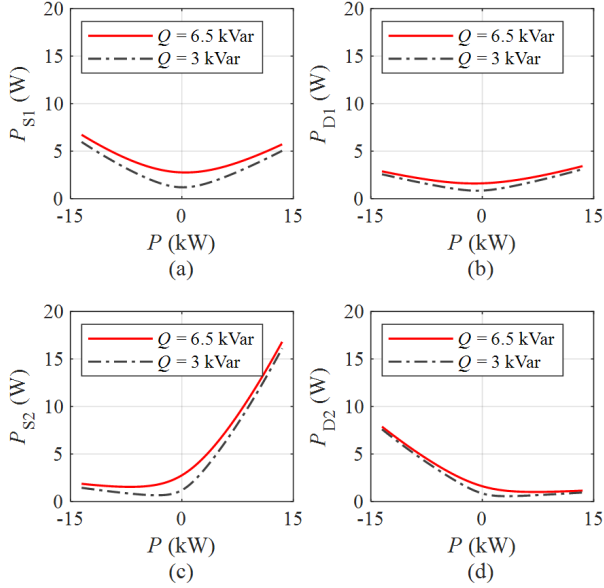


**Fig. 2.8:** The power losses of the semiconductor devices in an SM ( $P > 0$  inverter mode,  $P < 0$  rectifier mode): (a)  $S_1$ , (b)  $D_1$ , (c)  $S_2$  and (d)  $D_2$ .

$$I_{S1\_RMS}^2 = \frac{\int_s^2}{16\pi} \left[ \left( \frac{1}{2} - k^2 \right) (\pi - 2\alpha) - \frac{k}{3} \cos(3\alpha) \right]. \quad (2.27)$$

The device currents of  $S_2$ ,  $D_1$  and  $D_2$  are obtained similarly as listed in Table 2.3. Substituting the device currents into (2.21) and (2.23), the average power losses of the power devices are obtained.

Based on the established models, the power losses under various  $P/Q$  setpoints are shown in Fig. 2.8. When  $P > 0$  (inverter mode), the DC-bias current flows through the devices  $S_2$  and  $D_1$ , which leads to higher power losses. On the contrary, devices  $D_2$  and  $S_1$  dominate the power losses when  $P < 0$  (rectifier mode). Moreover, when the reactive power is reduced from 6.5 kVar to 3 kVar, the power losses of the all-power devices are alleviated correspondingly.

## 2.4.2 Power Losses of Capacitors

According to [63], the power losses of a capacitor are expressed by the RMS capacitor current  $I_{cap\_RMS}$  and capacitor series resistance  $ESR_{cap}$ , which are expressed by

$$P_{cap} = \sum_{\omega=0}^{\infty} I_{cap\_RMS}^2(\omega) \cdot ESR_{cap}(\omega). \quad (2.28)$$



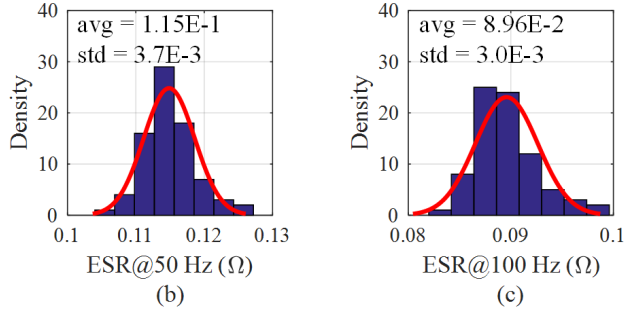
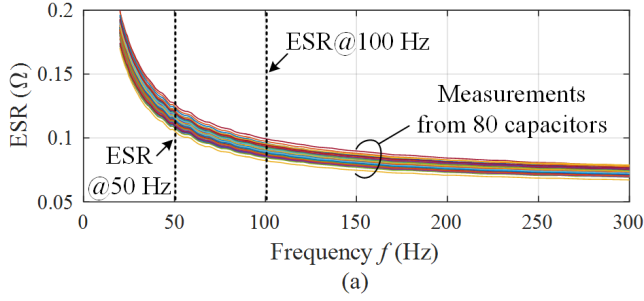


**Fig. 2.9:** The measurements of 80 capacitor series resistances under different frequencies: (a) The capacitor series resistance, (b) the distribution of  $\text{ESR}_{\text{cap}}$  at 50 Hz and (c)  $\text{ESR}_{\text{cap}}$  at 100 Hz.

The capacitor current of the MMC mainly consists of the 1<sup>st</sup>- and the 2<sup>nd</sup>-order components [44], whose amplitudes are

$$\hat{I}_{\text{cap}}(\omega) = \frac{\hat{I}_s}{4} \sqrt{m^2 k^2 - 2m \cos \varphi_c + 1}, \quad (2.29)$$

$$\hat{I}_{\text{cap}}(2\omega) = \frac{m \hat{I}_s}{8}. \quad (2.30)$$

The measured capacitor series resistance versus frequency for 80 capacitors is shown in Fig. 2.9, which decreases progressively with the frequency with sensible differences for those 80 capacitors. The measured  $\text{ESR}_{\text{cap}}$  is 115 m $\Omega$  (50 Hz) and 89.6 m $\Omega$  (100 Hz) on the average, respectively.

Substituting (2.29), (2.30) and the  $\text{ESR}_{\text{cap}}$  into (2.28), the corresponding capacitor losses are obtained as shown in Fig. 2.10. The 1<sup>st</sup>- and 2<sup>nd</sup>-order capacitor currents are symmetrical with respect to  $P = 0$  axis. However, the 1<sup>st</sup>-order capacitor current is approximately four times the 2<sup>nd</sup> order, indicating that the capacitor power losses are mainly produced by the 1<sup>st</sup>-order component. Moreover, both the capacitor currents and the power losses decrease as the reactive power demand decreases.

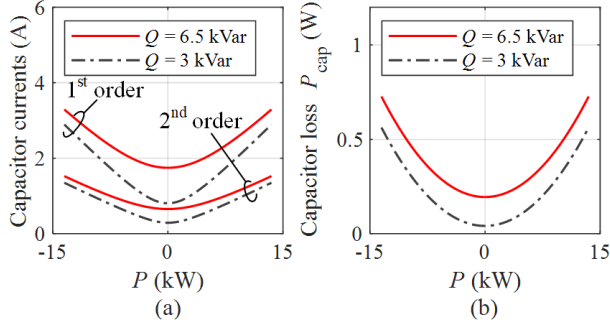


Fig. 2.10: Capacitor currents and power losses for a capacitor in an SM: (a) 1<sup>st</sup>- and 2<sup>nd</sup>-order capacitor currents and (2) capacitor power losses.

### 2.4.3 Power Losses of the Arm Inductors

The down-scale prototype uses iron-core arm inductors. The inductor power losses  $P_{\text{armL}}$  consist of winding losses  $P_w$  and core losses  $P_{\text{core}}$ . The winding losses depend on the resistance of each conducting element and the RMS current that flows through it, which are

$$P_w = \sum_{\omega=0}^{\infty} i_{p/n\_RMS}^2(\omega) R_{sL}(\omega) = \frac{\hat{i}_s^2 k^2}{4} R_{sL\_dc} + \frac{\hat{i}_s^2}{8} R_{sL\_ac}, \quad (2.31)$$

where  $i_{p/n\_RMS}$  is the RMS value of the upper/lower arm current and  $R_{sL}$  is the equivalent series resistance of the arm inductor. In the 6 arm inductors, the measured  $R_{sL}$  increases against the frequency as shown in Fig. 2.11, where the resistances are 64.4 m $\Omega$  (0 Hz) and 66.9 m $\Omega$  (50 Hz) on average, respectively.

According to [64], the core losses of the arm inductors are excited by the sinusoidal current with a DC-bias, which are

$$P_{\text{core}} = \left( C_{dc} K_h f \hat{B}^2 + K_c f^2 \hat{B}^2 + K_e f^{1.5} \hat{B}^{1.5} \right) \cdot V_c, \quad (2.32)$$

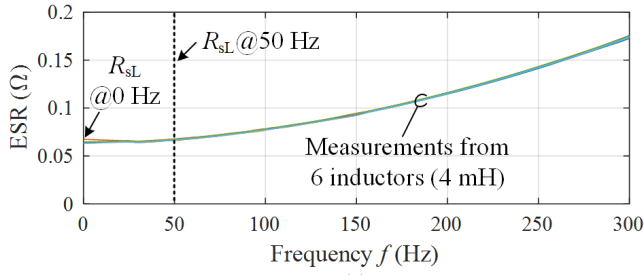
where  $\hat{B}$  is the amplitude of the AC flux,  $K_h$ ,  $K_c$  and  $K_e$  are the hysteresis, the eddy-current and the excess core loss coefficients, respectively.  $V_c$  is the core volume, and  $C_{dc}$  considers the impact of the DC-bias current.

The arm current and power losses are shown in Fig. 2.12. The arm current is dominated by the 1<sup>st</sup>-order component as shown in Fig. 2.12(a). Meanwhile, the DC component of the arm current is independent of reactive power. Finally, the power losses of the arm inductor are correspondingly shown in Fig. 2.12(b).

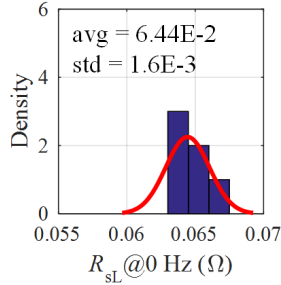
### 2.4.4 Power Losses of the Bleeding Resistors

The bleeding resistors are connected in parallel with the SM capacitors. The power losses of a bleeding resistor are voltage dependent as

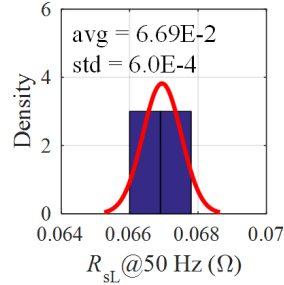
$$P_R = \frac{U_{SM}^2}{R_b}. \quad (2.33)$$



(a)

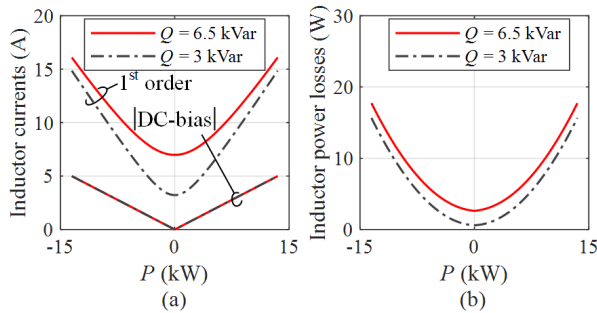


(b)



(c)

**Fig. 2.11:** The measured equivalent series resistance of 6 arm inductors: (a) inductor series resistances, (b) the parameter distribution at 0 Hz and (c) the distribution at 50 Hz.



(a)

(b)

**Fig. 2.12:** The arm inductor currents and power losses: (a) DC and 50-Hz components of the arm current, (b) power losses of an arm inductor.

According to the measured parameter distribution of the selected bleeding resistors shown in Fig. 2.13(a), the average resistance is 12.03 k $\Omega$ . Due to the mean value of the capacitor voltage, which is independent of the active/reactive powers, the corresponding power losses are almost constant under different  $P/Q$  values, which are shown in Fig. 2.13(b).

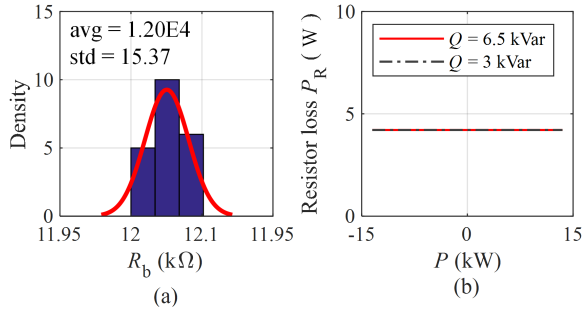
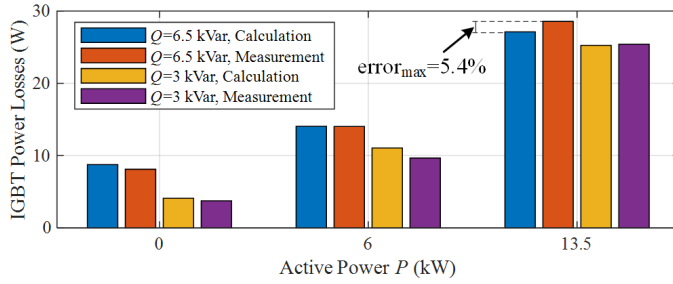


**Fig. 2.13:** The parameter distribution and the power losses of the bleeding resistors: (a) the measured resistance distribution and (b) the power losses of the bleeding resistor under different  $P/Q$  set points.

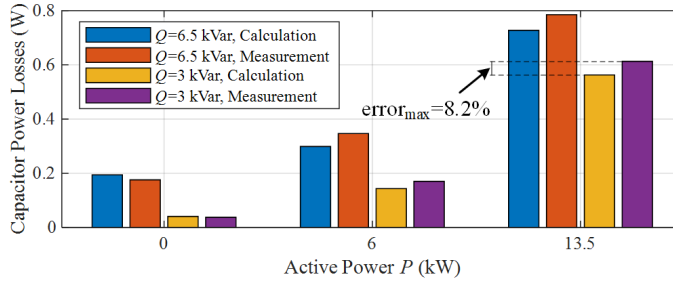
## 2.5 Experimental Verifications

The power losses of the components mentioned above are measured by the Newtons Power Analyzer PPA5500, and the measured results are compared to the theoretical values, as shown in Fig. 2.14. Since it is difficult to measure the power losses of a single power semiconductor chip, the entire IGBT module is measured. The total power losses of the four power devices (i.e.,  $S_1$ ,  $S_2$ ,  $D_1$  and  $D_2$ ) are shown in Fig. 2.14(a). The measurements coincide with the theoretical values with a maximum error of 5.4%. Next, a comparison of the measured capacitor power losses and the theoretical values are shown in Fig. 2.14(b). The capacitor power losses are relatively small in this case, where the maximum value is roughly 0.8 W. The experimental power loss data also agrees with the theoretical values with a maximum error of 8.2%. This kind of error might come from the switching-frequency ripple currents, which are neglected in the analytical models. Furthermore, the power losses of the arm inductor are shown in Fig. 2.14(c). The theoretical power losses are relatively small when  $P = 0$  kW, while the theoretical results become larger when  $P = 13.5$  kW. The differences are probably from the core loss model without considering the harmonics. When  $P = 0$  kW, the inductor current is minimal. The error of core losses due to harmonics accounts for a large part, which leads to a large error. However, the difference of around 3 W under the condition is still acceptable. Moreover, MMC applications usually utilize air-core inductors. The error from core losses contributes to a minor effect in real applications. However, for more accurate results, a more comprehensive inductor power loss model is required.

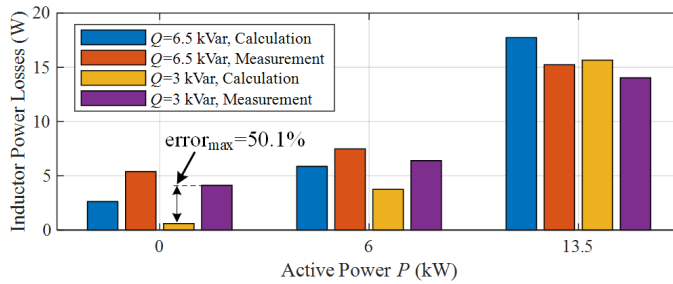
So far, the system-level power loss model has been established for the MMC. Both the device parameters and mission profiles (i.e.,  $P/Q$  set points at PCC) are considered. The corresponding outcomes provide the basis for the next thermal analysis and lifetime prediction.



(a)



(b)



(c)

**Fig. 2.14:** Comparison of the theoretical power losses and the measurements: (a) IGBT module, (b) capacitor and (c) arm inductor.

## 2.6 Summary

To achieve the reliability oriented design of the MMC, a systematical power loss evaluation of the MMC is modeled. This chapter has established the analytical models of the power losses of the power semiconductor devices, capacitors, inductors, and bleeding resistors. All the electrical parameters are based on the  $P/Q$  set points with PCC of the grid. It enables a computation-light and parameter-changing friendly model. The proposed model is validated by a 15-kVA down-scale prototype experimentally.



# Chapter 3

## Comprehensive Electro-thermal Model of the MMC

### 3.1 Abstract

According to [12], thermal-related issues are one of the most severe failure mechanisms for power electronic applications. Thus, the electro-thermal model is an essential part to discuss the reliability of the MMC systems. The electro-thermal model serves to convert the mission profiles into thermal profiles, which is directly related to the accumulated damages of devices and systems. Therefore, this chapter discusses the four different aspects as follows.

- The classification of typical thermal profiles in power electronic systems;
- Periodic thermal profiles of MMCs;
- Non-periodic thermal profiles of MMCs;
- Impact of Thermal Interface Materials (TIMs) and an empirical characterization model.

### 3.2 Classification of Typical Thermal Profiles

In terms of long-term reliability assessment of power electronic systems, one of the most challenging aspects is to convert the thermal profiles across multiple time scales, i.e., from switching cycles at the nano- or micro-seconds to the mission profile with a year or even longer time duration [C5]. In general, the thermal profiles of power electronic applications typically contain two major categories, as shown in Fig. 3.1:

- **Periodic Profiles:** thermal cycles due to the periodic power loss profiles, which are related to the fundamental-frequency currents or switching. In different

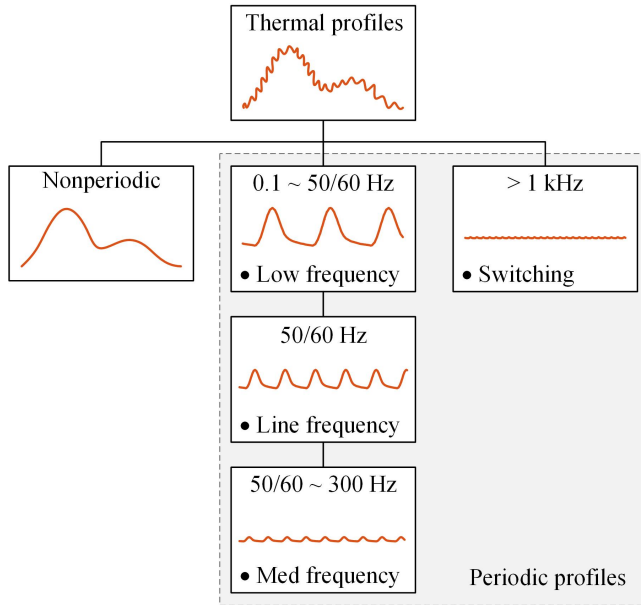


Fig. 3.1: Typical thermal profiles in power electronic systems [C5].

applications, the periodic profiles may have four different frequency ranges: low frequencies (low-speed variable applications), line frequencies (utilities), medium frequencies (high-speed motor drive), and also switching frequencies.

- **Non-periodic Profiles:** thermal swings due to the load variations and environments also exist. The time scales are typically seconds, minutes, days, or even longer.

Thermal behaviors under different time scales usually have distinctive performances. Thus, a single thermal model is challenging to provide good thermal estimation across multi-time scales. A compromise of computational burdens and accuracy is usually inevitable based on a single electro-thermal model. Therefore, it is necessary to distinguish the thermal behaviors of different time scales.

### 3.2.1 Time-domain Thermal Profile Analysis

In the case of an IGBT module as shown in Fig. 3.2, the power dissipation in a chip is not only heating up itself, but also increases the temperatures of the neighboring



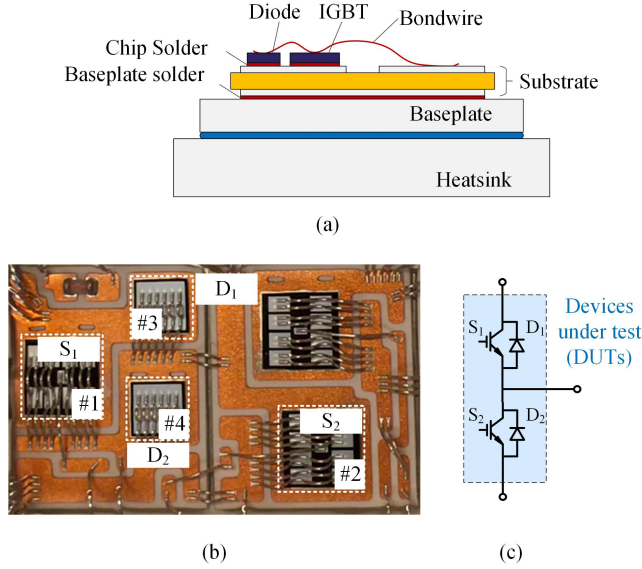


**Fig. 3.2:** Studied power module used for the MMC: (a) lateral structure; (b) horizontal distribution of chips and (c) circuit diagram [C5].

chips. Then, a thermal matrix is usually utilized to define the process, that is

$$\begin{aligned}
 & \begin{bmatrix} T_{j1}(t) \\ T_{j2}(t) \\ \vdots \\ T_{jn}(t) \end{bmatrix} \\
 = & \begin{bmatrix} Z_{th,11}(t) & Z_{th,12}(t) & \cdots & Z_{th,1n}(t) \\ Z_{th,21}(t) & Z_{th,22}(t) & \cdots & Z_{th,2n}(t) \\ \vdots & \vdots & \ddots & \vdots \\ Z_{th,n1}(t) & Z_{th,n2}(t) & \cdots & Z_{th,nn}(t) \end{bmatrix} \begin{bmatrix} P_1(t) \\ P_2(t) \\ \vdots \\ P_n(t) \end{bmatrix} + T_r \quad (3.1) \\
 = & (\mathbf{Z}_{th,self} + \mathbf{Z}_{th,mutual}) \cdot \mathbf{P} + T_r
 \end{aligned}$$

where  $T_j(t)$  is the junction temperature of each power semiconductor chip,  $P(t)$  is the corresponding power losses in the chip, and  $T_r$  is the reference temperature (e.g., case temperature, ambient temperature, etc). The diagonal elements  $Z_{th,ii}(t)$  correspond to the self thermal impedances of each heat source (i.e., chip), and non-diagonal elements  $Z_{th,ii}(t)$  denote mutual thermal impedances among chips. Clearly, the number of heat sources (e.g., chips) determines the dimension of the applied thermal matrix. For instance, a typical medium-voltage IGBT module, e.g., Infineon FF1000R17IE4 has 24 chips, which correspond to a  $24 \times 24$  thermal matrix. The high dimensional thermal matrix is complicated for long-term reliability evaluation. For the MMC with hundreds to thousands of components, it is more challenging to applied the thermal

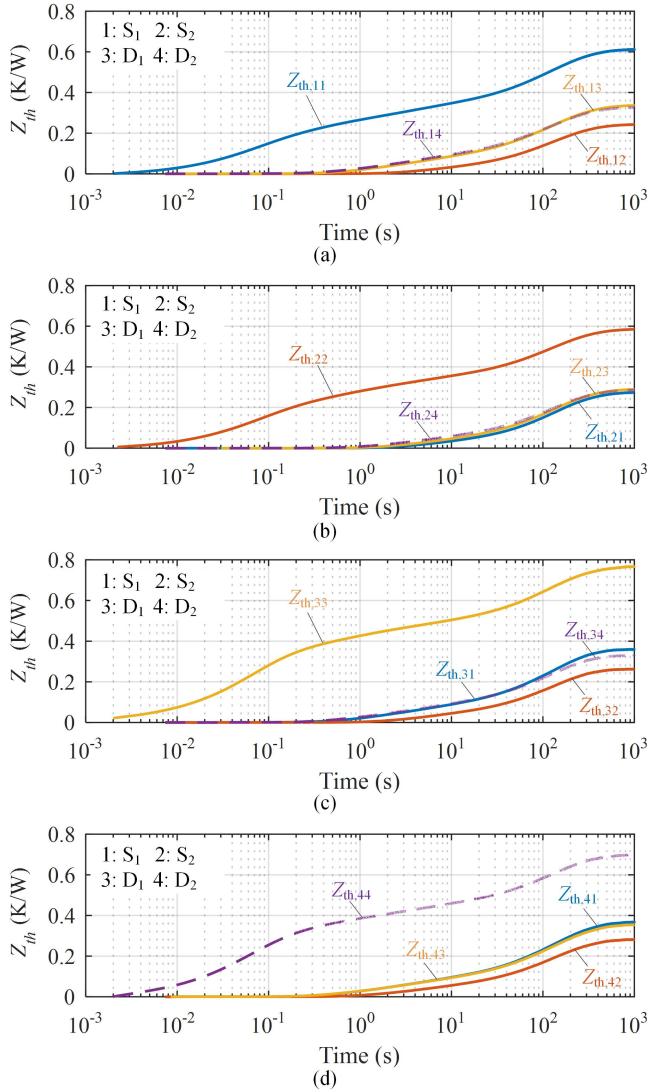


**Fig. 3.3:** Measured time-domain thermal impedance results to establish a thermal matrix of the selected power module [C5].

matrix with such dimensions. Therefore, a comprehensive method is necessary to convert the thermal profiles from different time scales.

As shown in Fig. 3.2, a half-bridge IGBT module consists of two IGBT chips and free-wheeling diode chips. According to the aforementioned thermal matrix, the measured the thermal impedance of each chip is shown in Fig. 3.3. In the time-scale response, the self thermal impedance  $Z_{ii}$  always has a faster response and a larger

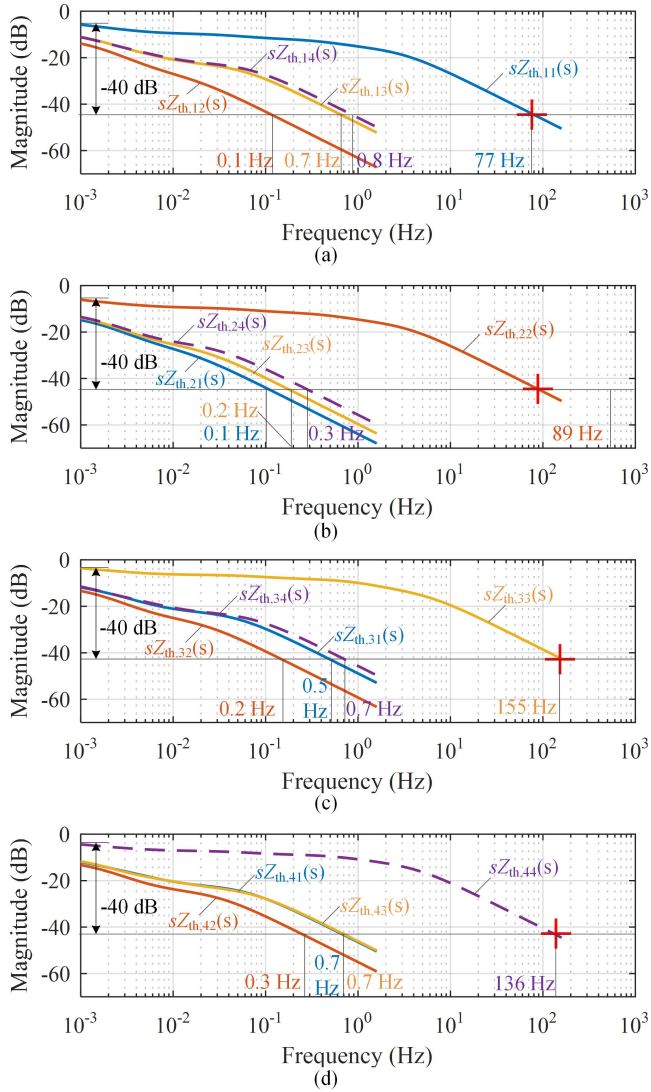


Fig. 3.4: Frequency-domain thermal impedances of the selected IGBT module [C5].

amplitude than the mutual thermal impedance  $Z_{ij}$ . The different time-domain thermal impedance implies the different junction temperatures. However, it is not trivial to find a rule to simplify the thermal matrix based on the obtained time-domain responses [C5].

### 3.2.2 Frequency-domain Thermal Profile Analysis

According to (3.1), the junction temperature of the first chip  $T_{j1}$  is converted into frequency domain, which is expressed as

$$T_{j1}(s) = Z_{th,11}(s) P_1(s) + Z_{th,12}(s) P_2(s) + \dots + Z_{th,14}(s) P_4(s) \quad (3.2)$$

When it comes to the junction temperature of a single chip (e.g.,  $T_{j1}$ ), the mutual thermal impedances (e.g.,  $Z_{th,12}$ ,  $Z_{th,13}$ ,  $Z_{th,14}$ ) are always smaller than the self-impedances (e.g.,  $Z_{th,11}$ ) as shown in Fig. 3.3. In other words, the self-impedance dominates the thermal response. Thus, the expression of (3.2) can be divided by the steady-state value of the self-impedance  $Z_{th,11}(0)$ , which is obtained as

$$T_{j1}(s) = Z_{th,11}(0) \left[ \frac{Z_{th,11}(s)}{Z_{th,11}(0)} P_1(s) + \frac{Z_{th,12}(s)}{Z_{th,11}(0)} P_2(s) + \dots + \frac{Z_{th,14}(s)}{Z_{th,11}(0)} P_4(s) \right] \quad (3.3)$$

For a specific power loss (e.g.,  $P_1(s)$ ), if the magnitude of  $Z_{th,11}(s)/Z_{th,11}(0)$  is smaller than -40 dB at a specific frequency, the corresponding temperature response will be less than 1% of the steady-state response of the self-impedance. Thus, the -40 dB related frequency is defined as a corner frequency in the case. Any thermal profiles over the corner frequency can be negligible since a small thermal response.

Based on the corner frequency, the non-periodic profiles with frequencies larger than 1 Hz have significant effects from both self and mutual thermal impedances, as shown in Fig. 3.4. When it comes to the periodic profiles with the frequency range of 1-100 Hz, the self-thermal impedance is still remarkable while the mutual thermal impedances are gradually minor. Furthermore, for the switching frequency over 1 kHz, neither self nor mutual thermal impedances are significant. It is reasonable to neglect the corresponding thermal responses from the switching frequencies. Therefore, for the studied IGBT module, both self- and mutual-thermal impedances are required for non-periodic profiles. Conversely, periodic profiles (1-100 Hz) are accepted when self-thermal impedances are considered only. The thermal responses due to the switching are negligible.

### 3.3 Periodic Power Loss Profiles of MMCs

Based on the aforementioned frequency-domain thermal analysis, the typical periodic profiles do not need to consider the mutual thermal effects among different devices. However, as shown in Fig. 3.5, the power losses of four power devices in an SM are unbalanced. The average power losses of  $S_2$  and  $D_1$  are larger than that of  $S_1$  and  $D_2$ . Moreover, the loss durations of the instantaneous power losses of  $S_2$  and  $D_1$  are also different from  $S_1$  and  $D_2$ . This inherent power loss unbalance is caused by the DC-bias component of the arm current, which has also been discussed in Chapter 2. Notably, the unbalanced power losses are not constant, which varies with the different operational conditions of the MMC. Thus, it is challenging to directly obtain the

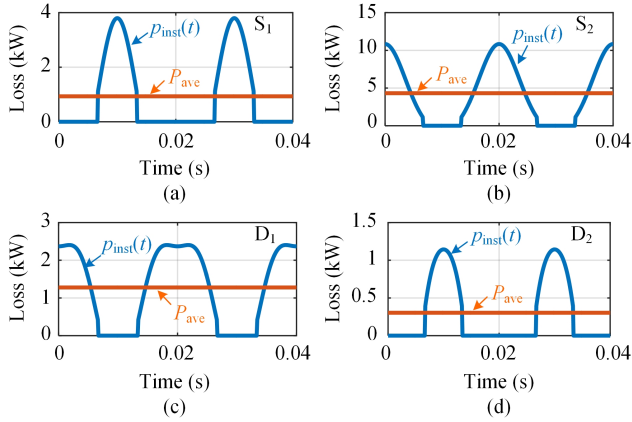


**Fig. 3.5:** Instantaneous power losses  $p_{\text{inst}}(t)$  of four power devices in an SM of a 30-MW MMC case and their corresponding average power losses  $P_{\text{ave}}$ : (a)  $S_1$ , (b)  $S_2$ , (c)  $D_1$ , and (d)  $D_2$  [J3].

**Table 3.1:** Proposed Equivalent Loss Curves for the Power Devices in an SM of the MMC [J1].

Arm currents	Devices	Loss duration	$f_e$	$P_{\text{peak}}$ of the average power loss
$i_p > 0$	$S_2, D_1$	$\pi + 2\alpha$	$\frac{\pi}{\pi+2\alpha} f_0$	$\frac{\pi^2}{(\pi+2\alpha)} P_{\text{ave}}$
	$S_1, D_2$	$\pi - 2\alpha$	$\frac{\pi}{\pi-2\alpha} f_0$	$\frac{\pi^2}{(\pi-2\alpha)} P_{\text{ave}}$
$i_n > 0$	$S_2, D_1$	$\pi + 2\alpha$	$\frac{\pi}{\pi+2\alpha} f_0$	$\frac{\pi^2}{(\pi+2\alpha)} P_{\text{ave}}$
	$S_1, D_2$	$\pi - 2\alpha$	$\frac{\pi}{\pi-2\alpha} f_0$	$\frac{\pi^2}{(\pi-2\alpha)} P_{\text{ave}}$

accurate instantaneous power losses of the devices and then convert them into corresponding thermal profiles. Simplified thermal modeling is necessary to model the periodic power loss profiles, which will be discussed from the following two parts: 1) propose an equivalent loss curve to model the impact of the DC-bias current, and 2) simplify the equivalent loss curve with a quantitative error level.

### 3.3.1 Equivalent Power Loss Profile

As mentioned above, the instantaneous power loss profiles of power devices in the MMC are complicated to be obtained, which varies with different devices, operational conditions, etc. In order to simplify them for thermal estimation, an equivalent power loss curve is proposed here, which should meet two requirements: 1) have identical loss profile duration and 2) have the same average energy or power losses. First, the proposed equivalent power loss curve is given by

$$p_{\text{equi\_inst}} = \begin{cases} P_{\text{peak}} \sin(2\pi f_e t), & p_{\text{equi\_inst}} > 0 \\ 0, & p_{\text{equi\_inst}} \leq 0 \end{cases} \quad (3.4)$$

where  $P_{\text{peak}}$  is the amplitude power loss, and  $f_e$  is the equivalent frequency to characterize the impact of the loss profile duration. Then, the following tasks are to

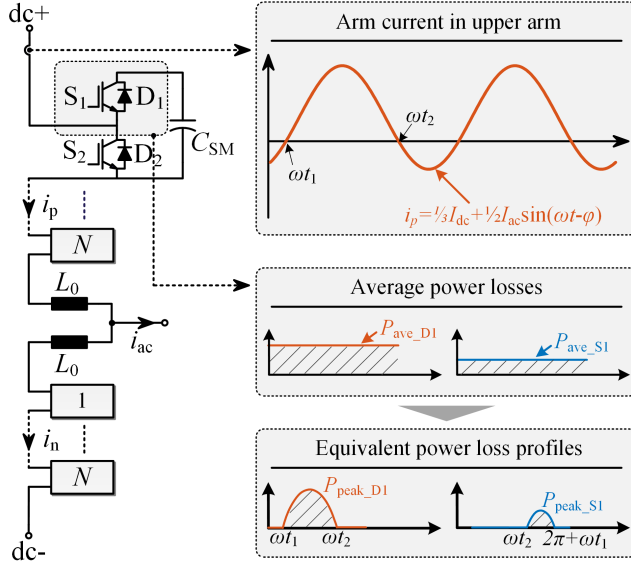


**Fig. 3.6:** Proposed equivalent power loss profile for the power semiconductor devices in the MMC, where the zero-crossing points  $z_{p1}$  and  $z_{p2}$  of the arm current determine the frequencies of the equivalent loss curves [J3].

determine the two parameters.

As shown in Fig. 3.6, the zero crossing points of the arm current determine the duration of the equivalent loss profiles, and further the frequencies. According to the calculated two zero points of the arm currents expressed in (2.24), the position of the zero crossing points depends on two operational parameters of the MMC, i.e., the phase-shift angle  $\varphi$  and the modulation index  $m$ . Thus, the equivalent frequencies can be expressed as

$$\begin{cases} f_{e1} = \frac{\pi}{\pi + 2\alpha} f_0, & \text{for } D_1, \\ f_{e2} = \frac{\pi}{\pi - 2\alpha} f_0, & \text{for } S_1. \end{cases} \quad (3.5)$$

Apart from the consideration of the power-loss duration time, the second aspect is to keep the same energy dissipation. Based on an integral calculation, the relationship between the amplitude  $P_{\text{peak}}$  and the average  $P_{\text{ave}}$  of the devices  $D_1$  and  $S_1$  (see Fig. 3.6) can be expressed as

$$\begin{cases} P_{\text{peak}_D1} = \frac{\pi^2}{(\pi + 2\alpha)} P_{\text{ave}} \\ P_{\text{peak}_S1} = \frac{\pi^2}{(\pi - 2\alpha)} P_{\text{ave}} \end{cases} \quad (3.6)$$

Until now, the parameters as mentioned in (3.4) are obtained by (3.5) and (3.6). Correspondingly, the equivalent loss curves of the devices  $S_2$ ,  $D_2$  are obtained and listed

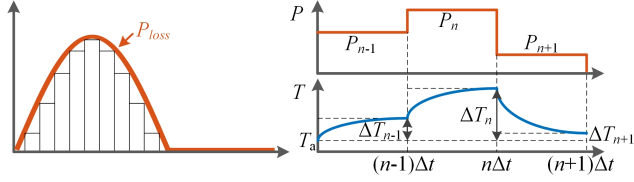


**Fig. 3.7:** Conversion process from the proposed equivalent loss curve into the temperature profile [J1].

**Table 3.2:** Specifications of a Full-Scale MMC System for Sensitivity Analysis of the Proposed Equivalent loss curves[J1].

Parameters	Values
System rated active power	$P = 30$ MW
Rated DC-link voltage	$U_{dc} = 31.8$ kV
Rated AC grid voltage	$U_{ac} = 14$ kV
Number of sub-modules per arm	$N = 12$
Arm inductor	$L_0 = 4$ mH
Arm resistor	$R_0 = 0.0628$ $\Omega$
Sub-module capacitor	$C_{SM} = 0.8$ mF
Switching frequency	$f_{sw} = 1$ kHz

in Table 3.1. The equivalent loss curves are different from the devices in an SM, but the upper and lower arms have the identical results according to Table 3.1.

Furthermore, the proposed equivalent loss profile is divided into a series of pulses, as shown in Fig. 3.7. The temperature of each dissipation pulse is determined by the previous temperature state and the present power loss value of the pulse as described in [65], which is given by

$$\begin{cases} \Delta T_{n-1} = P_{n-1} \sum_{v=1}^3 R_{thv} \left( 1 - e^{-\frac{\Delta t}{\tau_{thv}}} \right) \\ \Delta T_n = \sum_{v=1}^3 \Delta T_{n-1,v} e^{-\frac{\Delta t}{\tau_{thv}}} + P_n \sum_{v=1}^3 R_{thv} \left( 1 - e^{-\frac{\Delta t}{\tau_{thv}}} \right) \end{cases} \quad (3.7)$$

where  $R_{thv}$  is thermal resistance and  $\tau_{thv}$  is thermal time constant, which can be found in datasheet.  $P_{n-1}$  and  $P_n$  are the power losses in the previous and present states, respectively.  $\Delta t$  is the time period of each dissipated period.

### 3.3.2 Parameter Sensitivity Analysis

According to (3.5) to (3.6), the proposed equivalent loss profile has two factors  $P_{peak}$  and  $f_e$ , which are correlated to the modulation index  $m$  and the power factor angle  $\varphi$ . Thus, it is necessary to analyze the parameter sensitivity, where the discussion is based on a full-scale MMC as listed in Table 3.2.

A comparison between the thermal profiles based on the equivalent loss profile and the instantaneous losses are shown in Fig. 3.8. When the fundamental frequency

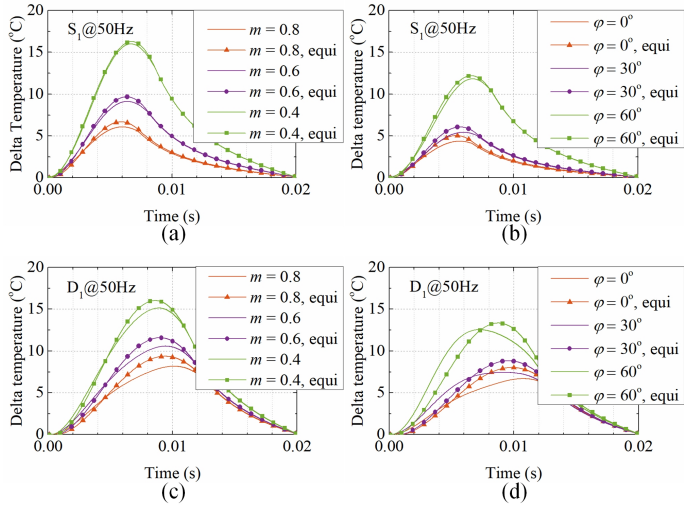


**Fig. 3.8:** Estimated thermal results based on instantaneous power losses and the proposed equivalent power loss curves at 50 Hz: thermal profiles of  $S_1$  (a) under different  $m$ , (b) different  $\varphi$ , thermal profiles of  $D_1$  (c) with various  $m$ , and (d) various  $\varphi$  ( $\varphi = 0^\circ$  for (a) and (c),  $m = 1$  for (b) and (d)) [J1].

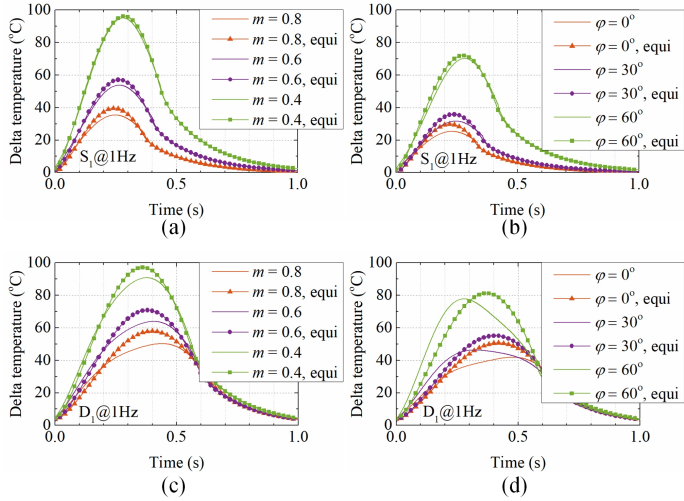


**Fig. 3.9:** Comparison of the thermal results by instantaneous power losses and equivalent power loss curves at 1-Hz operation: the device  $S_1$  (a) under different  $m$ , (b) different  $\varphi$ , thermal profiles of  $D_1$  (c) with various  $m$ , and (d) various  $\varphi$  ( $\varphi = 0^\circ$  for (a) and (c),  $m = 1$  for (b) and (d)) [J1].

is 50 Hz, the estimated results based on the proposed method agree with the theoretical values. The maximum error is around  $2^\circ\text{C}$ . Moreover, considering the low-frequency case of 1 Hz, Fig. 3.9 illustrates the results based on different  $m$  and  $\varphi$ . The



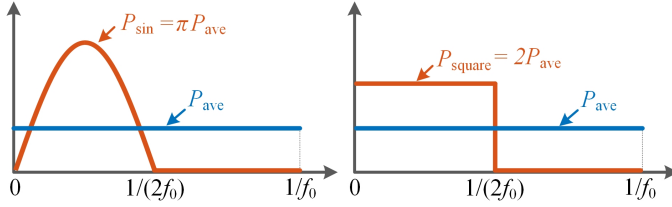


**Fig. 3.10:** Two conventional methods for junction temperature fluctuation estimation: fixed half-sine and fixed square loss profiles [J1].

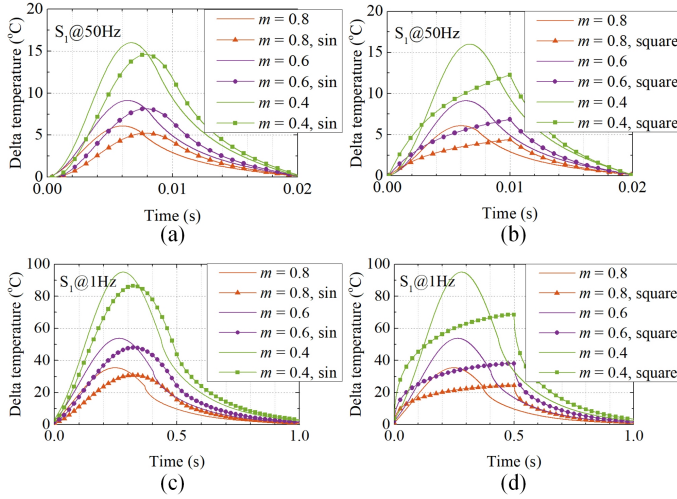


**Fig. 3.11:** Comparison of thermal profiles of  $S_1$  based on two prior-art methods with  $\varphi = 0^\circ$ : (a) fixed half sine loss profile and (b) fixed square loss profile at 50 Hz, (c) fixed half sine loss profile and (d) fixed square loss profile at 1 Hz [J1].

estimated thermal results by the proposed method match with the ones by the instantaneous power losses. Even for the thermal swings at low frequencies (i.e., 1 Hz), the temperature fluctuation of  $S_1$  is as large as  $95^\circ\text{C}$ . The estimated thermal results by the proposed method are close to the results by the instantaneous power losses.

Moreover, two widely utilized power loss profiles for thermal estimation of periodic profiles, i.e., the fixed half-sine and the fixed square loss profiles [46, 47, 66] are shown in Fig. 3.10, which are compared to the proposed method. Notably, These two prior-art methods are developed based on conventional two-level converters. Although both these two methods have the same energy as the instantaneous power losses, the loss duration is fixed to  $1/(2f_0)$ . The DC-bias of the arm current and the induced thermal unbalance are not considered in the two models. The estimated thermal profiles based on the two previous methods are shown in Fig. 3.11. With the fixed square profile, the difference is the largest to around  $25^\circ\text{C}$  at 1 Hz, as shown in Fig. 3.11(d). As shown in Fig. 3.11(a) and Fig. 3.11(c), the differences based on

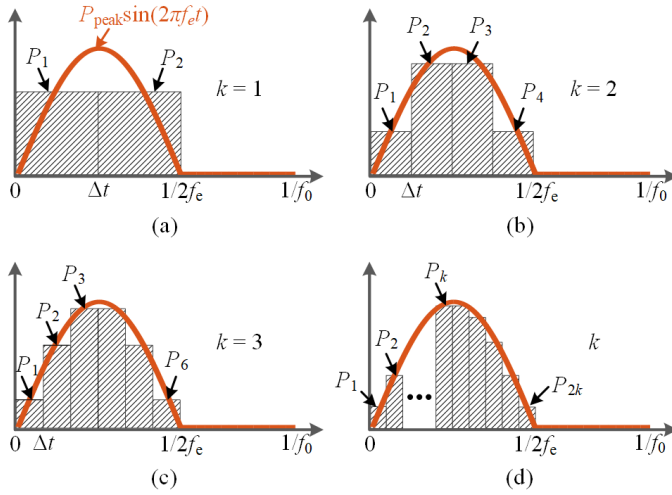


**Fig. 3.12:** The process to divide the equivalent power loss profile into a series of dissipation pulses for thermal estimation, i.e.,  $P_1, P_2, \dots, P_k, \dots, P_{2k}$  and  $k$  is the number of the divided dissipation levels: (a) one-level loss, (b) two-level losses, (c) three-level losses, (d)  $k$ -level losses [J2].

the fixed half-sine loss profile become smaller, but the maximum difference is still approximately  $10^\circ\text{C}$ . Notably, the computational complexity of the fixed half-sine profile is identical to the proposed method. The difference based on the half-sine profile is almost double under the same condition, which emphasizes that both the average power loss and the power loss distribution during a cycle are important for the thermal estimation [J1].

### 3.3.3 Simplification with Quantitative Errors

The aforementioned thermal estimation of the periodic profile needs to divide the equivalent power loss profile into a series of dissipation pulses. As shown in Fig. 3.12, the equivalent power loss profile can be divided into different pulses/levels, e.g., two ( $k = 1$ ), four ( $k = 2$ ), six ( $k = 3$ ), or  $2k$  pulses. With a larger  $k$ , the discretized power loss is more close to the half-sine equivalent power loss profile. A more accurate thermal estimation can be achieved by better power loss approximation but at the cost of increasing computations. This conflict raises a question of how to estimate the thermal behavior with minimum computations while within a maximum allowable error. In order to achieve the target, the error of thermal estimation should be analyzed quantitatively.

As shown in Fig. 3.12, each dissipation pulse can be calculated based on the identical energy, which is expressed as

$$P_i = \frac{4k}{\pi} P_{\text{peak}} \sin \frac{\pi}{4k} \sin \frac{(2i-1)\pi}{4k} \quad (3.8)$$

where  $P_i$  is the amplitude of the  $i$ -th dissipation pulse,  $i = 1, 2, \dots, 2k$ , and  $P_{\text{peak}}$  can be obtained according to (3.6).  $\Delta t$  is the pulse period, which is

$$\Delta t = \frac{1}{4f_e k} \quad (3.9)$$

Substituting (3.8) into the model of (3.7), the maximum temperature is expressed as

$$\Delta T_{\text{max}} = \sum_{i=1}^{k+1} P_i R_{\text{th}} \left(1 - e^{-\Delta t / \tau_{\text{th}}}\right) e^{-(k+1-i)\Delta t / \tau_{\text{th}}} \quad (3.10)$$

Notably, the number of the discretized dissipation pulses relies on the pulse period  $\Delta t$ . Due to the applied thermal model (i.e., Foster model) is usually based on the experimental measurements, the minimum  $\Delta t$  is limited by the minimum time scale of the applied thermal model. Most of the datasheets provide thermal impedances starting from 1 ms, which means that any thermal estimation with  $\Delta t < 1$  ms becomes uncertain. Therefore, the estimation of temperature fluctuation with  $\Delta t = 1$  ms is selected as a base value. The relative error for arbitrary dissipation pulses with  $k$  levels can be calculated as

$$\varepsilon = \frac{\Delta T_{\text{max}}(k_{\text{max}}) - \Delta T_{\text{max}}(k)}{\Delta T_{\text{max}}(k_{\text{max}})} \quad (3.11)$$

which can be expanded as

$$\varepsilon = 1 - \frac{\sum_{i=1}^{k+1} k \sin \frac{(2i-1)\pi}{4k} \sin \frac{\pi}{4k} \left(1 - e^{-\frac{-1}{4kf_e \tau_{\text{th}}}}\right) e^{-\frac{-(k+1-i)}{4kf_e \tau_{\text{th}}}}}{\sum_{i=1}^{k_{\text{max}}+1} k_{\text{max}} \sin \frac{(2i-1)\pi}{4k_{\text{max}}} \sin \frac{\pi}{4k_{\text{max}}} \left(1 - e^{-\frac{-1}{4k_{\text{max}}f_e \tau_{\text{th}}}}\right) e^{-\frac{-(k_{\text{max}}+1-i)}{4k_{\text{max}}f_e \tau_{\text{th}}}}} \quad (3.12)$$

According to (3.12), the obtained relative error only depends on three parameters: the number of loss levels  $k$ , the equivalent frequency  $f_e$ , and the thermal time constant  $\tau_{\text{th}}$  of the selected power device.  $P_{\text{peak}}$  and  $R_{\text{th}}$  do not affect the estimated error. With a specific application,  $f_e$  and  $\tau_{\text{th}}$  are easy to be obtained. The minimum dissipation level  $k_{\text{min}}$  can be calculated with a designer pre-set maximum allowable error  $\varepsilon_{\text{max}}$ .

A 1200-V/50-A IGBT module (i.e., F4-50R12KS4) is selected as the study case. Fig. 3.13 shows the minimum required  $k_{\text{min}}$  with different frequencies and error levels. When the maximum allowable error is selected as 10%, as shown in Fig. 3.13(a),  $k_{\text{max}}$  is around 2,900 while  $k_{\text{min}} = 2$  only when the fundamental frequency is around 0.1 Hz. Moreover,  $k_{\text{min}}$  based on the proposed method does not change significantly with the frequency.  $k_{\text{min}} = 2$  or 1 is enough to achieve a 10% error during the frequency range from 0.1 to 100 Hz. The estimated temperatures are also compared in Fig. 3.13(a). The estimated temperatures using  $k_{\text{min}}$  and  $k_{\text{max}}$  are close to each other under different frequencies. Furthermore, Figs. 3.13(b) and (c) show the results when the maximum allowable error  $\varepsilon_{\text{max}}$  is set as 5% and 1%, respectively. With a smaller error requirement, the estimated temperature has better results, but  $k_{\text{min}}$  based on the proposed method increases accordingly. Notably, the increased  $k_{\text{min}}$  based on the proposed method is still smaller than the  $k_{\text{max}}$  without any simplifications, which allows simplifying computation of thermal estimation even with a higher accuracy requirement.

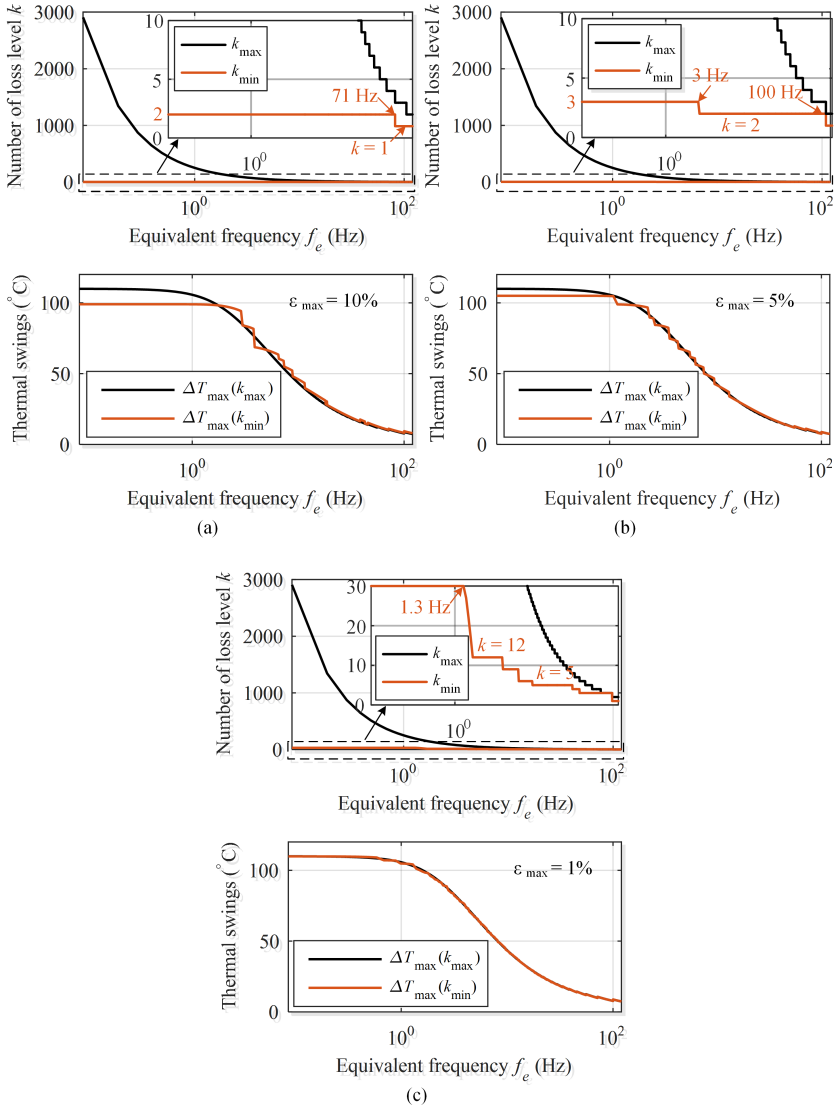


**Fig. 3.13:** Comparison of the required power loss levels of the base ( $\Delta t = 1$  ms) and the proposed method within different maximum allowable errors: (a) the loss levels and corresponding thermal fluctuations when  $\epsilon_{\max} = 10\%$ , (b)  $\epsilon_{\max} = 5\%$ , and (c)  $\epsilon_{\max} = 1\%$  [J3].

### 3.3.4 Experimental Validation

To validate the effectiveness of the proposed method, an experimental platform has been built as shown in Fig. 3.14. The circuit configuration and control strategies of the experimental platform have been discussed in [67] in detail.

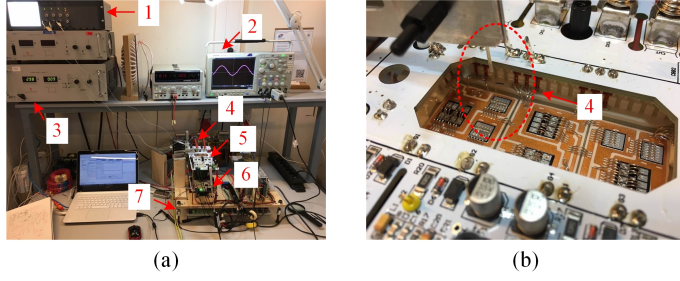


**Fig. 3.14:** Photos of the experimental platform for thermal behavior validation: (a) the set-up and (b) the IGBT module using optical fibers to measure the junction temperature. (1: the receiver of thermal fiber signals, 2: oscilloscope, 3: DC power supply, 4: thermal optical fiber, 5: SM under test, 6: SM for control, and 7: digital controller.) [J1]

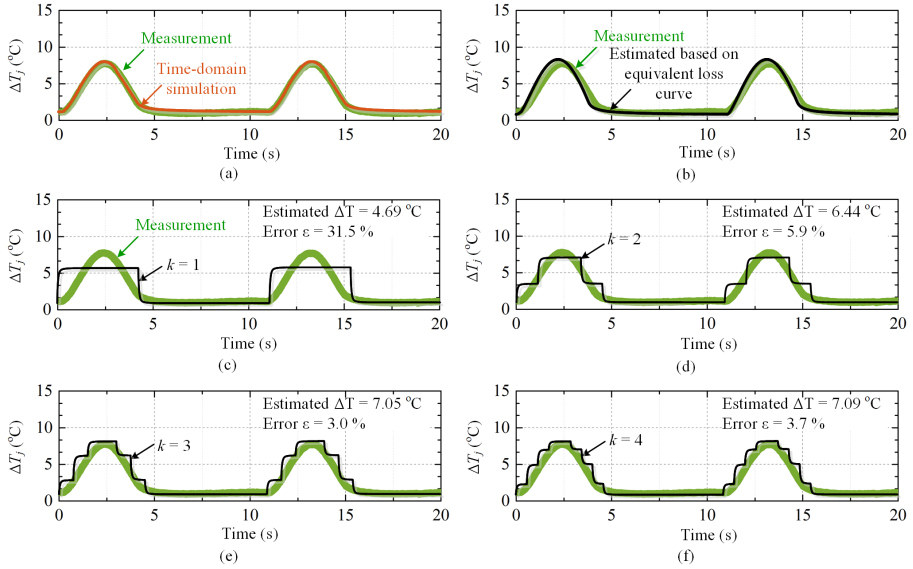


**Fig. 3.15:** Experimental comparison of thermal behaviors of the device  $S_1$  at 0.1 Hz: (a) the measured result and the time-domain simulation, (b) estimated result based on the equivalent power loss profile, (c) estimation based on the proposed simplified method with  $k = 1$ , (d)  $k = 2$ , (e)  $k = 3$  and (f)  $k = 4$ . [J3]

The steady-state junction temperatures of  $S_1$  are measured as shown in Fig. 3.15. The fluctuated waveform of the temperature profile is similar to a half-sine wave. However, the wave is not symmetrical in the period due to the inherent thermal unbalance of the MMC. The measured temperature fluctuation of  $S_1$  is around  $6.84^\circ\text{C}$ , which matches the time-domain simulation result as shown in Fig. 3.15(a). Moreover, the thermal result based on the proposed equivalent power loss profile also agrees with the measurement, as shown in Fig. 3.15(b). Following, Figs. 3.15(c-d) provide

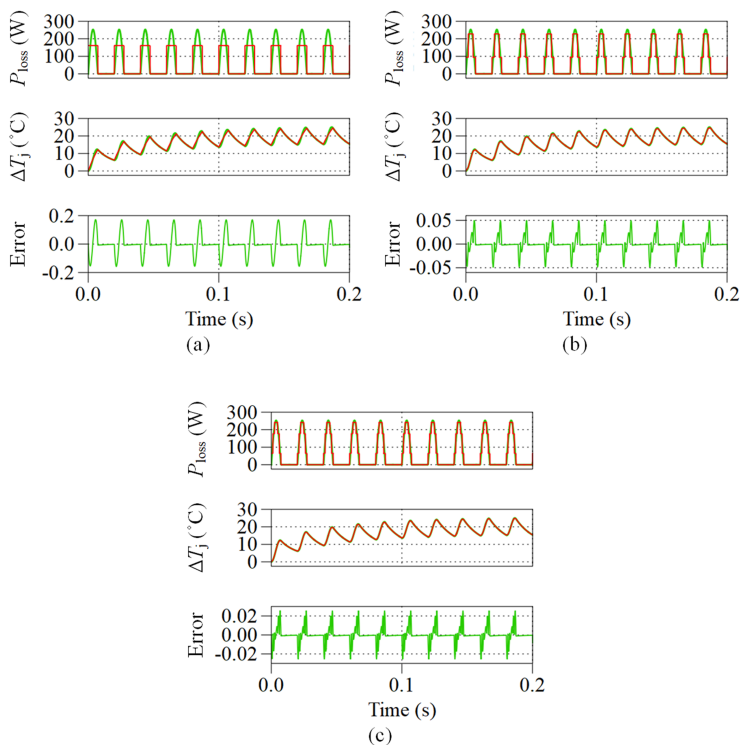


**Fig. 3.16:** Simulation results of power loss profiles, thermal transient behaviors, and the estimated error of the device  $S_1$  at 50 Hz based on the different power loss levels: (a)  $k = 1$ , (b)  $k = 2$ , and (c)  $k = 3$ . [J3]

the simplification based on from  $k = 1$  to  $k = 4$ . Based on the above measurements,  $k = 2$  is the minimum to achieve an  $\epsilon_{\max} = 10\%$ , while  $k = 3$  can provide a 5% error but  $\epsilon_{\max} = 1\%$ . These results are matched with the theoretical analysis in Fig. 3.13.

Furthermore, the 50-Hz thermal behaviors are validated by simulations due to the limited response time of the measuring equipment. In this case, the average power losses are intentionally set as 50 W to obtain a more obvious thermal response. As shown in Fig. 3.16, the estimated thermal behaviors with  $k = 1$ ,  $k = 2$ , and  $k = 3$  can follow the transient thermal response of the equivalent half-sine profile. The case with  $k = 2$  is the minimum requirement to achieve a 10% error. The power loss level with  $k = 3$  provides an error of around 2%. Therefore, the transient results also coincide with the theory as shown in Fig. 3.13

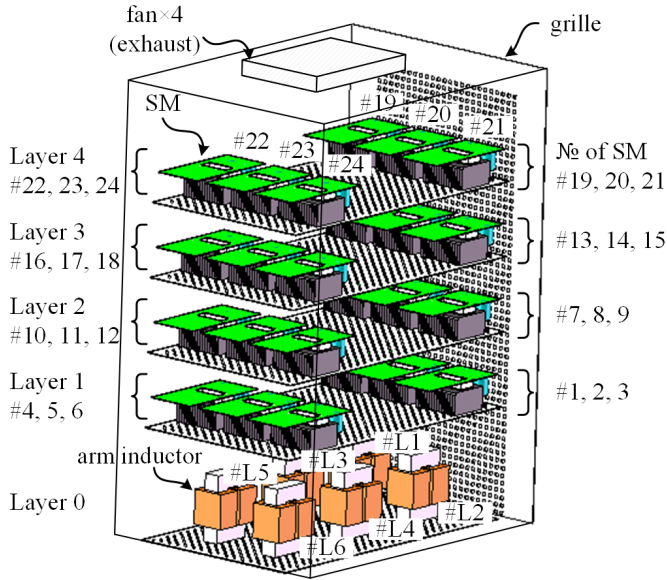


**Fig. 3.17:** 3-D layout of the down-scale MMC, where cooling air is imported from the bottom and backside grilles then exhausted via the top fans [J4].

### 3.4 Non-periodic Power Loss Profiles of MMCs

Non-periodic profiles are due to the variation of loads and environmental conditions. Its time scales are seconds, minutes, or even longer. As discussed above, the Thermal Cross-Coupling (TCC) effects are significant in the non-periodic thermal behaviors. In this part, the non-periodic device thermal profiles are discussed in the down-scale MMC prototype, where its 3-D layout is shown in Fig. 3.17. In this prototype, 24 SMs and six arm inductors are assembled at five different physical layers. The environmental cooling air is imported from the bottom and backside grilles, and then exhausted through the fans on the top of the cabinet. As many components exist in the prototype, a hierarchical thermal model is proposed, as shown in Fig. 3.18. In the first aspect, the junction/hotspot-to-local ambient thermal models of each device are established. The local ambient temperature is the local environmental temperature around a specific SM, in which the TCC effects consider the mutual influences among the different semiconductor chips, capacitors, and bleeding resistors. The second part of the thermal model depicts the relationship between the local ambient temperature of each SM and the global ambient temperature. The global ambient temperature is the temperature outside of the cabinet, which is normally not affected by the operation of the study case. The TCC effects of neighboring SMs and arm inductors are included in the modeling and analysis in the second level modeling.

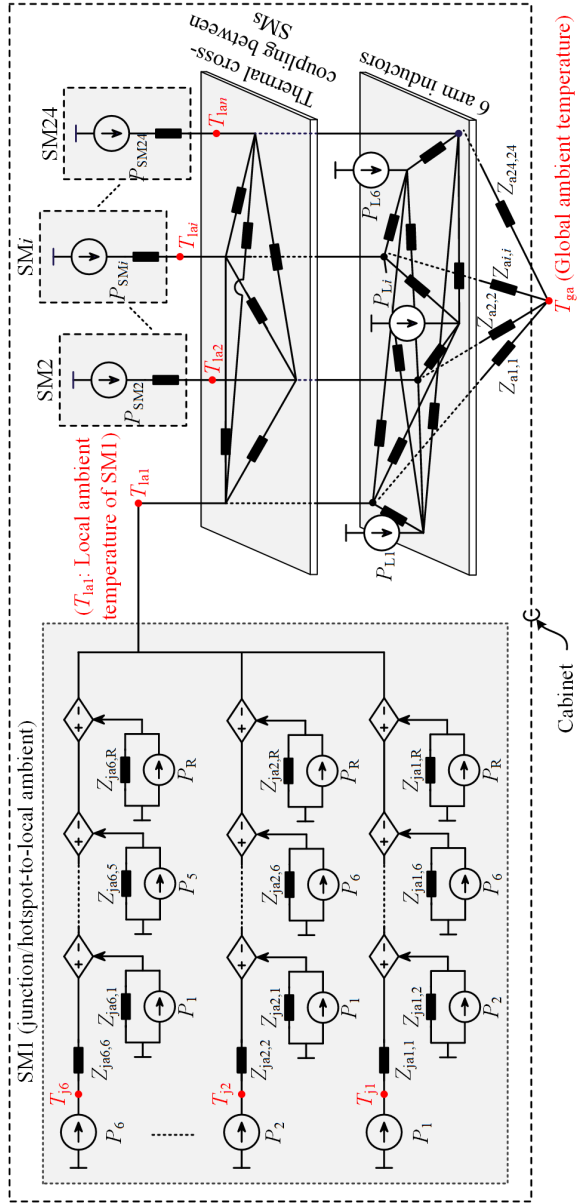


**Fig. 3.18:** Hierarchical decomposition of system-level thermal modeling of the down-scale MMC prototype, which considers the TCC effects among devices and among different subsystems. ( $T_{j1}$ – $T_{j6}$  are junction/hotspot temperatures of power devices or capacitors,  $T_{lai}$  is the local ambient temperature of the  $i$ -th SM,  $T_{ga}$  is the global ambient temperature of the environment,  $P_{SMi}$  is the total power losses of the  $i$ -th SM, and  $P_{Li}$  is the  $i$ -th arm-inductor power losses.) [J4]



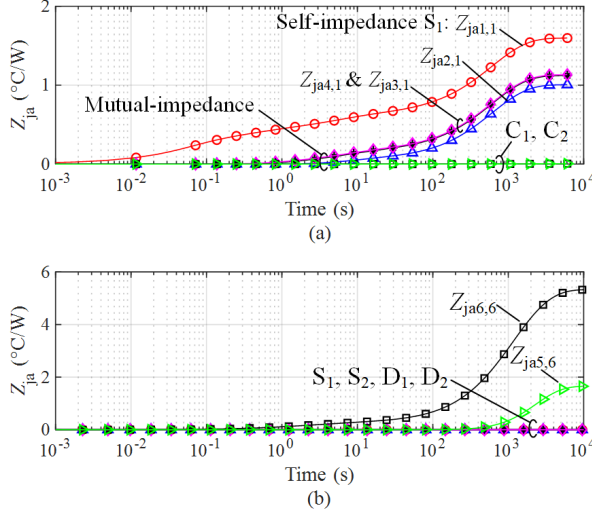


Fig. 3.19: FEM simulation results for the self junction/hotspot-to-local ambient thermal impedances and mutual thermal impedances for the devices in an SM: (a) the active device  $S_1$  and (b) the passive device  $C_2$  [J4].

### 3.4.1 Junction/Hotspot-to-Local Ambient Thermal Modeling

A half-bridge SM is typically comprised of an IGBT module, two capacitors, and a bleeding resistor. According to (3.1), the junction/hotspot-to-local ambient thermal model is expressed as

$$\begin{bmatrix} T_{j1} \\ \vdots \\ T_{j6} \end{bmatrix} = \begin{bmatrix} Z_{ja1,1} & \cdots & Z_{ja1,6} & Z_{ja1,R} \\ \vdots & \ddots & \vdots & \vdots \\ Z_{ja6,1} & \cdots & Z_{ja6,6} & Z_{ja6,R} \end{bmatrix} \begin{bmatrix} P_1 \\ \vdots \\ P_6 \\ P_R \end{bmatrix} + T_{la1}, \quad (3.13)$$

where the subscripts  $\{1, 2, \dots, 6, R\}$  denote the devices  $\{S_1, S_2, D_1, D_2, C_1, C_2, R_b\}$ ,  $T_{j1}, T_{j2}, \dots, T_{j6}$  are the junction or hotspot temperatures,  $Z_{jai,j}$  are the junction/hotspot-to-local ambient thermal impedances,  $P_1, \dots, P_6, P_R$  are the corresponding power losses, and  $T_{la1}$  is the local ambient temperature of SM1. The local ambient temperature is defined as the environmental temperature around the SM.

To obtain the junction/hotspot-to-local ambient thermal impedances, FEM simulations with ANSYS/Icepak are conducted based on real dimensions and material properties, as shown in Fig. 3.19. The self thermal impedance of  $S_1$  (denotes  $Z_{ja1,1}$ ) increase with time. Simultaneously, thermal impedances of  $S_2, D_1,$  and  $D_2$  are rising due to the TCC effects. However, the mutual thermal impedances of both capacitors ( $C_1$  and  $C_2$ ) are almost zero, which means that the temperature variations in the IGBT module do no affect the capacitors. Similarly, the self and mutual thermal impedances

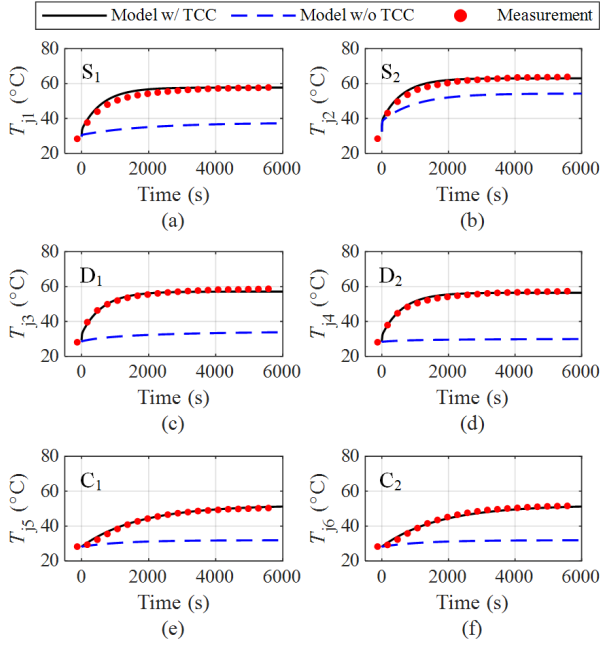


**Fig. 3.20:** Junction/hotspot temperatures of the critical devices in an SM: (a)  $S_1$ , (b)  $S_2$ , (c)  $D_1$ , (d)  $D_2$ , (e)  $C_1$ , and (f)  $C_2$  (where  $T_{\text{lamb}}=28^\circ\text{C}$ , active and reactive power of the MMC are 13.5 kW and 6.5 kVar, respectively. TCC: thermal cross-coupling) [J4].

of the passive component  $C_2$  are shown in Fig. 3.19(b). The capacitors have significant TCC effects between them, but they are independent of the IGBT module in the SM.

The measured junction and hotspot temperatures of an SM are shown in Fig. 3.20. The device  $S_2$  has the maximum junction temperature of  $67^\circ\text{C}$  as a result of the maximum power losses of 16.8 W. Meanwhile, the junction temperature of  $D_2$  is  $51^\circ\text{C}$  while its power losses are only around 1 W. The temperature rise of  $D_2$  is significantly affected the TCC effects of neighboring heat sources. However, without considering the TCC effects, the conventional thermal model provides the estimated thermal results with an error of up to 45%. This underestimated thermal estimation verifies that the TCC effect is non-negligible in the thermal estimation of the device.

### 3.4.2 Local Ambient-to-Global Ambient Thermal Modeling

As mentioned in (3.13), the local ambient temperature for each SM  $T_{\text{lai}}$  is the reference to estimate the junction/hotspot temperature of devices. The accuracy of the local ambient temperature affects the accuracy of the estimated device temperatures. The conventional thermal models usually assume the local ambient temperature as identical to the global ambient temperature. However, for the MMC with many SMs, the local ambient temperature of an SM is inevitably affected by the temperature rises

of the neighboring subsystems, as shown in Fig. 3.18. Thus, the SM and arm inductors are regarded as a unit. A thermal matrix method is applied again to consider the system-level TCC effects, which is expressed as

$$\begin{aligned}
 & \begin{bmatrix} T_{1a1} \\ T_{1a2} \\ \vdots \\ T_{1a24} \end{bmatrix} = \\
 & \begin{bmatrix} Z_{a1,1} & \cdots & Z_{a1,24} & \cdots & Z_{a1,L6} \\ Z_{a2,1} & \cdots & Z_{a2,24} & \cdots & Z_{a2,L6} \\ \vdots & \ddots & \vdots & \ddots & \ddots \\ Z_{a24,1} & \cdots & Z_{a24,24} & \cdots & Z_{a24,L6} \end{bmatrix} \begin{bmatrix} P_{SM1} \\ \vdots \\ P_{SM24} \\ P_{L1} \\ \vdots \\ P_{L6} \end{bmatrix} + T_{ga} \quad (3.14) \\
 & \Rightarrow \mathbf{T}_{1a} = \mathbf{Z}_a \mathbf{P}_{SM/L} + T_{ga}
 \end{aligned}$$

where  $\mathbf{T}_{1a}$  is the local ambient temperature vector of each SM. The local ambient-to-global ambient thermal impedance  $\mathbf{Z}_a$  characterizes the TCC effects between SMs and the impact of the cabinet and inductors.

In this case, the local ambient-to-global ambient thermal impedances are also characterized by FEM simulations. Each SM is heated up separately, and the local ambient temperature of each SM is recorded. Then, the obtained transient thermal impedances are shown in Fig. 3.21. When SM1 on the backside of the cabinet is heated up, the rising of self-thermal impedance  $Z_{a1,1}$  indicates that the local ambient temperature of SM1 increases as shown in Fig. 3.21(a). Meanwhile, the local ambient temperatures of the SMs (i.e., SM7, SM8, SM13, SM14 and SM19) are also heated up, which are described as the rising curves of  $Z_{a7,1}$ ,  $Z_{a8,1}$ ,  $Z_{a13,1}$ ,  $Z_{a14,1}$  and  $Z_{a19,1}$ . Since the cooling air is imported from the bottom and backside grilles and exhausts via the top of the cabinet, the TCC effects between SMs propagate mainly through the upward direction. Similarly, the front-side SM4 is heated up, as shown in Fig. 3.21(b). Compared to the SM1 in the same layer of the cabinet, the TCC effects of SM4 are more noticeable. This is because the front cabinet is airtight glass while the backside is grille with cooling air imported. Thus, the properties of the cabinet also have a significant impact on the local ambient-to-global ambient thermal impedances. In summary, the local ambient temperatures of SMs are significantly affected by the layout, the cooling method, and the material properties of the cabinet.

To identify the local ambient temperature distribution of the cabinet, measurement is carried out on each SM using K-type thermocouples and a data logger NI-9213. The local ambient temperatures of the 24 SMs are monitored continuously, as shown in Fig. 3.22. When the MMC system is not running (Time = 0 s), all the local ambient temperatures are equal to the global ambient temperature of 28°C. Afterwards, the local ambient temperatures of the SMs increase with an obvious divergent with the system operating. The divergence between different SMs is up to 17°C. Moreover, even though SM6 has the lowest local ambient temperature,  $T_{1a6} = 41^\circ\text{C}$ , it is still obviously higher than the global ambient temperature. Thus, without consideration

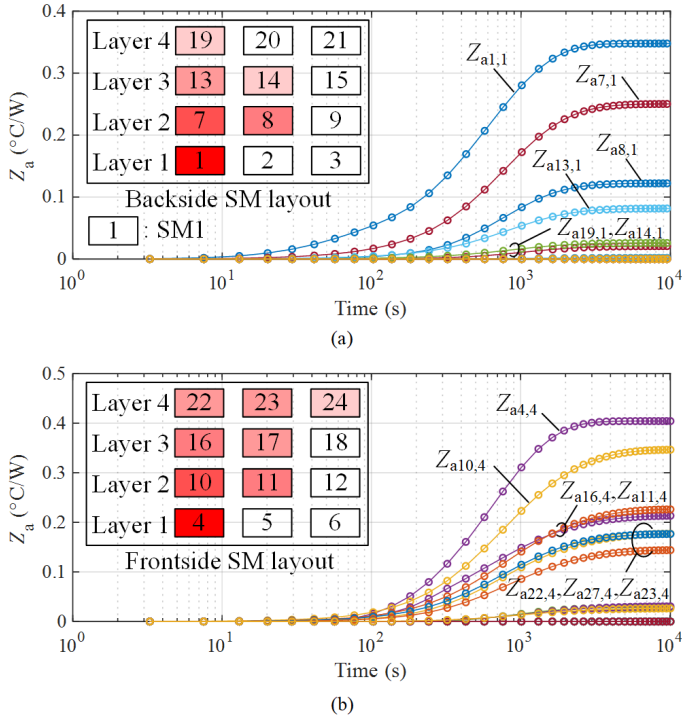


**Fig. 3.21:** The local ambient-to-global ambient thermal impedances with single SM heated-up respectively: (a) SM1 is heated up only and (b) SM4 is heated up only [J4].

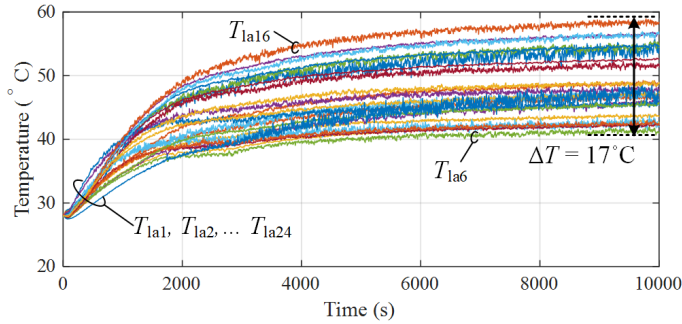


**Fig. 3.22:** Measured local ambient temperatures of 24 SMs in the MMC platform, where active and reactive powers are 13.5 kW and 6.5 kVar, and the global ambient temperature is  $28^\circ\text{C}$  [J4].

of the difference between the local ambient temperature and the global ambient temperature, the estimated device stresses will be underestimated. Furthermore, Fig. 3.23 compares the measured local ambient temperatures with the estimated values. The estimated results agree with the experimental data, with a maximum error of 2.5%.

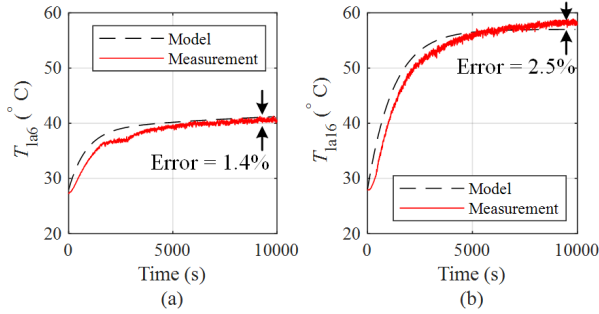


**Fig. 3.23:** Comparison of the measured local ambient temperatures and the estimated results of two SMs: (a) SM6 and (b) SM16 (the conditions are the same as Fig. 3.22) [J4].

## 3.5 Thermal Interface Materials in SMs

In the thermal modeling of power semiconductor devices, TIM has a substantial contribution to the thermal resistance from the junction to heatsink. However, conventional reliability predictions are usually assuming it as a constant. Therefore, this section has two parts: 1) investigate the impact of the applied TIM on the predicted lifetime, and 2) proposes a simple solution to characterize the thermal resistance of the TIM under realistic conditions.

### 3.5.1 Impact of TIM Thicknesses on Predicted Lifetime

Thermal models serve to convert power losses into temperatures of devices (e.g., IGBT module), as shown in Fig. 3.24. In many power electronic systems, a specific TIM is required to be assembled between the IGBT module and the heatsink. Thus, the thermal resistance of the TIM affects the junction temperature of the power device. In practice, the TIM is typically not a solid, which leads to the varied thermal resistance of the applied TIM. As shown in Fig. 3.25, the thermal resistance of the TIM is linear to the increasing Bond-Line Thickness (BLT) with a specific starting assembly thickness. Simultaneously, the thermal resistance is also related to different starting thicknesses. These thermal resistance data comes from [68], which are measured based on standard ASTM D5470 [51].

Furthermore, when applied thermal resistance of the TIM to lifetime prediction, the estimated annual thermal profiles and lifetime are shown in Figs. 3.26 and 3.27, respectively. With a starting thickness of 0.150 mm, the junction temperature of  $S_2$  peaks from approximately 105 °C (BLT = 0.02 mm) to 121 °C (BLT = 0.06 mm). Moreover, the predicted lifetime is also inappropriate to the starting thickness from 0.200 mm to 0.150 mm, as shown in Fig. 3.27. These phenomena emphasize the significant influence of the BLT and the starting thickness on both the junction temperatures and lifetime prediction.

Following, an experiment is carried out to measure the junction temperature profiles under various TIM thicknesses. The starting thickness of the TIM is controlled

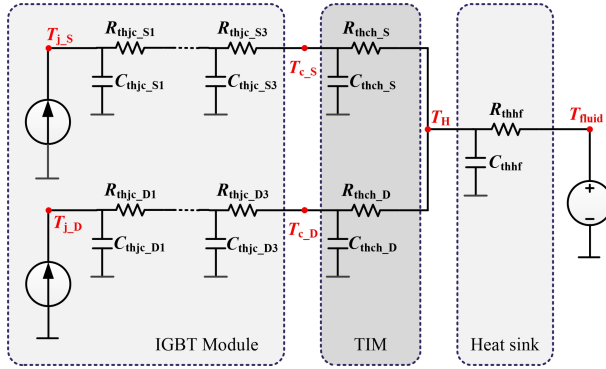


**Fig. 3.24:** Thermal model for a typical IGBT module which is assembled with TIM and a heatsink [C3].

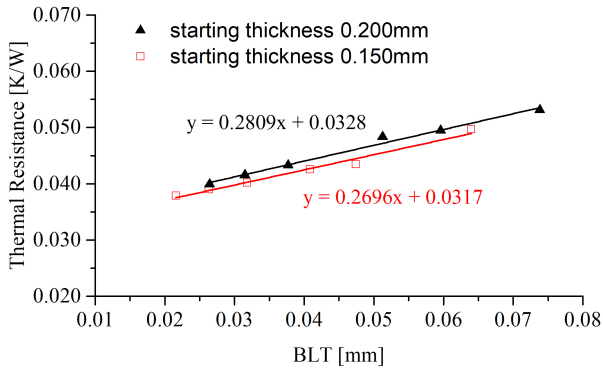


**Fig. 3.25:** Manufacturer provided thermal resistance of the TIM varies with the starting assembly thickness and the Bond-Line Thickness (BLT), data from [68] [C3].

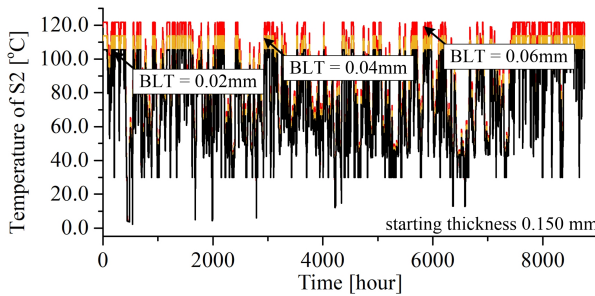


**Fig. 3.26:** Estimated thermal profiles of the device  $S_2$  under various BLTs of the TIM (the starting thickness is 0.150mm) [C3].

by a steel stencil with thicknesses from 80 to 200  $\mu\text{m}$ , as shown in Fig. 3.28. The IGBT

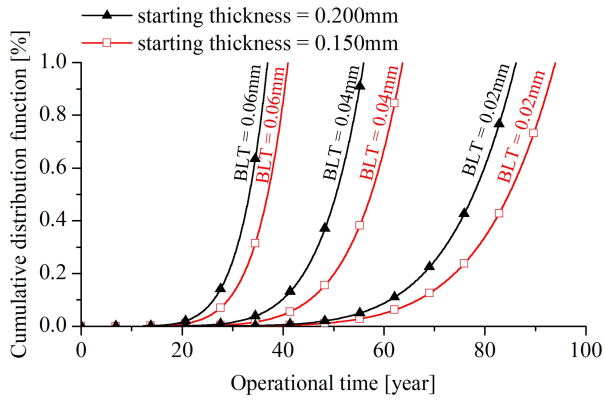


Fig. 3.27: Accumulated Damage of  $S_2$  under various BLT and starting assembly thicknesses [C3].

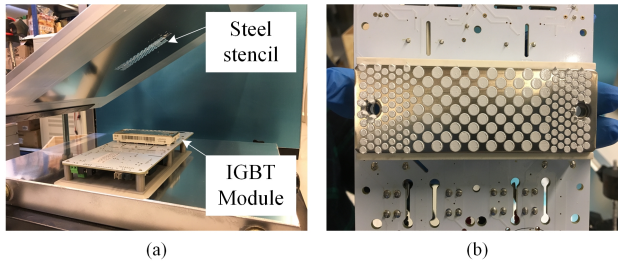


Fig. 3.28: The equipment to apply TIMs with screen printing, where the starting thickness of the TIM is controlled by the stencil: (a) screen printing equipment and (b) the applied TIM on the surface of the IGBT base plate [C3].

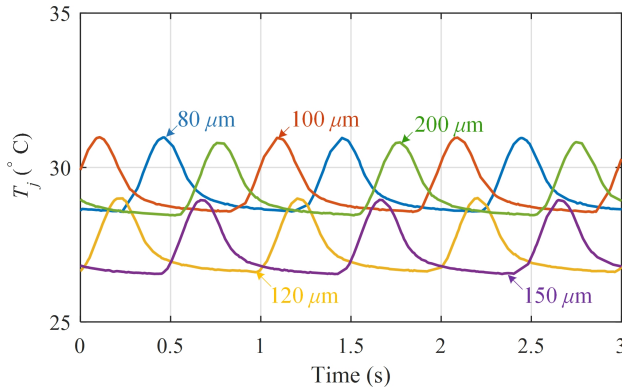


Fig. 3.29: Measured junction temperatures of the power device  $S_1$  in an SM of the MMC system with different starting thicknesses (the screw torque is fixed to 2 N·m) [C3].

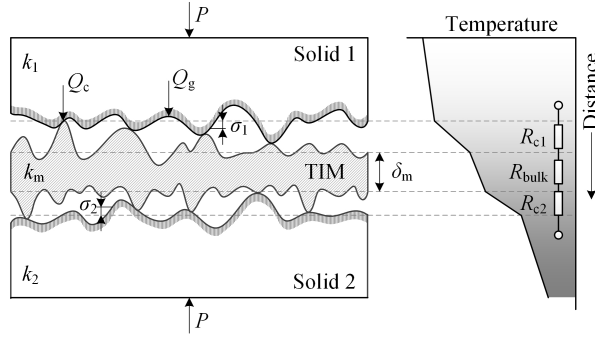


Fig. 3.30: A typical schematic assembly of the real joint surface of the TIM.

module is then applied to the same screw torque, which is aimed to keep the identical applied pressure. The measured junction temperatures of the device  $S_1$  are shown in Fig. 3.29. With a starting thickness of  $80\ \mu\text{m}$ , the junction temperature peaks approximately at  $31\ ^\circ\text{C}$ . Meanwhile, the starting thickness of  $100\ \mu\text{m}$  still has a maximum junction temperature of  $31\ ^\circ\text{C}$ . Furthermore, the maximum junction temperature decreases to  $28\ ^\circ\text{C}$  with the starting thicknesses of  $120\ \mu\text{m}$  and  $150\ \mu\text{m}$ . With a further increase of the starting thickness to  $200\ \mu\text{m}$ , the maximum junction temperature increases again to  $31\ ^\circ\text{C}$ . These results uncover the significant effect of the TIM on the junction temperature of the power device. However, the thermal resistance of TIM under realistic conditions is not linear as the standard condition. Either too thin or too thick thickness of the TIM increases the junction temperatures and impair the lifetime of power devices.

### 3.5.2 An Empirical Characterization Model for TIMs under Realistic Conditions

The aforementioned experimental results reveal that the thermal resistance under realistic conditions might be different from the standard linear result. Thus, how to model the thermal resistance with consideration of the realistic conditions is necessary. In the following part, a proposed empirical model of TIMs is discussed under realistic conditions.

A typical assembly joint of a TIM with two rough solids (e.g., based plates of IGBT modules, heatsinks, etc) is shown in Fig. 3.30. In the steady state, heat transfer across the joint has two contact resistances  $R_{c1}$  and  $R_{c2}$  and a bulk resistance of the TIM  $R_{\text{bulk}}$ , which are described as

$$R = R_{c1} + R_{\text{bulk}} + R_{c2} \quad (3.15)$$

In ASTM D5470 standard, the TIM is measured under an idealized flat surface, which means that the contact resistances are near to zero. However, due to milled heatsinks and pre-bended IGBT modules are commonly utilized in power electronic system, the contact resistance may have a significant effect.



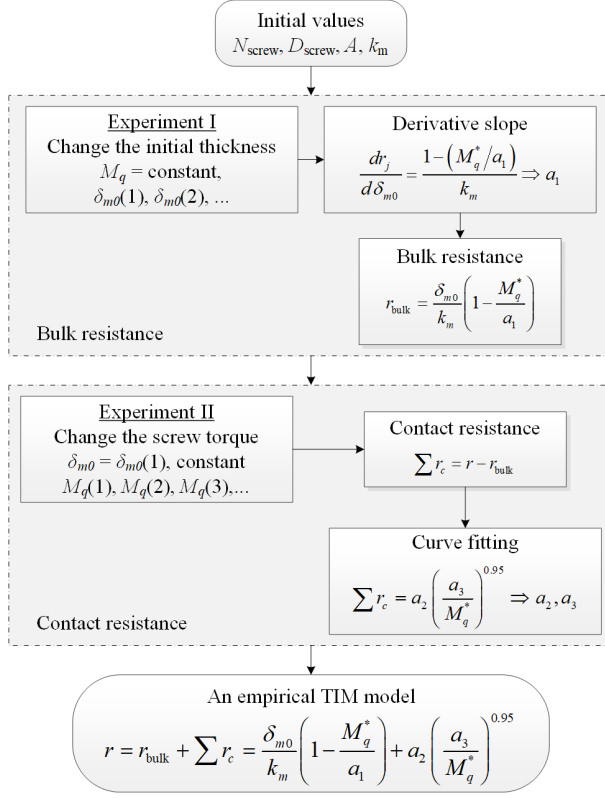


**Fig. 3.31:** The proposed method to characterize the thermal resistance of TIM considering realistic conditions [J5].

According to [54], the specific contact resistance of the TIM can be presented as

$$r_{c,i} = \frac{0.8\sigma(i)}{m(i)k_s(i)} \left( \frac{H_c}{P} \right)^{0.95} \quad (3.16)$$

where  $\sigma(i)$  is the effective surface roughness,  $m(i)$  is the absolute asperity slope,  $k_s(i)$  is the mean thermal conductivity between two surfaces,  $i = 1, 2$  represents the contacting solids,  $P$  is the apparent contact pressure, and  $H_c$  is the hardness of TIMs. Notably, the specific contact thermal resistance is defined as  $r_c = R_c/A_a$ .  $A_a$  is the apparent contact area.

The specific bulk resistance is expressed as, according to [54]

$$r_{\text{bulk}} = \frac{\delta_{m0}}{k_m} \left( 1 - \frac{P}{E_m} \right) \quad (3.17)$$

where  $\delta_{m0}$  is the starting assemble thickness with pressure of zero, and  $E_m$  is the effective Young's modulus.

Based on the above physical model, a method to characterize the thermal resistance of the TIM is shown in Fig. 3.31. First, the initial thickness of  $\delta_{m0}$  only affects

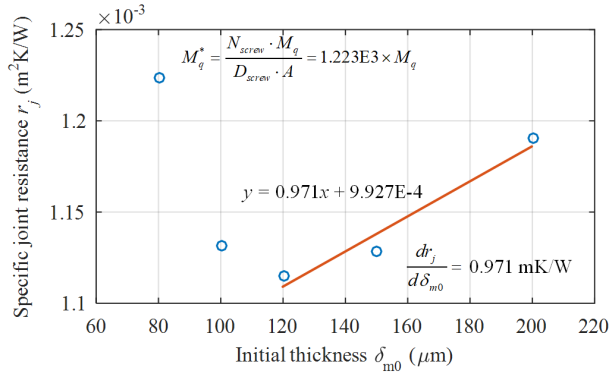


**Fig. 3.32:** Specific joint thermal resistance under five different initial thicknesses of the TIM (the screw torque is 2 N·m). The first two data do not obey the linear rule of the bulk resistance since the initial thickness is too thin. The air gap between two solids are not fully filled [J5].

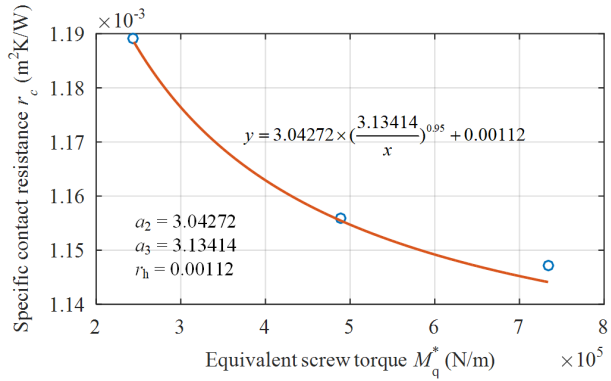


**Fig. 3.33:** Specific joint thermal resistance under three different screw torques and a constant initial thickness of the TIM [J5].

the bulk resistance. With a constant screw torque, the parameter  $a_1$  related to the bulk resistance can be obtained by changing the different initial thickness. Next, with the constant initial thickness, the contact resistance is characterized by changing the screw torques.

To validate the proposed method, the platform shown in Fig. 3.28 is used again. Five different initial thicknesses (i.e., 80, 100, 120, 150 and 200  $\mu\text{m}$ ) and two screw torques (i.e., 2, 4, 6 Nm) are applied. The measured thermal resistances are shown in

Figs. 3.32 and 3.33. Then, the TIM is characterized as

$$r_{\text{TIM}} = \frac{\delta_{m0}}{k_m} \left( 1 - \frac{M_q^*}{a_1} \right) + a_2 \times \left( \frac{a_3}{M_q^*} \right)^{0.95}$$

$$a_1 = 6.999\text{E}5$$

$$a_2 = 3.043$$

$$a_3 = 3.134$$
(3.18)

The empirical model is relied on a few number of measurements under realistic conditions. All the input are related to starting thicknesses and screw torques, which are easy to be applied and obtained in power converter designs.

However, the limitations of the proposed method include: 1) the thermal grease is only considered and evaluated. Different TIM materials or types (e.g., film) might have different characteristics and models; 2) the proposed empirical model do not have any physical meaning, which means that the model is highly related to the selected power devices and heatsinks.

### 3.6 Summary

In this chapter, multi-time scale thermal profiles in power electronic systems are classified into periodic and non-periodic profiles. The frequency-domain analysis has pointed out that the non-periodic profiles require to consider self- and mutual-thermal impedances, while periodic profiles require self thermal impedances only.

To model the inherent thermal unbalance of the MMC caused by the DC-bias current, an equivalent power loss profile is proposed for the periodic profiles. Moreover, based on the proposed equivalent power loss profile, a quantitative error model is established to simplify the computation while within a maximum allowable error. Experiments have been provided to verify the effectiveness of the proposed method in terms of different frequencies, steady states, and dynamics.

A system-level thermal model is proposed to consider the non-periodic profiles through two parts: the junction/hotspot-to-local ambient thermal model and the local ambient-to-global ambient thermal model. The first part considers the TCC effects among different devices (e.g., IGBTs, capacitors, etc.). The measurements show the TCC effects significantly affect the thermal estimation, an error of 45% is observed based on the conventional thermal models without considering the TCC effects. Subsequently, the second part of the thermal model provides a more accurate temperature reference for each SM. An in-situ measurement has revealed that not only the local ambient temperatures are different from the global ambient temperature up to 30°C, but also the local ambient temperatures between SMs are divergent to each other (up to 17°C). Even though the same type of components are utilized in each SM and the power losses between SMs are homogeneous, the divergent thermal results reveal the complicated thermal behaviors in the MMC. Beyond the reliability evaluation, the proposed thermal model also provides a guideline for the physical layout of SMs.

Finally, TIM is investigated from two aspects. First, the impact of TIM thicknesses on the predicted lifetime. The results have pointed out that both initial thickness and

BLT affects the predicted lifetime significantly. Second, an empirical characterization model is proposed for TIMs under realistic conditions. The proposed model relies on a few numbers of measurements. All the inputs are related to the initial thicknesses and screw torques only, which are easy to be applied in the power converter design.

## Chapter 4

# Mission Profile-based Lifetime Prediction for MMCs

### 4.1 Abstract

Based on the aforementioned power loss and thermal models, this chapter discusses a mission profile-based lifetime prediction method for an MMC system. Typically, the lifetime prediction of the MMC is deployed from bottom to top, e.g., from the component level, subsystem level, and up to the entire system evaluation. In prior-art studies, a few works have discussed the lifetime prediction of IGBT modules in MMCs based on long-term mission profiles [22]. However, the justifications of using the specific mission profiles or lifetime models have few discussions. Moreover, when it comes to system-level reliability of MMCs, the state-of-the-art studies are mostly based on constant failure rate models [17–19]. The constant failure rates are collected from large-population products of random failures, which are limited for MMCs with a small amount of commissioned projects and insufficient long-term usage data. Therefore, based on an offshore wind power application using an MMC, this chapter investigates the following three aspects:

- The impact of mission profiles on predicted component lifetime;
- The impact of lifetime model selections on assessed component lifetime;
- System-level reliability evaluation of a complete MMC system.

### 4.2 The Impact of Mission Profiles

Mission profile based lifetime prediction is an application-dependent reliability analysis method. In a wind power application using an MMC system, the mission

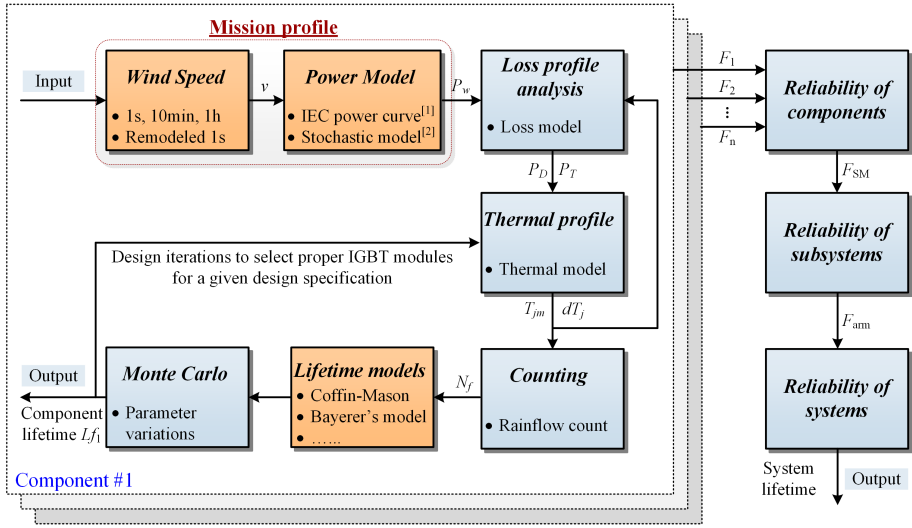


**Fig. 4.1:** Mission profile-based lifetime prediction method for the entire system of an MMC system.

profile data is converted into power information (e.g., active and/or reactive power), component-level power loss profiles, thermal profiles, and finally to predict the lifetime consumption of components due to wear-out failures. However, the requirements of the specific mission profile data have rarely been discussed in lifetime prediction. Reference [22] adopts the mission profile with a resolution of 1 hour/data in the lifetime prediction of the MMC system, but the reason or impact of the specific resolution still remains unclear. The higher resolution of mission profiles contains more rich information in terms of dynamic. As a result, a more accurate lifetime prediction could be anticipated, but at the cost of high-resolution data measurements, information storage, and more computational resources for the analysis. By contrast, mission profiles with a low resolution sacrifice the accuracy of lifetime prediction but benefit from alleviated sampling and computation. Regarding the lifetime prediction, the impact of different mission-profile resolutions is still unclear. Thus, the different mission profile selections are investigated in the following part.

#### 4.2.1 Different Mission Profile Resolutions based on a Wind Power Application

To investigate how the different mission profile resolution to affect the predicted lifetime of the MMC, the wind speed data was collected from an offshore platform in North Sea, as shown in Fig. 4.2. The period of the data ranges from September 2015 to August 2016 with a time resolution of 1 s/data. An average algorithm is conducted to obtain the corresponding data with resolutions of 10 minute/data and 1 hour/data. Notably, 1-s/data profiles usually require large data storage and thus are limited in field situations. Conversely, 10-minute/data wind speeds are commonly utilized in

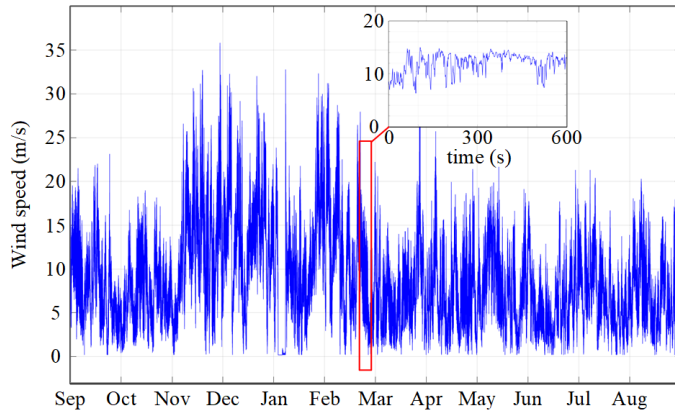


Fig. 4.2: Annual wind speeds with a resolution of 1 s/data from an offshore platform [C1].

many standard SCADA systems. However, 10-minute/data wind speeds inevitably sacrifice the fluctuations during the time scale of 10 minutes, as shown in the zoom-in box of Fig. 4.2. Ignoring these fluctuations might lead to an over optimistic lifetime. Therefore, apart from the originally measured 1-s/data, 10-minute/data and 1-hour/data mission profiles, a remodeled 1-s/data profiles are also involved in the study. The remodeled 1-s/data profiles is regenerated from 10-minute/data profile based on the proposed method in [69].

Apart from the wind profile, a power conversion model is also mandatory to translate wind speeds into power information, as shown in Fig. 4.1. The IEC power curve [70] is one of the widely accepted methods, which is originally developed from wind turbines. However, the IEC power curve only reveals the steady-state relationship between wind speeds and output power. When this model is utilized into a wind farm or conversion of high-resolution wind speeds, the steady-state model may lead to some errors since the IEC power curve is difficult to model the dynamics. Alternatively, a stochastic model [69] is proposed to convert the high-resolution wind speeds (i.e., 1 s/data) into output power of a wind farm. The field data have validated this model. Notably, when the wind speeds have a longer time scale, e.g., 10 minute/data or 1 hour/data, the dynamic effects of the wind farm are not significant. The output power of a wind farm is usually based on the IEC power curve directly [70].

Therefore, as listed in Table 4.1, five different mission profile resolutions are composed of four different wind-speed profiles and two power conversion models. The 1-s/data wind speeds and the stochastic model are selected as the benchmark, since it has the highest resolution and the power conversion model has been verified by a real wind farm in [69]. The predicted lifetime results by the other four different mission profiles are compared to the benchmark. The comparative investigation is aimed to uncover the impact of mission profiles.

**Table 4.1:** The Studied Five Different Mission Profiles [C1]

No.	Mission Profiles	Wind Resolution	Power Conversion Model
1	STO1s (Benchmark)	1 s/data	Stochastic model [69]
2	IEC1s	1 s/data	IEC power curve [70]
3	IEC10min	10 minute/data	IEC power curve
4	IEC1h	1 hour/data	IEC power curve
5	STO1sREG	remodeled 1 s/data	Stochastic model

## 4.2.2 Impact of Mission Profile Resolutions on Predicted Lifetime

According to the flowchart of component-level reliability prediction as shown in Fig. 4.1, the lifetime consumptions of IGBTs ( $S_1$  and  $S_2$ ) and its free-wheeling diodes ( $D_1$  and  $D_2$ ) are shown in Fig. 4.3. The three major dominant failure locations, i.e., the chip solder, baseplate solder, and bond wire, are denoted as CS, BS, and BW, respectively. The consumed lifetime due to 1-s/data wind speeds and the stochastic model is benchmarked. Compared to the results of 1-s/data profiles and the IEC power curve (labeled as IEC1s), the overestimated lifetime consumptions reveal that the IEC power curve induces excessive fluctuations with the high-resolution wind speeds. This power conversion model calculates many illusive fatigues. The IEC power curve is developed from the steady-state output power of wind turbines, where the time scale of 1 s is commonly less than the time constant of the wind turbines and/or farms. Therefore, the IEC power curve with 1-s/data wind speeds may provide a misleading predicted lifetime.

On the contrary, as shown in Fig. 4.3, the predicted lifetime consumption with 10-minute/data and 1-hour/data wind speeds and the IEC power curve is underestimated. This is because the mission profiles at the time scale of 10-minute or 1-hour cannot involve a large number of temperature fluctuations within the time scale of several seconds in-field operation, which leads to the ignorance the device degradation under the time scale. Therefore, mission profiles based on 10 minute/data or 1 hour/data may result in an over-optimistic reliability estimation.

When it comes to the remodeled 1 s/data wind speeds and the stochastic model (labeled as STO1sREG), the predicted lifetime consumption is close to the benchmark (labeled as STO1s). It reveals that the dynamics at 1 s can also be modeled by the regenerated model. When the wind speed profiles at 1 s/data are not accessible in practice, the regenerated high-resolution wind speeds are an alternative solution.

In summary, when applying the IEC power curve to convert the 1-s/data wind speed mission profiles, the calculated abundant high-frequency temperature swings do not exist in practice and thus lead to an overestimated lifetime consumption. By contrast, 10-minute/data or 1-hour/data wind speeds and the IEC power curve are challenging to model the temperature fluctuations at the time scale of seconds, which might lead to an over-optimistic lifetime result. In addition, when 1-s/data wind speeds are not accessible in practice, the remodeled 1-s/data wind speeds from standard SCADA 10-minute/data profiles are an alternative solution.



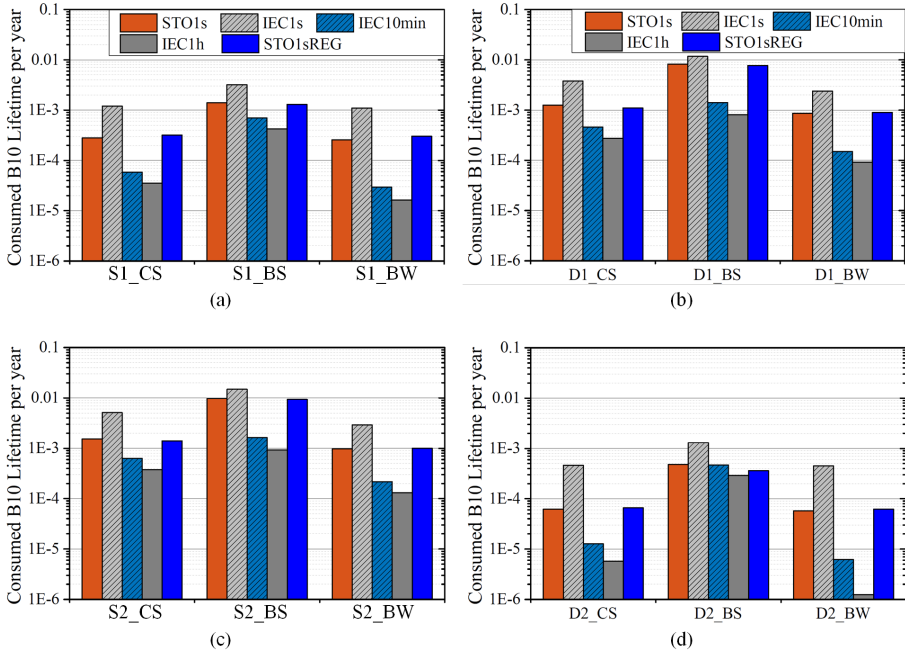


**Fig. 4.3:** The consumed  $B_{10}$  lifetime per year due to wear outs of power devices (i.e.,  $S_1$ ,  $S_2$ ,  $D_1$ , and  $D_2$ ) in an SM of the MMC given different mission profile resolutions (see Table 4.1), where CS, BS and BW represent the chip solder, baseplate solder, and bond wire, respectively. (a)  $S_1$ , (b)  $D_1$ , (c)  $S_2$ , (d)  $D_2$ . [C1]

## 4.3 Impact of Lifetime Model Selection

As shown in Fig. 4.4, a typical IGBT module consists of different layers, where these layer materials have different expansion coefficients. When an IGBT module is exposed to temperature fluctuations, the thermo-mechanical stress between materials leads to the aging process of the connections, which eventually causes device failure. Therefore, many lifetime models of power modules (i.e., the number of temperature cycles) are developed as a function of the temperature swings (i.e.,  $\Delta T$ ). In this investigation, annual wind speeds with a resolution of 1-hour/data are utilized. The following part is going to discuss the impact of different lifetime model selections.

### 4.3.1 Typical Lifetime Models

As listed in Table 4.2, many lifetime models have been proposed to quantify the relationship between the number of cycles to failure and the applied stresses. Model 1 is the well-known Coffin-Manson model [55]. The number of cycles to failure  $N_f$  is related to the temperature change  $\Delta T$ . The model coefficients  $A$  and  $n$  are empirical parameters that are dependent on the power cycling data. In reference [56], the

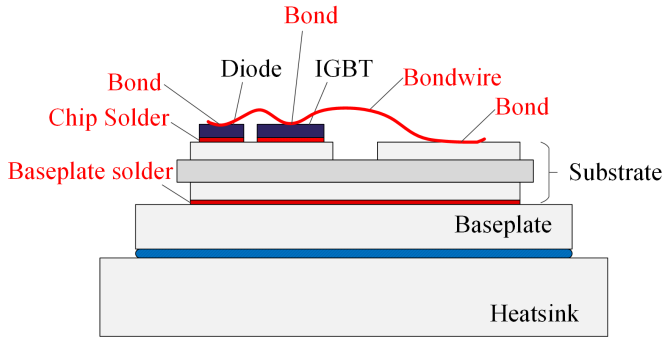


Fig. 4.4: Physical structure of a typical IGBT module

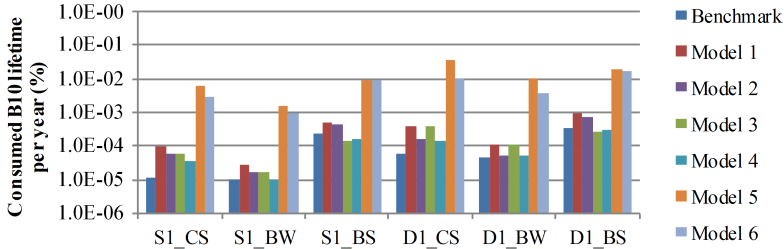
effect of the temperature swings is explained by a stress-strain model. With a low stress below the yield strain ( $\Delta T$  is small), the produced energy only results in elastic deformation. Thus, no damage occurs in the situation. On the contrary, when the stress is above the yield strain, an irreversible deformation is induced and the material enters into the plastic region. Thus, the parameter  $\Delta T_0$  in Model 2 represents the elastic strain range, which depends on different materials and packaging technology. If  $\Delta T_0$  is negligible, it can be removed from Model 2 and the equation turns to be the Coffin-Manson model expressed in Model 1. Moreover, the LESIT project [71] in the 1990s reveals the influence of the average junction temperature  $T_m$  on the number of cycles. As a result, the Coffin-Manson model is modified via the Arrhenius approach as Model 3, where  $k_B$  is Boltzmann's constant, and  $E_a$  is the activation energy. Similarly, considering the elastic strain range, Model 3 can be rewritten as Model 4. As the next step, the  $N_f$ -lifetime dependency was examined by other parameters, such as power-on time  $t_{on}$ , the current per wire bond  $I$ , the diameter of bond wires  $D$ , the chip voltage class  $V$ , etc. One of the most representative ones is Bayerer's model as shown in Model 5 [58]. The corresponding Model 6 consider the elastic strain range. It worth noticing that each lifetime model has its limitations and effective ranges. It thus raises a question of how to select a lifetime model in the reliability assessment and the corresponding effects. In order to investigate the impact of different lifetime model selections, power cycling data from the manufacturer [72] is chosen as the benchmark in the study. Based on an MMC system, the predicted lifetime results according to the different lifetime models listed in Table 4.2 are compared.

### 4.3.2 Impact of Lifetime Model Selections on Predicted Lifetime

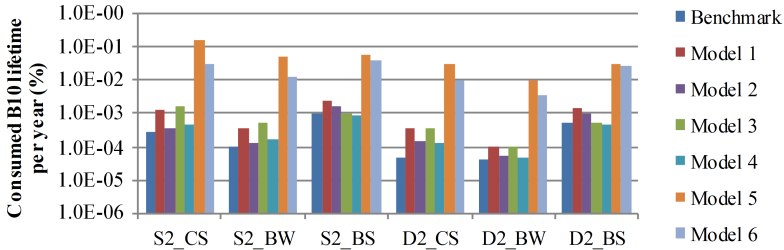
In the investigation, the manufacturer provides the  $B_{10}$  lifetime power cycling data. It means that the number of cycles where 10% of the modules of a population fail. The predicted lifetime based on the benchmark and different lifetime models is shown in Fig. 4.5.  $S_1$  and  $D_1$  denote IGBT<sub>2</sub> and its free-wheeling diode, and  $S_2$  and  $D_2$  are IGBT<sub>2</sub> and its diode. The consumed  $B_{10}$  lifetime of  $S_2$  is larger than  $S_1$

**Table 4.2:** Commonly-Employed Cycle to Failure Lifetime Models.

Model	Reference	Lifetime Models
1 (Coffin-Manson model)	[55]	$N_f = A\Delta T^{-n}$
2 (General Coffin-Manson)	[56]	$N_f = A(\Delta T - \Delta T_0)^{-n}$
3 (LESIT model)	[46]	$N_f = A\Delta T^{-n} \cdot \exp\left(\frac{E_a}{k_B T_m}\right)$
4 (General LESIT model)		$N_f = A(\Delta T - \Delta T_0)^{-n} \cdot \exp\left(\frac{E_a}{k_B T_m}\right)$
5 (Bayerer's model)	[58]	$N_f = A\Delta T^{-n} \cdot \exp\left(\frac{\beta_2}{T_{min}}\right) t_{on}^{\beta_3} I^{\beta_4} V^{\beta_5} D^{\beta_6}$
6 (General Bayerer's model)		$N_f = A(\Delta T - \Delta T_0)^{-n} \cdot \exp\left(\frac{\beta_2}{T_{min}}\right) t_{on}^{\beta_3} I^{\beta_4} V^{\beta_5} D^{\beta_6}$



(a)



(b)

**Fig. 4.5:** Comparison between  $B_{10}$  lifetime consumptions based on the aging data from the manufacturer (benchmark) and by six different lifetime models ( $S_1$  and  $D_1$  denote the IGBT<sub>1</sub> and its diode in the SM, and  $S_2$  and  $D_2$  are the IGBT<sub>2</sub> and its diode, CS – chip solder, BW – bond wire, and BS – base plate solder, see Table 4.2) [C2].

based on all the selected lifetime models. It is due to  $S_2$  of the MMC has more intensive thermal fluctuations than the other three power devices in an SM of the MMC. In addition, for the chip solder of  $S_1$  (labeled as  $S1\_CS$ ), the predicted lifetime consumptions based on lifetime models are larger than the benchmark result ( $1.129 \times 10^{-5}$  per year). Specifically, the commonly used Coffin-Manson model (i.e., Model 1) only considers the amplitude of temperature fluctuations. The corresponding obtained result is approximately ten times the benchmark. For Model 2 with consideration of the elastic strain range  $\Delta T_0$ , the predicted lifetime consumption (e.g.,  $S1\_CS$ ) is approaching the benchmark. It indicates that many small temperature variations  $\Delta T$

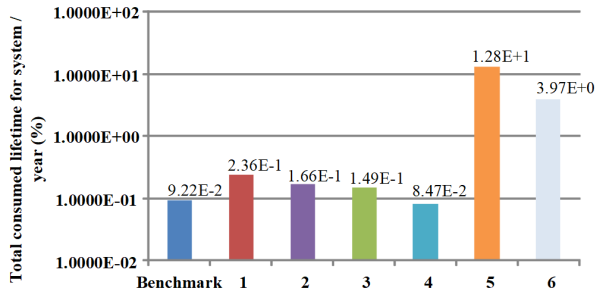


Fig. 4.6: Comparison of the lifetime consumption of the entire MMC system based on the six different lifetime models (consider the wear out of the power semiconductor devices only) [C2].

only induce elastic deformation. Furthermore, Model 3 considers the impact of the absolute temperature in the lifetime model (i.e.,  $T_{jm}$  in Model 3). For example, for the same  $\Delta T = 50^\circ\text{C}$ , devices with the average temperature of  $100^\circ\text{C}$  typically have more severe damages compared to devices under  $50^\circ\text{C}$  on average. As shown in Fig. 4.5, the predicted lifetime of S1\_CS is close to the benchmark. When both  $\Delta T_0$  and  $T_m$  are considered in Model 4, the predicted lifetime is further improved compared to the benchmark. These comparisons reveal the significance of both  $\Delta T_0$  and  $T_m$ . However, when Models 5 and Model 6 involve the power-on time  $t_{on}$ , large differences are observed compared to the benchmark. In the comparative study of different lifetime models, the resolution of mission profiles is 1 hour/data. The corresponding  $t_{on}$  is one hour at least, which far exceeds the typical effective range of  $t_{on}$  during 0.1-60 s. In conclusion, the selection of lifetime models significantly affect the predicted lifetime result. The selection of a specific lifetime model is necessary to consider the applicability, limitations, and effective ranges of each parameter.

Moreover, the predicted lifetime consumption of the entire MMC system due to wear outs is shown in Fig. 4.6. In this case, the studied MMC system has 72 SMs (i.e., 144 IGBT modules). The obtained lifetime by Model 4 is the closest to the benchmark, which means that both the elastic range  $\Delta T_0$  and absolute temperature significantly affect the predicted lifetime. On the contrary, the effective range of power-on time  $t_{on}$  should be carefully considered based on the applications.

In addition, the provided power cycling data of the IGBT module is  $B_{10}$  lifetime. Based on the manufacturer provided the factors 0.90 (for  $B_5$  lifetime) and 0.70 (for  $B_1$  lifetime) [72], the failure probability distribution due to device wear outs is shown in Fig. 4.7. The benchmark indicates that the MMC system has 10% IGBT due to wear-out failures within 10.8 years. Then, the predicted lifetimes based on Model 1 to Model 3 are 4.2, 6.0, and 6.7 years, respectively. For Model 4 with consideration of the temperature amplitude, elastic region and absolute temperature, the predicted lifetime around 11.8 years is the closest to the benchmark. It can conclude again that the elastic region and the absolute temperature are important to lifetime prediction. On the contrary, Model 5 and model 6 consider more parameters including the power-on time, but the predicted lifetime is smaller than one year. The large difference compared to the benchmark is due to the power-on time of the application beyond

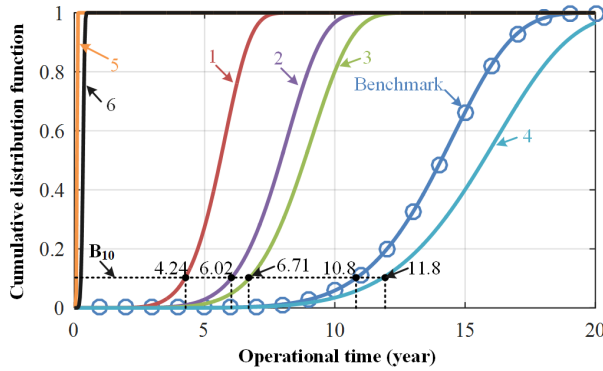


Fig. 4.7: Cumulative distribution function of the end-of-life of the MMC due to the wear-out fatigue of power semiconductor devices [C2].

the effective range of the lifetime model. Consequently, the lifetime model selection should consider various factors as well as the effective ranges of each parameter.

## 4.4 System-level Reliability Assessment

Based on the aforementioned power loss models, thermal models, and investigations of mission profiles and lifetime models. This part is aimed to establish a mission profile-based lifetime prediction for the system-level of the MMC. In order to fully consider the experimental parameters in Chapter 2 and validated thermal models in Chapter 3, the system-level lifetime prediction is based on the down-scale MMC prototype (see Fig. 2.3).

### 4.4.1 Thermal Profiles and Static Annual Damage of Components

According to the above comparative investigation of mission profiles with various resolutions, one-year wind speeds with a sampling frequency of 1 Hz is adopted here, as shown in Fig. 4.8. The corresponding converted active power profiles are also shown in Fig. 4.8. The conversion process considers the dynamics of the wind farm. The reactive power is set to be constant at 0.4 p.u. throughout the year.

Based on the established electro-thermal models in Chapter 3, the one-year mission profiles are converted into the thermal profiles for components as shown in Fig. 4.9. The global ambient temperature is set as 28°C in the case. The local ambient temperature of SM6 and SM16 fluctuates around 38°C and 50°C, respectively, as shown in Figs. 4.9(a) and (b). The local ambient temperature of SM16 is obviously more severe than the SM6 in terms of the average value and fluctuations. Regarding the junction temperatures of power devices, although the power losses of the four power devices in an SM are significantly different from each other as discussed in Chapter 2, the corresponding junction temperatures are not divergent remarkably.

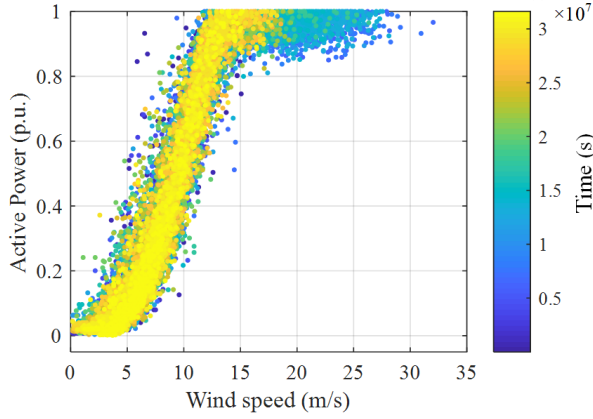


**Fig. 4.8:** One-year wind-speed mission profiles with resolution of 1 s/data and the corresponding converted active power profiles [J4].

The device  $S_2$  has the highest power dissipations, and its junction temperature is the highest. The other three junction temperatures are close to each other. These phenomena are due to the TCC effects of the thermal model as mentioned in Chapter 3. Meanwhile, the varied local ambient temperatures affect the capacitor hotspot temperatures, as shown in Fig. 4.9(c). The capacitor hotspot temperatures of SM16 are more significant in both the maximum hotspot temperature and the temperature distribution. Comparing the obtained thermal profiles in SM6 and SM16, the SMs of the MMC bear the different thermal stresses even if they have relatively equal power losses.

Following, the temperature swings in the power devices induce repetitive thermo-mechanical stresses, accumulated as fatigue, and finally also challenge the lifetime. According to the above investigations of the lifetime model selection, the temperature swings, absolute temperature, and power-on time are affected significantly the predicted lifetime results, and should be considered carefully. Combining the manufacturer provided data [57], the lifetime model for the selected IGBT module is

$$N_f = A(\Delta T_j)^{\beta_1} \cdot \exp\left(\frac{\beta_2}{T_{jmax} + 273}\right) \cdot \left(\frac{t_{on}}{1.5}\right)^{\beta_3}, \quad (4.1)$$

where  $N_f$  is the number of cycles to failure,  $\Delta T_j$  is the junction temperature fluctuation,  $T_{jmax}$  is the maximum junction temperature,  $t_{on}$  is the power-on time, and  $A$ ,  $\beta_1$ ,  $\beta_2$  and  $\beta_3$  are coefficients based on the power-cycling data. Based on [57], the parameters are  $A = 1.42 \times 10^{12}$ ,  $\beta_1 = -7.14$ ,  $\beta_2 = 5154$ ,  $\beta_3 = -0.3$ . Notably,  $t_{on}$  has limitations of  $0.1 \text{ s} < t_{on} < 60 \text{ s}$ .

The lifetime of Al-Caps is affected by the temperature stresses and the voltage stress, as presented in [73] and [63], which is given by

$$L_c = L_{c0} \cdot 2^{\frac{T_0 - T}{n_1}} \cdot \left(\frac{U}{U_0}\right)^{-n_2}, \quad (4.2)$$

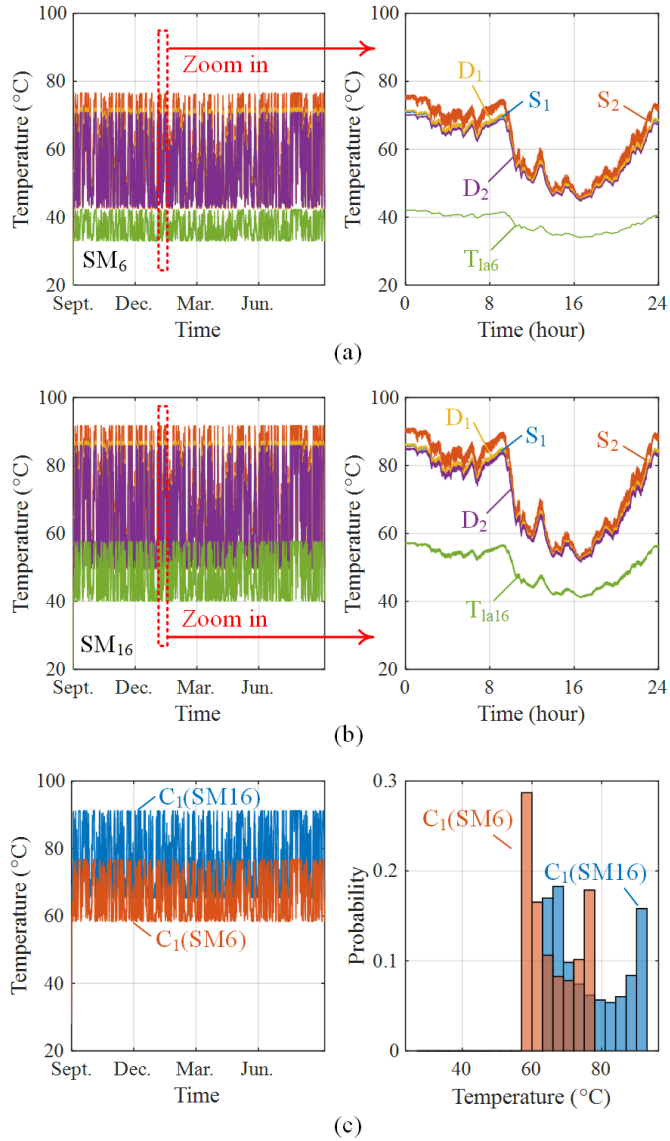


**Fig. 4.9:** Simulated temperature profile for the critical components ( $S_1$ ,  $S_2$ ,  $D_1$ ,  $D_2$ ,  $C_1$ ) and local ambient temperatures for different SMs: (a) SM6, (b) SM16, and (c) capacitor hotspot temperatures and its distributions when applying the annual wind speed mission profile [J4].

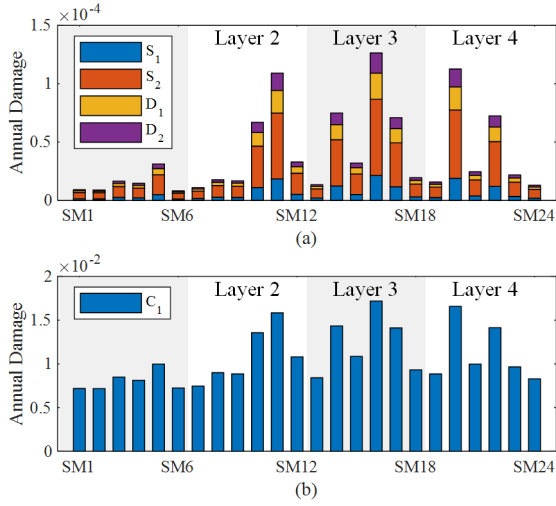


**Fig. 4.10:** Static annual damages of IGBTs and capacitors in the 24 SMs of the down-scale MMC prototype: (a) power semiconductor devices and (b) capacitors [J4].

where  $L_c$  is the lifetime under the thermal stress  $T$  and voltage stress  $U$ , while  $L_{c0}$  is the lifetime under the reference thermal and electrical conditions  $T_0$  and  $U_0$ .  $n_1$  and  $n_2$  are fitting coefficients relying on different manufacturers and technologies. In the case, the parameters has  $n_1 = 10$  and  $n_2 = 5$  according to [73].

The total damage for a device is accumulated based on Miners rules [74] as

$$D_{mg} = \sum_k \frac{n_k}{N_{fk}}, \quad (4.3)$$

where  $n_k$  is the amount of total cycles with a specific stress, and  $N_{fk}$  is the amount of cycles till failure for the same stress. The end-of-life of a device is achieved when the accumulative damage  $D_{mg}$  reaches one.

Then, the static annual damages due to wear-out of IGBT modules and capacitors are shown in Fig. 4.10. The different SMs have various annual wear-out damages regarding the power devices and capacitors, even the same IGBT module and capacitor are utilized in the prototype. As shown in Fig. 4.10(a), the total damage of power devices in SM6 is only  $0.1 \times 10^{-4}$  per year, while the damage of SM16 is up to  $1.3 \times 10^{-4}$  per year. Furthermore, the annual damages due to wear-out of the capacitors are much more severe than the power devices, as shown in Fig. 4.10(a). A single capacitor in SM16 has damage of  $1.7 \times 10^{-2}$  per year, which is almost 100 times the damages of the power devices. Moreover, the capacitor damages also vary with different SMs. The devices in different SMs withstands significant different stresses, which may induce a certain of SMs with shorter lifetime.



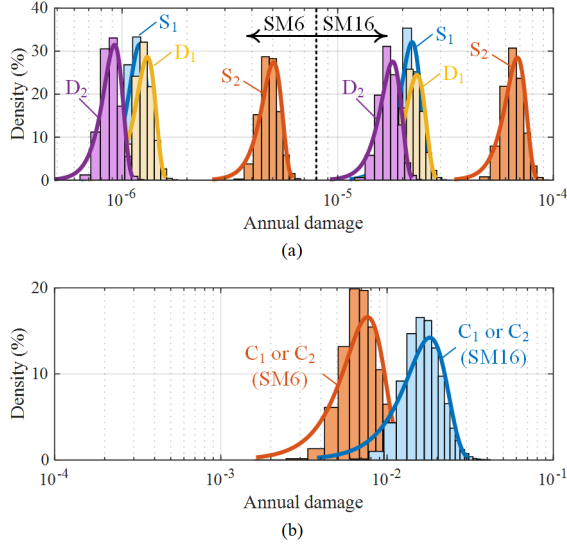


**Fig. 4.11:** Monte Carlo simulations of the critical components in SM6 and SM16: (a) power semiconductor devices and (b) capacitors [J4].

#### 4.4.2 Monte Carlo Simulations and System-Level Failure Probability Calculation

The static damage is established based on the normal parameters. However, the lifetime of a device is affected by many uncertainties in real applications, such as the variation of device parameters, the lifetime model parameters, etc. Thus, it is necessary to take the relevant uncertainties into account. Monte Carlo simulations are carried out here. The measured parameter uncertainties of the used devices in Chapter 2 and the varied lifetime parameters in (4.1) and (4.2) are considered. Consequently, the obtained Monte Carlo results of different devices in SM6 and SM16 are shown in Fig. 4.11. For the power semiconductor devices as shown in Fig. 4.11(a), the device  $S_2$  has always the largest annual damage distribution, which is centered around  $5 \times 10^{-6}$  per year for SM6 and  $5 \times 10^{-4}$  per year for SM16, respectively. Moreover, the damage distributions of all-power devices in SM16 are larger than those in SM6. It reveals the significant impacts of the different local ambient temperatures. Additionally, the annual damages of capacitors in both SMs are shown in Fig. 4.11(b). The capacitor damages are centered around  $1 \times 10^{-2}$  per year and significantly surpass the power semiconductors. It implies the capacitor has a shorter lifetime than the power semiconductor devices in an SM.

Accordingly, the Monte Carlo histograms are fitted with the Weibull distribution as

$$f(t) = \frac{\beta}{\eta} \left( \frac{t}{\eta} \right)^{\beta-1} e^{-\left( \frac{t}{\eta} \right)^\beta}, \quad (4.4)$$

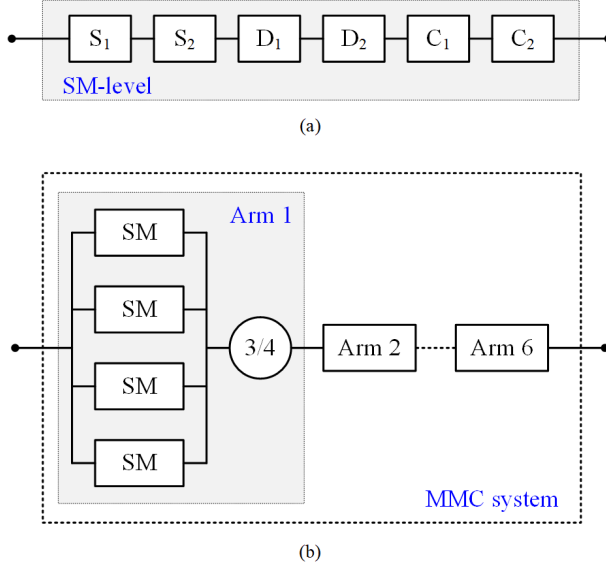


**Fig. 4.12:** System-level lifetime analysis based on reliability block diagram: (a) composition of an SM (four power semiconductor devices and two capacitors) and (b) composition of the entire MMC system, where the arm is 3-out-of-4 system [J4].

$$F(t) = 1 - e^{-\left(\frac{t}{\eta}\right)^\beta}, \quad (4.5)$$

where  $\beta$  and  $\eta$  are the shape and the scale parameters, respectively.  $f(t)$  is the probability density function in terms of time  $t$ , and  $F(t)$  is the accumulated failure probability.

Based on the aforementioned reliability information of the devices, the system-level reliability assessment of the MMC follows the steps from the SM-level, arm-level, to entire system. Each level of reliability analysis is calculated via the Reliability Block Diagram (RBD) as shown in Fig. 4.12. For the reliability of an SM, all the power devices and capacitors are serially connected in the RBD. It implies any failed single device will lead to the failure of the SM. Therefore, the corresponding failure function  $F_{SMi}$  and reliability function  $R_{SMi}$  of the  $i$ -th SM are given by the component failure function  $F_{comj}$

$$F_{SMi}(t) = 1 - \prod_{j=1}^6 [1 - F_{comj}(t)], \quad (4.6)$$

$$R_{SMi}(t) = \prod_{j=1}^6 [1 - F_{comj}(t)]. \quad (4.7)$$

The component-level and corresponding SM-level failure probabilities of SM6 and SM16 are shown in Figs. 4.13(a) and (b), respectively. The failure probabilities of IGBTs/diodes of both SMs are almost zero. By contrast, the failure probability of

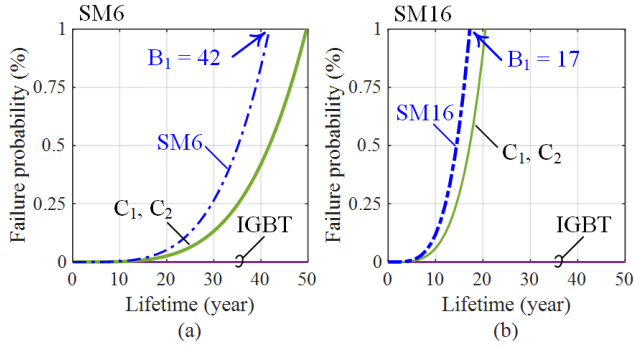


**Fig. 4.13:** Failure probability due to wear out of IGBTs and capacitors in two SMs: (a) SM6 and (b) SM16 [J4].

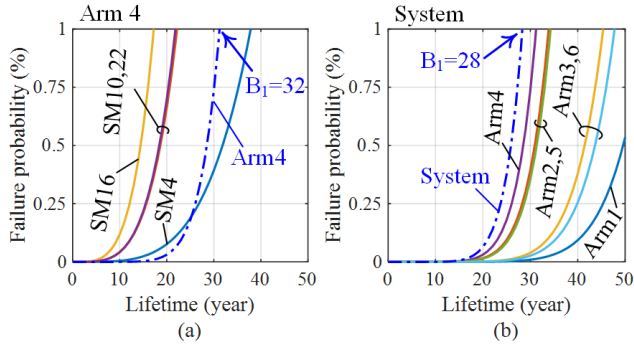


**Fig. 4.14:** Accumulated percentage of wear-out failure probability of the MMC system: (a) from the SM level to the arm level and (b) from the arm level to the system level [J4].

capacitors rapidly increases. It implies that the power semiconductor devices may have excessive design margins in this case. The reliability of the capacitors dominates the lifetimes of SMs. The  $B_1$  lifetimes (1% devices fail) of the capacitors in both SMs are within 50 and 20 years, respectively. Simultaneously, the  $B_1$  lifetimes of SM6 and SM16 due to wear out are within 42 and 17 years, respectively.

Afterwards, the reliability analysis of the entire MMC system is shown in Fig. 4.12(b). In each arm, a 3-out-of-4 redundancy is applied to improve the reliability performance. Taking the first arm as an example, which consists of SM1, SM7, SM13 and SM19, the failure function of the arm is expressed as

$$\begin{aligned}
 F_{\text{arm1}}(t) &= 1 - R_{\text{SM1}}(t)R_{\text{SM7}}(t)R_{\text{SM13}}(t)R_{\text{SM19}}(t) \\
 &\quad - F_{\text{SM1}}(t)R_{\text{SM7}}(t)R_{\text{SM13}}(t)R_{\text{SM19}}(t) \\
 &\quad - R_{\text{SM1}}(t)F_{\text{SM7}}(t)R_{\text{SM13}}(t)R_{\text{SM19}}(t) \\
 &\quad - R_{\text{SM1}}(t)R_{\text{SM7}}(t)F_{\text{SM13}}(t)R_{\text{SM19}}(t) \\
 &\quad - R_{\text{SM1}}(t)R_{\text{SM7}}(t)R_{\text{SM13}}(t)F_{\text{SM19}}(t).
 \end{aligned} \tag{4.8}$$

**Table 4.3:** Comparison of the Down-scale Prototype and Full-scale MMC Systems and Corresponding References [J4].

Categories	Down-scale prototype	Full-scale MMC
Power semiconductors	IGBT power modules	Press-pack IGBT devices [75, 76] IGCT [77]
Capacitors	Al-capacitors	Film capacitors [63, 76]
Magnetic components	Iron-core inductors	Air-core inductors [78]
Cooling methods	Forced air-cooling	Liquid cooling [79] Optical fibers [80]
Other components	None	Control board [81] Mechanical parts [82]

Furthermore, the system-level reliability is also a serial connection of six arms. The failure function, thus, is estimated by

$$F_{\text{system}}(t) = 1 - \prod_{j=1}^6 [1 - F_{\text{armi}}(t)]. \quad (4.9)$$

The corresponding arm-level and system-level reliability results are shown in Fig. 4.14. In Fig. 4.14(a), four different SMs have variable failure probabilities. Due to the redundant structure, the failure probability of the arm is smaller than all the consisting SMs in the first 25 years. After the 25<sup>th</sup> year, the unreliability is soaring and surpasses the failure probability of SM4. The  $B_1$  lifetime of the arm is within 32 years. On the other hand, Fig. 4.14(b) depicts reliable relationship between each arm and the system. Arm 1 has the lowest failure probability while Arm 4 has the worst reliability in the entire system. Since the whole system is a serial connection, the reliability of the entire system is worse than all arms. The  $B_1$  lifetime of the MMC is within 28 years. So far, the reliability assessment of the whole MMC platform has been established, which covers from single components to the composition of the SM or the arm. Although the annual damage of a single power device is as low as  $1 \times 10^{-6}$  per year, the  $B_1$  lifetime of the entire system is within 28 years only.

### 4.4.3 Discussion

This chapter limits its scope to the wear-out failure of IGBTs and capacitors. It provides a potential method to size IGBTs and capacitors according to mission profile based reliability prediction. It also demonstrates a systematic methodology to perform reliability analysis from system-level modeling to component-level modeling, and then back to the system-level reliability. The same method could be applied to other types of components.

Table 4.3 lists the differences between the down-scale prototype and full-scale MMC systems. A typical full-scale MMC utilizes 4.5 kV/1.2 kA power modules [9], instead of the power module of 1.2 kV/50 A in the prototype. Meanwhile, other options for power devices usually have press-pack IGBTs, IGCT, etc [75–77]. For passive components, full-scale MMC systems use more high-power film capacitors as they provide higher voltage ratings and better reliability performance [63]. The different

failure mechanisms are necessary to be considered in terms of different packaging technologies and devices.

Moreover, single-event related failure of MMC is also an important part to be considered in the design and system-level reliability analysis, such as liquid cooling systems [79], optical fibers [80], control boards [81], mechanical parts [82], etc. It relies more on the field operation experiences of the specific type of MMCs or similar products. From the design perspective, proper protection strategies and robustness design are beneficial to the reduction of this type of failure.

## 4.5 Summary

Mission profile-based lifetime prediction for the MMC has been discussed in the chapter, focusing on the impact of mission profiles, the selection of lifetime models, and the system-level reliability assessment.

For the mission profile investigation, annual wind speeds with four different resolutions are considered, i.e., 1 s/data, 10 minute/data (standard SCADA system), 1 hour/data, and remodeled 1 s/data. In addition, the wind profiles are converted into power information via two different power conversion models, namely IEC 61400-12-1 power curves and the stochastic model. The predicted lifetime results are compared. In conclusion, the wind profile with 10 minute/data and 1 hour/data are not sufficient to represent the thermal dynamics in the range of seconds, which might result in overoptimistic lifetime estimation. Moreover, IEC 61400-12-1 power curve is limited to convert high-resolution wind profiles (e.g., 1 s/data). The remodeled 1-s/data wind profile is able to achieve an acceptable predicted lifetime result.

The lifetime model study compares six commonly used models to the manufacturer provided aging data. The lifetime models with consideration of the elastic deformation and the absolute temperature (e.g., the mean temperature) can improve the accuracy of the predicted lifetime. However, the consideration of power-on time should refer to the effective range. The lifetime model selection should be careful to consider the power cycling ranges.

Finally, based on a 15-kVA experimental prototype, this chapter provides a system-level methodology to assess the reliability of the MMC, covering the critical components, subsystems, and the entire system. The diverse annual damages among devices and SMs comprehensively illustrate the impacts of the uneven parameters and the complicated thermal behaviors in the MMC. The annual damage of a single component is as low as  $1 \times 10^{-6}$  per year, but the accumulated failure (%) due to the wear out of IGBTs and capacitors in the MMC is 1% at 20 years of operation. This phenomenon emphasizes the severe reliability challenges in the MMC in terms of components and system integrations. The results also provide a guideline for the sizing of critical components and the physical layout of SMs.



# Chapter 5

## Conclusions

This chapter summarizes the results and outcomes of the research during the Ph.D. study. The main contributions and research perspectives are discussed.

### 5.1 Summary

In the Ph.D. project, the main research focus is on evaluating the reliability performance of MMCs. Several challenging issues for power loss models, electro-thermal models, lifetime prediction methods have been discussed, and corresponding solutions are proposed. In the following, a summary of this Ph.D. thesis is presented.

In Chapter 1, the demands and challenges for MMCs have been discussed. As the MMC plays a critical role in HVDC transmissions, one of the significant challenges is how to design an MMC with compromised design margins and costs while fulfilling a specific reliability target. This target relies on a system-level reliability assessment. The power loss models, electro-thermal models, and lifetime prediction methods are prerequisites in the process and meanwhile associated with many challenges.

One potential problem is the power loss model of the MMC involving many components (e.g., IGBTs, capacitors, inductors, bleeding resistors, etc.), which consume a large computational burden if they are analyzed for long-term serve time. Moreover, power loss evaluation requires much device-level electrical information, such as currents and voltages of devices, modulation indexes, etc. However, this information is usually inaccessible for reliability evaluation in an initial design stage, where mission profiles commonly provide the system-level information only (e.g., active/reactive information at the PCC). Therefore, from the perspective of system-level reliability analysis of the MMC, power losses evaluation requires computational efficiency, involving all critical components, and utilization of system-level specifications only. The solutions to fulfill these requirements have been discussed in Chapter 2. A system-level power loss analytical power loss model has been established. All critical components in the MMC are covered, which considers the impacts of uneven device parameters and variation of mission profiles.

Chapter 3 discussed the electro-thermal model of the MMC based on the different

responses described in the frequency domain. The periodic and non-periodic profiles are discussed separately. For periodic profiles, one of the challenges is to model the inherent thermal unbalance computationally-efficiently while still keep a small error. This chapter proposes an equivalent power loss profile to model the varied periodic power loss profiles. Meanwhile, an error model is established to simplify the proposed equivalent power loss profile within a quantitative error. Moreover, non-periodic profiles involve many components, SMs, and systems. The time scales are across seconds, minutes, and even longer, which inevitably induce complicated TCC effects among them. Therefore, the junction/hotspot-to-local ambient thermal model and local ambient-to-global ambient thermal model are investigated in the Ph.D. project. The hierarchical thermal model considers the TCC effects among devices and subsystems comprehensively. Apart from the two different thermal profiles, TIMs have also been discussed from the impact on the predicted lifetime and characterization model. The corresponding results show a significant impact of TIMs.

Finally, reliability performance is evaluated in Chapter 4. The resolution of the mission profile is investigated at first. The annual wind speeds with 1 s/data are recommended considering the high dynamics of power devices. Afterwards, a comparative study has been carried out on the lifetime model selection. It reveals that the commonly used Coffin-Manson model may lead to a significant difference compared to the benchmark from power cycling data. Based on the discussions above, a system-level reliability prediction is conducted. Different stresses in various SMs and redundancies are discussed. The outcomes serve as a first step for developing realistic reliability analysis and model-based design methods for full-scale MMCs in practical applications.

## 5.2 Main Contributions

The main contributions of the Ph.D. projects are summarized as follows:

### A) System-level Power Loss Model for MMCs

- The proposed power loss model covers all major components, including IGBTs, capacitor, inductors, bleeding resistors;
- The proposed analytical model is computationally efficient, and based on the active and reactive power information at the PCC;
- The analytical process considers the component tolerances.

### B) Comprehensive electro-thermal model of MMCs

- Thermal profiles of typical power electronic systems are classified into periodic and non-periodic profiles. The corresponding thermal estimation requirements are discussed based on the frequency-domain analysis;
- An equivalent power loss profile is proposed to consider the inherent thermal unbalance of the MMC;
- An error model is proposed to simplify the thermal estimation of periodic profiles within a quantitative error level;



- A system-level thermal model is proposed based on the MMC prototype, which comprehensively considers the TCC effects among devices, different subsystems, and also the impact of the cabinet and layout;
- The impact of the TIM is also investigated from the perspective of reliability;
- An empirical model is proposed to characterize the thermal resistance of TIMs under realistic conditions.

### C) System-level evaluation of MMCs

- The impact of mission profile models is investigated, which points out the requirement of high-resolution mission profiles and appropriate power conversion models;
- The impact of lifetime model selection is investigated, which emphasizes the significant impact of the lifetime model selection;
- System-level reliability evaluation is carried on the MMC, which considers the uneven stresses of different SMs and including also the redundancies. The outcomes serve as a first step for developing realistic reliability analysis and model-based design methods for full-scale MMCs in practical applications.

## 5.3 Research Perspectives

Although several aspects of the reliability evaluation of MMCs have been investigated in this Ph.D. project, there are still some challenges requiring to be addressed:

- The proposed power loss model has been verified by a 15-kVA down-scale prototype, where the major components are Si-based IGBTs, Al-Caps, and iron-core inductance. However, for the full-scale MMC, there is still a lack of experimental verifications. As the full-scale MMC may use different types of components, a practical validation is necessary when extending the proposed method to the full-scale MMC.
- A comprehensive thermal analysis of the MMC is provided from different time scales (i.e., periodic and non-periodic profiles) to different spatial scales (e.g., device level, SM level, system-level). However, the thermal model requires complicated FEM simulations. A simplified analytical thermal model is beneficial for reducing the computational burden.
- The reliability evaluation considers the wear-out failure of IGBTs and capacitors. However, many failure modes for MMCs, such as random failures, software failures, cooling systems, gate drivers, optical fibers, and the failure of other components, are not considered. It relies more on the field operation experiences of the specific type of MMCs or similar products. From a design perspective, proper protection strategies and robustness design are beneficial to the reduction of this type of failure.
- The identification of parameter sensitivity is necessary, which includes device parameters, thermal-model parameters, and lifetime model parameters.

- Validation of a full-scale SM is important, for example, accelerated tests.
- It is essential to apply the proposed method in varied conditions, such as varied control commands, environmental parameters, etc.

# Bibliography

## References

- [1] A. Lesnicar and R. Marquardt, "An innovative modular multilevel converter topology suitable for a wide power range," in *Proc. IEEE Bol. PowerTech Conf.*, 2003, pp. 272–277.
- [2] A. Nami, J. Liang, F. Dijkhuizen, and G. D. Demetriades, "Modular multilevel converters for HVDC applications: Review on converter cells and functionalities," *IEEE Trans. Power Electron.*, vol. 30, no. 1, pp. 18–36, 2015.
- [3] H. Akagi, "Classification, terminology, and application of the modular multilevel cascade converter (MMCC)," *IEEE Trans. Power Electron.*, vol. 26, no. 11, pp. 3119–3130, Nov. 2011.
- [4] S. Debnath, J. Qin, B. Bahrani, M. Saeedifard, and P. Barbosa, "Operation, control, and applications of the modular multilevel converter: a review," *IEEE Trans. Power Electron.*, vol. 30, no. 1, pp. 37–53, Jan. 2015.
- [5] M. A. Perez, S. Bernet, J. Rodriguez, S. Kouro, and R. Lizana, "Circuit topologies, modelling, control schemes and applications of modular multilevel converters," *IEEE Trans. Power Electron.*, vol. 30, no. 1, pp. 4–17, Mar. 2015.
- [6] M. Hagiwara, K. Nishimura, and H. Akagi, "A medium-voltage motor drive with a modular multilevel PWM inverter," *IEEE Trans. Power Electron.*, vol. 25, no. 7, pp. 1786–1799, Jul. 2010.
- [7] A. Antonopoulos, L. Ångquist, S. Norrga, K. Ilves, L. Harnefors, and H. P. Nee, "Modular multilevel converter AC motor drives with constant torque from zero to nominal speed," *IEEE Trans. Ind. Appl.*, vol. 50, no. 3, pp. 1982–1993, May/Jun. 2014.
- [8] H. Wang, G. Tang, Z. He, and J. Yang, "Efficient grounding for modular multilevel HVDC converters (MMC) on the AC side," *IEEE Trans. Power Deliv.*, vol. 29, no. 3, pp. 1262–1272, Jun. 2014.
- [9] K. Sharifabadi, L. Harnefors, H.-P. Nee, R. Teodorescu, and S. Norrga, *Design, Control and Application of Modular Multilevel Converters for HVDC Transmission Systems*. John Wiley & Sons, 2016.

- [10] M. Davies, M. Dommaschk, J. Dorn, J. Lang, D. Retzmann, and D. Soerangr, *HVDC PLUS: Basics and Principle of Operation*. Siemens AG, 2008.
- [11] S. Yang, A. Bryant, P. Mawby, D. Xiang, L. Ran, and P. Tavner, "An industry-based survey of reliability in power electronic converters," *IEEE Trans. Ind. Appl.*, vol. 47, no. 3, pp. 1441–1451, Mar. 2011.
- [12] ZVEL, "Handbook for robustness validation of automotive electrical/electronic modules," Tech. Rep., Jun. 2008.
- [13] J. Glasdam, J. Hjerrild, L. H. Kocewiak, and C. L. Bak, "Review on multi-level voltage source converter based HVDC technologies for grid connection of large offshore wind farms," in *Proc. IEEE Int. Conf. Power Syst. Technol. POWERCON*, 2012, pp. 1–6.
- [14] ABB, "HVDC Light. It's time to connect," 2017. [Online]. Available: <https://search-ext.abb.com/library/Download.aspx?DocumentID=POW-0038&LanguageCode=en&DocumentPartId={&}Action=Launch>
- [15] G. Konstantinou, J. Pou, S. Ceballos, and V. G. Agelidis, "Active redundant submodule configuration in modular multilevel converters," *IEEE Trans. Power Del.*, vol. 28, no. 4, pp. 2333–2341, Oct. 2013.
- [16] O. Cwikowski, H. R. Wickramasinghe, G. Konstantinou, J. Pou, M. Barnes, and R. Shuttleworth, "Modular multilevel converter DC fault protection," *IEEE Trans. Power Del.*, vol. 33, no. 1, pp. 291–300, Feb. 2017.
- [17] B. Wang, X. Wang, Z. Bie, P. D. Judge, X. Wang, and T. C. Green, "Reliability model of MMC considering periodic preventive maintenance," *IEEE Trans. Power Deliv.*, vol. 32, no. 3, pp. 1535–1544, Jun. 2017.
- [18] J. Xu, P. Zhao, and C. Zhao, "Reliability analysis and redundancy configuration of MMC with hybrid submodule topologies," *IEEE Trans. Power Electron.*, vol. 31, no. 4, pp. 2720–2729, Apr. 2016.
- [19] P. Tu, S. Yang, and P. Wang, "Reliability- and cost-based redundancy design for modular multilevel converter," *IEEE Trans. Ind. Electron.*, vol. 66, no. 3, pp. 2333–2342, Mar. 2019.
- [20] "Military handbook: Reliability prediction of electronic equipment MIL-HDBK-217F," Tech. Rep., 1991.
- [21] K. Ma, H. Wang, and F. Blaabjerg, "New approaches to reliability assessment - using physics-of-failure for prediction and design in power electronics systems," *IEEE Power Electron. Mag.*, vol. 3, no. 4, pp. 28–41, 2016.
- [22] H. Liu, K. Ma, Z. Qin, P. C. Loh, and F. Blaabjerg, "Lifetime estimation of MMC for offshore wind power HVDC application," *IEEE J. Emerg. Sel. Topics Power Electron.*, vol. 4, no. 2, pp. 504–511, Sep. 2016.

- [23] Y. Zhang, H. Wang, Z. Wang, Y. Yang, and F. Blaabjerg, "Impact of lifetime model selections on the reliability prediction of IGBT modules in modular multilevel converters," in *Proc. IEEE Energy Conversion Congress and Exposition*, 2017, pp. 4202–4207.
- [24] IEC-62751-2, "Determination of power losses in voltage sourced converter (VSC) valves for HVDC systems - Part 2: modular multilevel converters," 2012.
- [25] A. Christe and D. Dujic, "Virtual submodule concept for fast semi-numerical modular multilevel converter loss estimation," *IEEE Trans. Ind. Electron.*, vol. 64, no. 7, pp. 5286–5294, 2017.
- [26] S. Rohner, S. Bernet, M. Hiller, and R. Sommer, "Modulation, losses, and semiconductor requirements of modular multilevel converters," *IEEE Trans. Ind. Electron.*, vol. 57, no. 8, pp. 2633–2642, 2010.
- [27] H. Wang, G. Tang, Z. He, and J. Cao, "Power loss and junction temperature analysis in the modular multilevel converters for HVDC transmission systems," *J. of Power Electron.*, vol. 15, no. 3, pp. 685–694, May 2015.
- [28] T. Modeer, H. P. Nee, and S. Norrga, "Loss comparison of different sub-module implementations for modular multilevel converters in HVDC applications," in *EPE J. (European Power Electron. Drives Journal)*, vol. 22, no. 3, 2012, pp. 32–38.
- [29] Z. Zhang, Z. Xu, and Y. Xue, "Valve losses evaluation based on piecewise analytical method for MMC-HVDC links," *IEEE Trans. Power Deliv.*, vol. 29, no. 3, pp. 1354–1362, Jun. 2014.
- [30] S. Rodrigues, A. Papadopoulos, E. Kontos, T. Todorovic, and P. Bauer, "Steady-state loss model of half-bridge modular multilevel converters," *IEEE Trans. Ind. Appl.*, vol. 52, no. 3, pp. 2415–2425, 2016.
- [31] L. Yang, Y. Li, Z. Li, P. Wang, F. Gao, and F. Xu, "A simplified loss model of modular multilevel converter," in *IEEE PES Asia-Pacific Power Energy Conf.*, 2016, pp. 661–665.
- [32] L. Wu, J. Qin, M. Saeedifard, and O. Wasynczuk, "Efficiency evaluation of the modular multilevel converter based on Si and SiC switching devices for medium / high-voltage applications," *IEEE Trans. Electron Devices*, vol. 62, no. 2, pp. 286–293, Feb. 2015.
- [33] "Operating Instructions–VLT 5000 FLUX," *Danfoss*, 2005.
- [34] K. Ma, M. Liserre, F. Blaabjerg, and T. Kerekes, "Thermal loading and lifetime estimation for power device considering mission profiles in wind power converter," *IEEE Trans. Power Electron.*, vol. 30, no. 2, pp. 590–602, Mar. 2015.
- [35] Y. Shen, A. Chub, H. Wang, D. Vinnikov, E. Liivik, and F. Blaabjerg, "Wear-out failure analysis of an impedance-source PV microinverter based on system-level electrothermal modeling," *IEEE Trans. Ind. Electron.*, vol. 66, no. 5, pp. 3914–3927, May 2019.

- [36] D. Zhou, H. Wang, and F. Blaabjerg, "Mission profile based system-level reliability analysis of DC/DC converters for a backup power application," *IEEE Trans. Power Electron.*, vol. 33, no. 9, pp. 8030–8039, Aug. 2018.
- [37] F. Hahn, M. Andresen, G. Buticchi, and M. Liserre, "Thermal analysis and balancing for modular multilevel converters in HVDC applications," *IEEE Trans. Power Electron.*, vol. 33, no. 3, pp. 1985–1996, Mar. 2018.
- [38] W. Li, H. Yang, J. Sheng, C. Li, M. Chen, X. He, and X. Gu, "Thermal optimization of modular multilevel converters with surplus sub-module active-bypass plus neutral-point-shift scheme under unbalanced grid," *IEEE J. Emerg. Sel. Top. Power Electron.*, vol. PP, no. c, pp. 1–1, Early access, 2019.
- [39] J. Goncalves, D. J. Rogers, and J. Liang, "Submodule temperature regulation and balancing in modular multilevel converters," *IEEE Trans. Ind. Electron.*, vol. 65, no. 9, pp. 7085–7094, Sept. 2018.
- [40] Y. Dong, H. Yang, W. Li, and X. He, "Neutral-point-shift-based active thermal control for a modular multilevel converter under a single-phase-to-ground fault," *IEEE Trans. Ind. Electron.*, vol. 66, no. 3, pp. 2474–2484, 2019.
- [41] P. D. Reigosa, H. Wang, Y. Yang, and F. Blaabjerg, "Prediction of bond wire fatigue of IGBTs in a PV inverter under a long-term operation," *IEEE Trans. Power Electron.*, vol. 31, no. 10, pp. 7171–7182, Dec. 2016.
- [42] W. Lai, M. Chen, L. Ran, O. Alatise, S. Xu, and P. Mawby, "Low  $\Delta T_j$  stress cycle effect in IGBT power module die-attach lifetime modeling," *IEEE Trans. Power Electron.*, vol. 31, no. 9, pp. 6575–6585, Nov. 2016.
- [43] J. J. Jung, H. J. Lee, and S. K. Sul, "Control strategy for improved dynamic performance of variable-speed drives with modular multilevel converter," *IEEE J. Emerg. Sel. Topics Power Electron.*, vol. 3, no. 2, pp. 371–380, June 2015.
- [44] K. Ilves, A. Antonopoulos, S. Norrga, and H. P. Nee, "Steady-state analysis of interaction between harmonic components of arm and line quantities of modular multilevel converters," *IEEE Trans. Power Electron.*, vol. 27, no. 1, pp. 57–68, Jan. 2012.
- [45] K. Ma, A. S. Bahman, S. Beczkowski, and F. Blaabjerg, "Complete loss and thermal model of power semiconductors including device rating information," *Ieee Trans. Power Electron.*, vol. 30, no. 5, pp. 2556–2569, may 2015.
- [46] A. Wintrich, N. Ulrich, T. Werner, and T. Reimann, *Application Manual Power Semiconductors*. Nuremberg, Germany: Semikron Int.GmbH, 2015.
- [47] "Dimensioning program IPOSIM for loss and thermal calculation of Infineon IGBT modules," Infineon application notes, Tech. Rep.
- [48] S. Thomas, "Infineon AN2008-03: Thermal equivalent circuit models," Tech. Rep., 2008.

- [49] A. S. Bahman, K. Ma, P. Ghimire, F. Iannuzzo, and F. Blaabjerg, "A 3-D-lumped thermal network model for long-term load profiles analysis in high-power IGBT modules," *IEEE J. Emerg. Sel. Top. Power Electron.*, vol. 4, no. 3, pp. 1050–1063, Sept. 2016.
- [50] K. Ma, N. He, M. Liserre, and F. Blaabjerg, "Frequency-domain thermal modeling and characterization of power semiconductor devices," *IEEE Trans. Power Electron.*, vol. 31, no. 10, pp. 7183–7193, 2016.
- [51] A. standard, "Standard test method for thermal transmission properties of thermally conductive electrical insulation materials," *ASTM International*, 2006.
- [52] G. K. Morris, M. Polakowski, L. Wei, M. D. Ball, M. G. Phillips, C. Mosey, and R. A. Lukaszewski, "Thermal interface material evaluation for IGBT modules under realistic power cycling conditions," in *Proc. IEEE Integr. Power Packag.*, 2015, pp. 111–114.
- [53] B. R. Prasher, "Thermal interface materials : Historical perspective , status , and future directions," *Proc. IEEE*, vol. 94, no. 8, pp. 1571–1586, 2006.
- [54] I. Savija, J. R. Culham, and M. M. Yovanovich, "Effective thermophysical properties of thermal interface materials: part I definitions and models," in *Proc. Int. Electron. Packag. Tech. Conf. Exhib.*, 2003, pp. 1–7.
- [55] S. S. Manson and T. Dolan, "Thermal stress and low cycle fatigue," *J. Applied Mechanics*, vol. 33, p. 957, 1966.
- [56] H. Wang, K. Ma, and F. Blaabjerg, "Design for reliability of power electronic systems," in *Proc. 38<sup>th</sup> Annual Conf. IEEE Ind. Electron. Society*, 2012, pp. 33–44.
- [57] H. Ludwig, "AN2010-02 technical information: IGBT modules use of power cycling curves for IGBT4," pp. 1–6, 2010.
- [58] R. Bayerer, T. Herrmann, T. Licht, J. Lutz, and M. Feller, "Model for power cycling lifetime of igbt modules - various factors influencing lifetime," in *Proc. 5th Int. Conf. Integrated Power Electron. Systems*, March 2008, pp. 1–6.
- [59] P. D. Judge, G. Chaffey, M. M. Merlin, P. R. Clemow, and T. C. Green, "Dimensioning and modulation index selection for the hybrid modular multilevel converter," *IEEE Trans. Power Electron.*, vol. 33, no. 5, pp. 3837–3851, May 2018.
- [60] C. Oates, "Modular multilevel converter design for VSC HVDC applications," *IEEE J. Emerg. Sel. Top. Power Electron.*, vol. 3, no. 2, pp. 505–515, Jun. 2015.
- [61] T. Nakanishi and J. I. Itoh, "High power density design for a modular multilevel converter with an H-bridge cell based on a volume evaluation of each component," *IEEE Trans. Power Electron.*, vol. 33, no. 3, pp. 1967–1984, Mar. 2018.
- [62] Y. Zhang, H. Wang, Z. Wang, Y. Yang, and F. Blaabjerg, "Simplified thermal modeling for IGBT modules with periodic power loss profiles in modular multilevel converters," *IEEE Trans. Ind. Electron.*, vol. 66, no. 3, pp. 2323–2332, Apr. 2018.

- [63] H. Wang and F. Blaabjerg, "Reliability of capacitors for DC-link applications in power electronic converters—an overview," *IEEE Trans. Ind. Appl.*, vol. 50, no. 5, pp. 3569–3578, Sept./Oct. 2014.
- [64] ANSYS, "Maxwell Online Help," Canonsburg, PA, 2016.
- [65] N. C. Sintamarean, F. Blaabjerg, H. Wang, F. Iannuzzo, and P. De Place Rimmen, "Reliability oriented design tool for the new generation of grid connected PV-inverters," *IEEE Trans. Power Electron.*, vol. 30, no. 5, pp. 2635–2644, May. 2015.
- [66] L. Pan and C. Zhang, "A high power density integrated charger for electric vehicles with active ripple compensation," *Math. Probl. Eng.*, 2015.
- [67] Z. Wang, H. Wang, Y. Zhang, and F. Blaabjerg, "A viable mission profile emulator for power modules in modular multilevel converters," *IEEE Transactions on Power Electronics*, pp. 1–1, early access.
- [68] M. Schulz, S. T. Allen, D. Phan, and P. Wilhelm, "The crucial influence of thermal interface material in power electronic design," 2013. [Online]. Available: <http://www.imapsfrance.org/puissance2013/4-Henkel.pdf>
- [69] P. Milan, M. Wächter, and J. Peinke, "Stochastic modeling and performance monitoring of wind farm power production," *Journal of Renewable and Sustainable Energy*, vol. 6, no. 3, p. 033119, 2014.
- [70] IEC61400-12-1, "Wind energy generation systems - Part12-1: Power performance measurements of electricity producing wind turbines."
- [71] M. Held, P. Jacob, G. Nicoletti, P. Scacco, and P. M.-H., "Fast power cycling test of igbt modules in traction application," *International Journal of Electronics*, vol. 86, no. 10, 1999.
- [72] E. Özkol, S. Hartmann, and H. Duran, "Load-cycling capability of HiPak<sup>TM</sup> IGBT modules 5SYA2043-03," Tech. Rep., 2012.
- [73] D. Zhou, Y. Song, Y. Liu, and F. Blaabjerg, "Mission profile based reliability evaluation of capacitor banks in wind power converters," *IEEE Trans. Power Electron.*, vol. 34, no. 5, pp. 4665–4677, May 2019.
- [74] M. A. Miner, "Cumulative damage in fatigue," *American Society of Mechanical Engineers - Journal of Applied Mechanics*, vol. 12, pp. 159–164, 1945.
- [75] H. Y. Long, M. R. Sweet, E. M. S. Narayanan, and G. Li, "Reliability study and modelling of igbt press-pack power modules," in *2017 IEEE Applied Power Electronics Conference and Exposition (APEC)*, March 2017, pp. 2711–2717.
- [76] L. Hui, Z. Meimei, Y. Ran, L. Wei, D. Jili, L. Haiyang, and Q. Haitao, "Reliability modelling and analysis on MMC for VSC-HVDC by considering the press-pack IGBT and capacitors failure," *J. Eng.*, vol. 2019, no. 16, pp. 2219–2223, 2019.



- [77] B. Zhao, R. Zeng, Z. Yu, Q. Song, Y. Huang, Z. Chen, and T. Wei, "A more prospective look at IGCT: uncovering a promising choice for dc grids," *IEEE Ind. Electron. Mag.*, vol. 12, no. 3, pp. 6–18, Sept. 2018.
- [78] Z. Yuan, J. J. He, Y. Pan, X. G. Yin, C. Ding, S. F. Ning, and H. L. Li, "Thermal analysis of air-core power reactors," *ISRN Mech. Eng.*, vol. 2013, pp. 1–7, 2013.
- [79] G. Bing, H. Tingting, Y. Fan, L. Chao, S. Xiaoning, and C. Yijie, "Investigation on deposition behavior of HVDC water cooling system based on electro-mass transfer-velocity coupling model," *IEEE Access*, vol. 7, pp. 1–1, 2019.
- [80] N. Evano, R. El Abdi, and M. Poulain, "Lifetime modeling of silica optical fiber in static fatigue test," *J. Appl. Res. Technol.*, vol. 14, no. 4, pp. 278–285, 2016.
- [81] R. Grinberg, G. Riedel, A. Korn, P. Steimer, and E. Bjornstad, "On reliability of medium voltage multilevel converters," in *2013 IEEE Energy Convers. Congr. Expo. ECCE 2013*, 2013, pp. 4047–4052.
- [82] Sinclar-Knight-Merz(SKM), "Calculating target availability figures for HVDC interconnectors," Tech. Rep. December, 2012.

ISSN (online): 2446-1636  
ISBN (online): 978-87-7210-538-3

**AALBORG UNIVERSITY PRESS**